Retrieval of land surface emissivity from AMSR-E and SEVIRI data

Shi Qiu

UNIVERSITÉ DE STRASBOURG

N° d'ordre :

École Doctorale Mathématiques, Sciences de l'Information et de l'Ingénieur

UdS – INSA – ENGEES

THÈSE

présentée pour obtenir le grade de

Docteur de l'Université de Strasbourg
Discipline : Télédétection

par

Shi QIU

Retrieval of Land Surface Emissivity from AMSR-E and SEVIRI data

Soutenue publiquement le 20 Septembre 2013

Membres du jury

Directrice de thèse: M. Zhao-Liang Li, Directeur de recherches CNRS
Rapporteur externe: M. José A. Sobrino, Professeur de l'Université de Valence, Espagne
Rapporteur externe: M. Guangjian Yan, Professeur de l'Université Normale de Beijing, Chine
Examinateur: Mme. Françoise Nerry, Directeur de recherches CNR

Acknowledgment

First of all, I would like to express my sincere gratitude to my supervisor, Zhao-Liang Li, for his instructive advice and useful suggestions on my thesis. I am deeply grateful of his help in the completion of this thesis.

High tribute shall be paid to Dr. Caixia Gao and Dr. Zenglin Liu, whose unselfish help triggers my passion for this field and whose earnest attitude tells me how to do research in our major.

I am also deeply indebted to all the other tutors, teachers and all my colleagues in our laboratory, and they are Dr. Francoise Nerry, Raphael Luhahe, Dr. Jelila Labed, Prof. Marcel Raffy, Dr. Yoshitate Takakura, Dr. Jerome Colin, Dr. Roux Roman, Dr. Nicolas Albalat, Dr. Yonggang Qian, Dr. Ronglin Tang, Dr. Wei Zhao, Dr. Huazhong Ren, Sibo Duan, Rongyuan Liu, Jing Lu, Yuan Liu, Pei Leng, Xiwei Fan, Hongyuan Huo, and etc.

Special thanks to the reviewers, Dr. Francoise Nerry, Prof. José A. Sobrino and Prof. Guangjian Yan, for their hard work and valuable advice to perfect my thesis.

My sincere thanks are given to my parents and Uncle Li for their continuous support and encouragement.

It is difficult for me to quote everyone here. I simply make a point of saying that I appreciate everyone who helped me or gave me spirit supports.

This research was fully funded by the project CEOP-AEGIS (Coordinated Asia-European long-term Observing system of Qinghai-Tibet Plateau hydro-meteorological processes and the Asian-monsoon systEm with Ground satellite Image data and numerical Simulations).

Résumé

Restitutionde l'émissivité de surface terrestre à partir de données AMSR-E et SEVIRI/MSG2

Le climat de la Terre est déterminé principalement par la façon dont l'énergie est répartie entre les océans, la surface terrestre et l'atmosphère. Dans ces trois composantes principales, la surface de la Terre a un intérêt particulier en raison de sa relation directe avec les activités humaines.

La couverture terrestre de la Terre correspond environ à 30 % de la surface totale. Elle se compose de sols nus, de végétation, de neige, des glaciers, des eaux intérieures, des montagnes, des canopées urbaines, etc. Les processus en jeu à la surface de la Terre sont principalement dus aux échanges de chaleur, d'eau, de CO_2 entre la surface terrestre et l'atmosphère et constituent la partie principale des études sur le changement climatique. Ainsi, le changement climatique est du aux échanges d'eau et d'énergie entre la surface et l'atmosphère. L'eau, et plus concrètement l'humidité du sol, influencent fortement la répartition de l'énergie solaire incidente sur la surface de la Terre. On trouve le flux de chaleur latente, le flux de chaleur sensible et le flux de chaleur au sol. Le flux de chaleur latente (évapotranspiration), avec les précipitations, les changements d'humidité du sol et le ruissellement de surface, forment le bilan hydrique. La végétation affecte à la fois le bilan hydrique et énergétique et ce de plusieurs façons. En protégeant le sol du rayonnement solaire direct, la végétation limite l'énergie disponible par le flux de chaleur latente à partir des couches de surface. En même temps, la végétation extrait de l'eau de la Terre par ces racines pour sa propre alimentation et l'expulse ensuite dans l'atmosphère.

La couverture de la Terre est très variable sur une gamme d'échelles spatiales et temporelles. Cette grande hétérogénéité est un défi pour les études de validation des modèles globales météorologiques et climatiques. Les mesures in situ de ses caractéristiques ne sont en général pas représentatives d'une région plus large, ce qui rend nécessaire la mise au point d'un réseau dense de mesures reparties sur toute la surface terrestre. La création d'un tel réseau à l'échelle continentale n'est malheureusement pas réaliste. La seule solution pour acquérir des observations à l'échelle mondiale et sur le long terme de ces paramètres est la télédétection (Entekhabi et al. 1999).

L’émissivité de la surface de la Terre (LSE) est l'un des paramètres de surface les plus importants. Elle traduit la capacité de la surface à émettre un rayonnement. La LSE est d'une importance considérable pour de nombreuses applications telles que les études sur l’érosion des sols, les estimations des quantités et des changements de la couverture végétale, la cartographie du substratum rocheux et l'exploration des ressources (Gillespie et al. 1998). D’un autre côté, elle est aussi le paramètre clé pour déterminer l'humidité du sol et la température de la surface terrestre (LST) à partir d’études radiométriques (Kerr et al , 2001; Owe et al , 2001; Njoku et al, 2003; Verstraeten et al, 2006).

Considérant la progressive prise de conscience de l'importance de la LSE, l’intérêt pour l'estimation de celle-ci à partir de données de télédétection avec le développement de nouvelles techniques est aussi croissant, rendant possible la détermination et le suivi de la LSE à grande échelle. Dans le cas d’une estimation précise de la LSE à partir de données de télédétection, de nombreuses études ont été réalisées avec des méthodes différentes (Sobrino et al , 2001;Sobrino et al , 2005). Dans ces procédés, les méthodes de détermination de la LSE à partir des données infrarouge thermique (TIR) sont relativement matures et largement répandus. De la fin des années 1970, il y a eu de nombreuses études qui ont porté sur l’estimation de la LSE en utilisant la télédétection dans le domaine TIR. L’infrarouge thermique offre une des possibilités pour déterminer simultanément la LSE et la LST, à partir du rayonnement thermique émis par la surface de la Terre. Si les conditions atmosphériques sont favorables, il est possible de déterminer exactement LES et LST.

Comme les autres capteurs en télédétection optique, la télédétection TIR ne peut pas acquérir d’informations dans des conditions nuageuses. Par conséquent elle ne peut pas être utilisée pour produire les LSE et LST quand il y a de nuages. Une analyse de la NASA sur les produits LST, révèle que le résultat final a été affecté par les nuages pour plus de 60 % des régions étudiées, ce qui signifie que la télédétection dans l’infrarouge thermique comporte des limites importantes dans la pratique. D’un autre côté, des méthodes existent utilisant les données micro-ondes (MW) pour estimer la LST et sont très faiblement influencées par les effets atmosphériques comme les nuages, et donc peuvent compléter les résultats obtenus dans l’infrarouge thermique. La télédétection dans la bande des micro-ondes (MW) combinée avec le domaine TIR offre donc une capacité unique de détecter les paramètres de la surface terrestre dans presque toutes les conditions météorologiques

Bien que les données MW sont exploitées depuis de nombreuses années, des études ont mis l'accent sur les problèmes d'estimation de la LSE dans cette bande parce que: (1) il est difficile d'interpréter physiquement la LSE d'une surface hétérogène à faible résolution spatiale, (2) l'impact de l'humidité du sol et la rugosité de surface sur le LSE est très important, (3) comme dans le domaine TIR , la LST et le LSE sont difficiles à séparer, les deux grandeurs étant combinées dans le signal détecté, (4) bien que les données MW soient moins perturbées par l'atmosphère et les nuages que dans le domaine TIR, les effets atmosphériques doivent cependant encore être corrigés pour obtenir la LSE de façon précise, (5) les anciens capteurs MW ont un faible rapport signal/bruit, conduisant à une grande erreur sur la LSE.

Les travaux présentés dans ce mémoire de thèse visent à: (1) améliorer la méthode de d'obtention de la LSE à partir du capteur SEVIRI (SpinningEnhanced Visible and InfraRed Imager) à bord du satellite géostationnaire MSG (Météosat Seconde Génération), (2) à élaborer des méthodes d'extraction LSE à partir des données MW du capteur AMSR-E (Advanced Microwave Scanning Radiometer-EarthObserving System).

Les problèmes rencontrés sont de différents ordres :

Tout d'abord, la détermination de l'émissivité et la température de surface (LSE et LST) est un problème mathématiquement sans solution, même pour des mesures en surface. L'équation de transfert radiatif montre que le rayonnement émis à partir de la surface dans le domaine de l'infrarouge est une fonction de sa température et de l'émissivité. Si le rayonnement est mesuré à N longueurs d'onde, il y aura toujours N+1 inconnues, soit N émissivités correspondant à chaque longueur d'onde et une température de surface. La solution de ce système d'équations sous-déterminé décrits par les radiances mesurées est la principale difficulté dans la détermination simultanée de LST et LSE. Le couplage des deux grandeurs de surface (émissivité et température) dans la radiance mesurée, oblige un calcul précis de l'émissivité pour déterminer la température et vice-versa (Li et Becker, 1993; Becker et Li, 1995; Li et al, 2000).

Deuxièmement, l'absorption et l'émission propre de l'atmosphère, et la réflexion de la surface terrestre, compliquent davantage le problème de détermination de l'émissivité et la température de surface. L'échange d'énergie entre la surface terrestre et l'atmosphère est toujours combiné dans la bande spectrale, en particulier dans la bande spectrale TIR. D'une part, l'émissivité inférieure à l'unité (l'émissivité est égale à l'unité uniquement dans le cas

idéal d'un corps noir) entraîne une réduction de la radiance émise par la surface, d'autre part, l'atmosphère reflète une partie du rayonnement atmosphérique descendant propre de l'atmosphère en le renvoyant dans l'atmosphère.

L'anisotropie de la réflectivité et l'émissivité peut réduire ou accroître le rayonnement total de la surface (Prata, 1993). En outre, le rayonnement de surface mesuré par le satellite, est atténué par l'atmosphère avant d'atteindre le capteur. Considérant le rayonnement atmosphérique montant, l'atmosphère peut aussi avoir des effets indéterminés sur le rayonnement de surface initial. De toute évidence, l'effet combiné de l'émissivité inférieure à l'unité et des effets de l'atmosphère rend difficile l'obtention des LST et LSE à partir des mesures au niveau de l'atmosphère (TOA « Top Of Atmosphere ») (Dashet al, 2005). De ce point de vue, la LSE peut être considérée comme une variable cruciale qui doit être connue avant de corriger la radiance de surface des effets atmosphériques et de récupérer la LST. En outre, elle est le point clé pour résoudre le problème de couplage entre la surface de la terre et l'atmosphère. En plus, pour la région MW, les capteurs actuels ne sont pas encore très performants, et rendent les valeurs de température de brillances incertaines. En particulier dans la région de basse fréquence, il existe un grand écart de température de brillance due à l'interférence de radiofréquence. Néanmoins, la contribution atmosphérique est faible dans cette région de basse fréquence, et donc la plupart des modèles utilisent les données de basse fréquence, ce qui augmente la fiabilité des résultats. Ignorer la correction atmosphérique est généralement une autre raison pour réduire la précision en la détermination de l'émissivité à partir de données satellite et l'ajout d'une correction de ces effets peut résoudre ce problème.

Troisièmement, en raison de la complexité de la simulation de l'émissivité de la surface qui est affecté par la végétation, la topographie, les inondations, la neige et d'autres facteurs, les méthodes pour d'obtention la LST à partir des données passives MW doivent prendre en compte une variabilité spatiale et temporelle très importante, et par conséquent, l'étude de la surface de la Terre et l'inversion des paramètres atmosphériques en utilisant les données MW est encore très limitée.

Considérant les questions et les problèmes identifiés ci-dessus et à travers une étude complète des méthodes régionales d'estimation de l'émissivité à partir de données de télédétection existants, ce travail porte sur le développement d'une méthodologie permettant de déterminer l'émissivité à l'échelle régionale à partir des données TIR et des données passives MW à bord de satellites en orbite polaire.

Ce mémoire est composé de six chapitres.

Dans le premier chapitre, après l'introduction, l'état de l'art sur les méthodes d'estimation de la LSE régionale à partir de données satellites dans les deux régions spectrales d'étude (MW et TIR) est présenté. Trois différentes types de méthodes existent pour estimer la LSE à partir des données TIR : (1) les méthodes semi-empiriques, (2) les méthodes de séparation émissivité/température multicanal et (3) les méthodes basées sur des hypothèses physiques. Pour les études utilisant les données MW, les principales méthodes dédiées à l'estimation du LSE sont: (1) méthodes que utilisent des hypothèses physiques, (2) méthodes empiriques et (3) méthodes qui utilisent des réseaux neuronaux.

Dans le chapitre 2 les principes fondamentaux de la physique utilisés dans la détermination de la LSE à partir de données qui proviennent d'un satellite sont rappelés. Cela comprend les concepts de base des processus, la théorie de base de la télédétection pour la région des micro-ondes et pour l'infrarouge thermique (TIR), la diffusion de surface et les propriétés radiatives, l'absorption atmosphérique et les mécanismes de diffusion.

L'équation de transfert radiatif dans un cas général, s'écrit :

$$R(\theta_v,\lambda) = R_G(\theta_v,\lambda)t(\theta_v,\lambda) + R_{atm\uparrow}(\theta_v,\lambda) + R_{s\uparrow}(\theta_v,\lambda)$$

Cette équation peut être réécrite en termes de température de brillance comme:

$$B(T_{B,S},\theta_v,\lambda) = B\left(T_{B,G},\theta_v,\lambda\right)t\left(\theta_v,\lambda\right) + R_{atm\uparrow}\left(\theta_v,\lambda\right)$$

La contribution de la surface à la température de brillance totale est :

$$\begin{aligned} R_G(\theta_v,\lambda) &= B\left(T_{B,G},\theta_v,\lambda\right) \\ &= \varepsilon(\theta_v,\lambda)B(T_s,\lambda) + \left[1-\varepsilon(\theta_v,\lambda)\right]\left[R_{atm\downarrow}(\lambda) + R_{s\downarrow}(\lambda)\right] + \rho_b(\theta_v,\theta_s,\varphi,\lambda)E_{sun}(\theta_s,\lambda) \end{aligned}$$

Où $T_{B,S}$ est la température de brillance au niveau du satellite; θ_v est l'angle zénithale; $R_G(\theta_v,\lambda)$ est la radiance spectrale totale mesurée à niveau du sol; $T_{B,G}$ est la température de brillance à niveau du sol; $t(\theta_v,\lambda)$ est la transmission totale de l'atmosphère; $R_{atm\uparrow}(\theta_v,\lambda)$ et

$R_{s\uparrow}(\theta_v, \lambda)$ sont les radiances montantes spectrales directe et proviennent de la diffusion atmosphérique de la contribution solaire; $R_{atm\downarrow}(\lambda)$ et $R_{s\downarrow}(\lambda)$ sont les radiances atmosphériques descendante et la radiance atmosphérique descendant provenant de la diffusion atmosphérique de la contribution solaire ; $\rho_b(\theta_v, \theta_s, \varphi, \lambda)$ est la réflectivité spectrale bidirectionnelle; φ est l'angle d'azimutal relatif entre l'angle d'azimutal et l'azimutal solaire ; $E_{sun}(\theta_s, \lambda)$ est la radiance solaire directe au niveau du sol

Le chapitre 3 est consacré à décrire les capteurs, les données et les modèles utilisés dans ce travail.

Pour la restitution des émissivités dans la région des microondes (MW), les données du capteur AMSR-E et les données MODIS, tous les deux à bord du satellite américain Aqua, sur l'ensemble de la Chine, zone couvrant la longitude 71.875 ° E à 134,875 ° E et la latitude 4.125 ° N à 54.125 ° N, sont utilisés pour cartographier la LSE dans les différents canaux de MW en utilisant la méthode proposée dans cette thèse pour l'année 2006.

Pour restituer la LST à partir des données TIR, une zone géographique formée par la péninsule ibérique et d'une partie du Maghreb, a été utilisée, couvrant la longitude 15 ° W à 15 ° E et la latitude de 30 ° N à 45 ° N et.

Les données de satellite utilisées dans cette thèse sont les suivantes: celles du capteur AMSR-E (Advanced Microwave Scanning Radiometer-EarthObserving System) et celles du capteur MODIS (MODerate-resolution Imaging Spectroradiometer), ainsi que les données du capteur SEVIRI pour étudier la présence de nuages.

Pour réaliser les corrections atmosphériques nous avons utilisés les profils atmosphériques fournis par ECMWF (European Centre for Medium-Range WeatherForecasts) et les données d'élévation du terrain Digital Elevation Map (DEM).

Le modèle de transfert radiatif pour réaliser les simulations de LSE et LST est le code MODTRAN.

Le Chapitre 4 est centré sur l'estimation du LSE à partir de données micro-ondes passives. Notre premier objectif est de construire un modèle de transfert radiatif allant de la surface à l'atmosphère. Dans cette partie le modèle AIEM (Advanced Integral Equation Model) a été utilisé pour calculer l'émissivité de la surface de la Terre. Généralement, le modèle AIEM

fournit une connexion simple et précise entre l'émission de surface à des fréquences différentes et celles qui ont une polarisation différente, ainsi que les mesures des paramètres de rugosité de surface couramment utilisés. Pour éliminer les effets atmosphériques dans la région MW, le modèle MonoRTM (MONOchromatic Radiative Transfer Model) a été utilisé pour obtenir l'influence exacte de l'atmosphère. Finalement, le modèle SARTM (Soil-Atmosphere Radiative Transfer Model (SARTM)) a été construit à partir des modèles MonoRTM et AIEM.

Le deuxième objectif de ce chapitre est construire une base de données de LES à partir de données du capteur AMSR-E et de LST obtenues à partir de données MODIS. La section suivante est consacrée à (1) développer une relation empirique entre les émissions de surface dans la région MW avec polarisation verticale et horizontale (2) développer une méthode pour récupérer les LSE à partir des données AMSR -E, à condition que la LST soit connue ou puisse être estimée d'une autre façon.

En s'appuyant sur l'équation de transfert radiatif, une méthode a été proposée pour directement extraire l'émissivité de la surface à partir des données du capteur AMSR-E et MODIS, supposant l'atmosphère totalement caractérisée.

$$\varepsilon_{f,p} = \frac{T_{B,f,p} - T_{au,f} - T_{ad,f} \times t_f - T_{sp} \times t_f^{\,2}}{\left(T_s - T_{ad,f} - T_{sp} \times t_f\right) \times t_f}$$

où les indices *p* et *f* représentent l'état de polarisation (horizontale ou verticale) et la fréquence. T_{sp} est une constante que représente la température équivalente de l'espace, (T_{sp} = 2.7 *K*.). Dans cette étude, la LSE a été estimée à partir de la T_B (température de brillance à niveau du capteur), et de *f* et *p*, et la LST (T_s) estimée à partir des données MODIS et les profils atmosphériques fournis par ECMWF utilisés pour estimer les quantités atmosphériques (t_f, $T_{au,f}$, $T_{ad,f}$) avec le logiciel de transfert radiatif MonoRTM.

Un autre objectif de ce chapitre est d'analyser les effets atmosphériques sur des données AMSR-E et de proposer ensuite un algorithme de correction atmosphérique à 18,7 GHz en polarisation verticale, pour la restitution de LST. Dans cette section, une base de données provenant de simulations couvrant diverses conditions atmosphériques et surfaces a été d'abord construite. Les effets atmosphériques sur les observations AMSR-E sont ensuite

analysés et un algorithme de correction atmosphérique à 18,7 GHz avec une polarisation verticale est finalement proposé.

Utilisant la base de données simulée, qui couvre un large éventail de conditions de surface terrestres et atmosphériques, une analyse quantitative des effets atmosphériques sur les données AMSR-E a été faite. Les résultats montrent que l'atmosphère a un effet évident sur l'observation du capteur AMSR-E, à l'exception des bandes 6.925 et 10,65 GHz avec une polarisation verticale et 6.925 GHz avec une polarisation horizontale.

Une correction atmosphérique est nécessaire avant d'utiliser les données AMSR-E pour estimer les paramètres de la surface terrestre. En utilisant des relations empiriques et des hypothèses raisonnables, un algorithme de correction atmosphérique a été proposé. D'après les observations de deux canaux AMSR-E (18,7 et 23,8 GHz avec une polarisation verticale), les effets atmosphériques sur les observations à 18,7 GHz de polarisation verticale sont négligeables et peuvent être corrigés et la radiance émisse par la surface terrestre dans ce canal peut être estimée.

De même, la LST peut être estimée en utilisant la méthode proposée et une émissivité connue. Les résultats montrent que l'algorithme de correction est performant. Avec des données simulées, l'erreur quadratique moyenne diminue de 6,04 K à 0,99 K, et l'erreur quadratique moyenne de la LST est estimée à 1,17 K. Ces résultats indiquent que la méthode proposée est essentielle pour améliorer les estimations des paramètres de la surface terrestre.

Le chapitre 5 présente un algorithme amélioré pour obtenir simultanément LSE et LST à partir des données du capteur SEVIRI à bord du satellite MSG-2. La méthode des TISI (Temperature Independent Spectral Indices) a été révisée et sera utilisé pour déterminer l'émissivité. Du fait des faibles résolutions temporelles et spatiales des descriptions des profils atmosphériques disponibles, un logiciel pour adapter les corrections atmosphériques a été développé et amélioré avec le but d'estimer LSE à partir du concept des TISI. Enfin, cet algorithme amélioré est appliqué à plusieurs données SEVIRI sur la zone d'étude. Avec plusieurs cas détaillés, il est démontré que ces améliorations sur la méthode de détermination de la LSE sont efficaces et raisonnables. Ce chapitre est organisé comme suit. La section 5.2 décrit toutes les données utilisées dans cette étude. Les principes des méthodes d'extraction de LSE et LST et de leurs applications aux données SEVIRI sont détaillés à la section 5.3. La section 5.4 présente les résultats préliminaires obtenus à partir des données MSG-2/SEVIRI et

les résultats de leur validation croisée avec les produits dérivés de LST MODIS. La section 5.5 est consacrée aux conclusions.

Parce que les LST et LSE sont les principales caractéristiques de la surface de la Terre dans le domaine thermique, leurs restitutions à partir de l'espace a été étudié depuis plusieurs décennies. Sur la base des études de Jiang *et al.* (2006) et Jiang (2007), un algorithme opérationnel amélioré est développé dans ce document pour déterminer à la fois le LSE et LST à partir des mesures MSG-2/SEVIRI. Trois modules de l'algorithme TISI jour/nuit sont améliorés : les corrections atmosphériques, la mise en place du modèle de réflectivité bi-directionnelle et la récupération de la LSE dans le canal SEVIRI 10. La méthode GSW proposé par Becker et Li (1990) et amélioré par Wan et Dozier (1996) est ensuite utilisée pour obtenir la LST.

L'application de notre algorithme aux données SEVIRI sous différentes conditions climatiques et atmosphériques a révélé que le nouvel algorithme de correction atmosphérique résout des problèmes qui existaient dans l'algorithme original proposé par Jiang *et al.* (2006) et Jiang (2007). En effet dans le cas particulier des corrections atmosphériques dans les régions avec une heure de levé du soleil tardive, les résultats obtenus par le nouvel algorithme sont plus réalistes, ce qui montre que l'algorithme amélioré est plus efficace.

Pour valider résultats de LST (SEVIRI LST1) issus des mesures SEVIRI obtenus en utilisant l'algorithme amélioré, des validations croisées sont menées sur deux jours clairs (22 Août 2009 et 3 Juillet 2008) sur toute la zone d'étude avec les LST MODIS.

Le résultat montre que dans plus de 70 % des cas, la différence entre le SEVIRI LST1 et MODIS LST est inférieur à 2,5 K. Les différences de LST ont tendance à être plus basses la nuit que pendant la jour en raison des conditions thermiques relativement homogènes de la surface de la Terre pendant la nuit. Toutefois, d'autres travaux de validation doivent être effectués en utilisant des mesures de terrain.

Les conclusions de ce travail et les perspectives sont données dans le sixième chapitre.

Contents:

List of Figures:

List of Tables:

Chapter 1

Introduction

The Earth's natural climate is mainly determined by the way energy is distributed between the ocean, the land surface, and the atmosphere. In these three main components, the land surface is of particular interest because of its direct and local impact on human activities.

Land surface covers about 30% of the Earth's surface, it consists of soil, vegetation, snow, glaciers, inland water, mountains, and much more. Land surface process, in principal, refers to the exchanges of heat, water, CO_2, and other trace constituents at the interface of land surface and atmospere, it is the center of climate change studies. The climate change is the coupled water and energy balance within the land-atmosphere continuum. Water, particularly surface soil moisture, strongly influences the partitioning of the incoming solar energy at land surface into latent, sensible and ground heat fluxes. Latent heat flux, together with precipitation, soil moisture change, surface and subsuface runoff makes up the water balance. Vegetation affects both water and energy balances in several ways. By shielding the soil from direct solar radiation, vegetation limits the energy available for the latent heat flux from the surface layers. At the same time, the vegetation extracts water from the whole root zone and transpires it into the atmosphere (Chahine, 1992; Njoku et al., 2003; Weng et al., 2004).

The land surface is also most variable over a broad range of temporal and spatial scales. This large heterogeneity is a challenge for validation studies of global meteorological and climate models. In situ measurements of its characterizations are generally not representative for a wider region, making dense long-term measurement networks necessary. Creating such a network on a continental scale is, unfortunately, not feasible. The only realistic way to acquire long-term global observations of the key surface parameters is by means of remote sensing (e.g. Entekhabi et al., 1999). Land surface emissivity (LSE) is one of the most important surface parameters, it is the relative ability of the radiation emitted by the land surface. LSE is of considerable importance for many applications such as soil development and erosion studies, estimating amounts and changes in spare vegetation cover, bedrock mapping and resource exploration (Gillespie et al., 1998). In addition, it is the key parameter to retrieve soil moisture and Land Surface Temperature (LST) from radiometry (e.g. Kerr et al., 2001; Owe et al., 2001; Njoku et al., 2003; Verstraeten et al., 2006).

As the gradual awareness of the importance of the LSE, there is an increasing interest in LSE estimate from remotely sensed data with the development of remote sensing technology, that makes retrieving and monitoring LSE in a large scale be possible. In the case of accurate estimation of LSE from remotely sensed data, many studies have been performed with

different methods. Methods for LSE retrieval from Thermal InfraRed (TIR) data are relatively mature and widespread. From late 1970s, there have been many studies focused on LSE estimate using TIR remote sensing. TIR remote sensing provides one of the possibilities to retrieve LSE and LST from land surface emitted thermal radiation without damaging it. As the other optical remote sensors, remote sensing in TIR cannot capture the surface information under cloudy conditions; consequently it cannot be used to produce LSE in these conditions.

In comparison with TIR, Microwave (MW) remote sensing provides a unique capability for sensing land surface parameters under nearly all weather conditions because it can penetrate cloud to capture land surface parameters. Although MW data have been exploited for many years, a few studies have been directly focused on LSE estimation because: (1) it is difficult to physically interpret LSE for heterogeneous surface at low spatial resolution; (2) impact of soil moisture and surface roughness on LSE is very important; (3) like TIR, LST and LSE are difficult to be separated from passive MW data; (4) Although MW data are less perturbed by the atmosphere and the cloud, atmospheric effects still need to be corrected to get more accurate LSE; (5) former MW sensors had low signal to noise ratio, leading to large error on LSE.

This study aims: (1) to improve LSE retrieval method from the Spinning Enhanced Visible and Infrared Imager (SEVIRI) data on board the geostationary satellite (Meteosat Second Generation (MSG)); (2) to develop LSE retrieval method from MW data (Advanced Microwave Scanning Radiometer-Earth Observing System (AMSR-E)).

1.1 Overview of LSE retrieval methods from TIR data in the past decades

LSE, as an intrinsic property of natural materials, is often regarded as an indicator of material composition, especially for the silicate minerals, although it varies with viewing angle and surface roughness (Sobrino et al., 2001; Sobrino et al., 2005). Being so important, the methodology which produces LSE from remotely sensed data has been developed for many decades.

Remote sensing can provide LSE at different temporal and spatial scales. Estimation of LSE from TIR data caught people's attention since the TIROS satellite launched in 1962. From 1970s, a large number of studies have been conducted to retrieve LSE. With the development of space information technology in the past 40 years, although satellite-derived

LSE from TIR data has made a great progress, there are still at least two problems to be cleverly resolved (Becker and Li, 1995): (1) a separation of LSE and LST from radiance at ground level and (2) atmospheric corrections.

Radiance measured from space can cover large spectral range, from the visible/near-infrared (VNIR), Middle InfraRed (MIR), TIR to MW. This radiance contains the combined effects of surface and atmosphere. To date, various methods have been proposed to retrieve LSE. Several methods use statistical relationships between the measurement and LSE; others use reasonable assumptions or constraints on Planck's function and the atmospheric radiance transfer equation (RTE) to solve the undetermined problem or the ill-posed inversion problem. Generally, there are three distinctive ways to estimate LSE from TIR data: (1) semi-empirical methods, (2) multi-channel temperature/emissivity separation methods and (3) physically based methods.

1.1.1 Semi-empirical methods

This type of methods estimates the LSE from the semi-empirical classification-based look-up table or the statistical relationship between the normalised difference vegetation indexes (NDVI) derived from the VNIR bands and LSE in the TIR bands. The representative methods are the classification-based emissivity method (Snyder et al., 1998a; Sun and Pinker, 2003; Peres and DaCamara, 2005) and the NDVI-based emissivity method (Van de Griend and Owe, 1993; Valor and Caselles, 1996; Sobrino and Raissouni, 2000).

(1) Classification-based emissivity method (CBEM). Generally, the CBEM is based on the use of conventional land-cover classification information. The key point of this method is to properly classify the land surface and then to assign the emissivity from classification-based look-up tables. Theoretically, the CBEM can produce accurate LSE products over the area in which land covers are accurately classified and each class has well-known emissivities (Gillespie et al., 1996). However, Snyder et al. (1998a) pointed out several major difficulties in using CBEM, such as the determination of surface wetness, the identification of senescent vegetation and the uncertainty of the dynamics of snow and ice surface states. The superiority of CBEM are: 1) simplicity; 2) accuracy for the pixels with classes having well known emissivities; 3) accurate atmospheric correction is not required; 4) emissivity can be obtained at the same spatial resolution as that of visible and near infrared data; 5) no requirement of the TIR bands. In another hand, the

limitations and disadvantages are: 1) require the *a prior* knowledge of emissivity database for classes, as well as the corresponding classification map; 2) depend on classification accuracy; 3) seasonal and dynamic states, such as the surface wetness, senescent vegetation and the uncertainty of dynamics of snow and ice, may degrade the accuracy; 4) less accurate for coarse resolution and less reliable for the classes with contrast emissivities, e.g., geologic substrates; 5) displays discontinuities.

(2) NDVI based emissivity method (NBEM). Within the framework of the project 'Botswana Water and Surface Energy Balance Research Program', Van de Griend and Owe (1993) found a very high correlation between the LSE in the band covering from 8-14 μm and the logarithmic NDVI, i.e.,

$$\varepsilon = a + b\ln(NDVI), \tag{1.1}$$

where a and b are constants derived from regression analysis. Although this method is a potentially powerful tool to estimate the LSE at a pixel scale directly from space because NDVI can be easily derived from the reflectance in VNIR bands, the relationship has been proven to be quite dependent on the area studied, and the coefficients a and b obtained for one site cannot be applied to other sites (Van de Griend and Owe, 1993). Inspired from the work of Van de Griend and Owe (1993), using the NDVI as a connection to describe the 'cavity effect', Valor and Caselles (1996) proposed a method derived from the model of Caselles and Sobrino (1989), to estimate the effective LSE for a row-distributed rough system.

Considering the complexity of method proposed by Valor and Caselles (1996), Sobrino and Raissouni (2000) further developed an operational NDVI threshold method to derive the LSE from space using the following criteria and formulae:

$$\varepsilon_i = \begin{cases} a_i + b_i\rho_{red} & NDVI < NDVI_s \\ \varepsilon_{v,i}P_v + \varepsilon_{s,i}(1-P_v) + d\varepsilon_i & NDVI_s < NDVI < NDVI_v \\ \varepsilon_{v,i} + d\varepsilon_i & NDVI > NDVI_v \end{cases}, \tag{1.2}$$

where a_i and b_i are channel-dependent regression coefficients, ρ_{red} is the reflectivity of the red channel and $NDVI_s$ is the NDVI corresponding to the bare soil. $\varepsilon_{v,i}$ and $\varepsilon_{s,i}$ are the vegetation and soil emissivities in channel i, respectively. Both of them can be measured in the field (Rubio et al. 1997, Rubio et al. 2003) or obtained from an emissivity database

(Baldridge et al. 2009). P_v is the fraction of vegetation that can be derived either from the NDVI (Valor and Caselles 1996, Carlson and Ripley 1997, Sobrino and Raissouni 2000) or from the variable atmospherically resistant index (VARIgreen) and spectral-mixture analysis techniques (Sobrino et al., 2008), $d_{\varepsilon,i}$ is the mean cavity effect and can take values of 0.02 or higher from numerical simulation (Valor and Caselles 1996) and $NDVI_v$ is the full vegetation *NDVI*. $NDVI_s$ and $NDVI_v$ can be estimated from the histogram for the entire scene (Dash et al., 2005; Sobrino et al., 2008).

Because of its simplicity, the *NDVI* threshold method has already been successfully applied to various sensors. However, the main problem with this method is the lack of continuity for emissivity values at $NDVI = NDVI_s$ and $NDVI = NDVI_v$ because they are calculated using different functions (Sobrino et al., 2008). In addition, the NDVI threshold method can only provide acceptable results in the 10–12 μm interval bands because the relationship between the emissivity and reflectivity for bare soil samples does not provide satisfactory results in the 8–9.5 μm domain for some soil types.

1.1.2 Multi-channel temperature/emissivity separation methods

The multi-channel temperature emissivity separation methods referred to a group of algorithms that retrieve the LSTs and LSEs from the at-surface radiances. After introducing some reasonable assumptions or constraints, these methods retrieve the LSEs directly from the emitted radiance.

(1) Emissivity spectrum feature-based methods. This type of methods determines the emissivity from the characteristics of emissivity spectra. The emissivity can be derived using several methods: by assuming that the emissivity at a channel is time-invariable, e.g., the two-temperature method which can directly estimate the spectral emissivity without any assumption about the spectral shape, but it is sensitive to the noise (Watson, 1992); by assuming that emissivity has a flat spectrum at specific wavelengths, e.g., the gray-body emissivity method which is thought to be more applicable for hyperspectral TIR data (Barducci and Pippi, 1996); by assuming that the emissivity spectrum is smooth, e.g., the iterative spectrally smooth temperature emissivity separation method, which is proposed to estimate LST and LSE from hyperspectral data (Borel, 1997 and 1998); or by applying *a priori* knowledge about the emissivity distribution range, e.g., the emissivity bounds method (Jaggiet al. 1992).

(2) **Reference channel method (RCM).** The RCM was first developed by Kahle et al. (1980). Supposing the LSE of channel *i* have been known, the LST can be derived for each pixel from the measured radiance in reference channel with known emissivity after atmospheric correction. This LST is then used to derive emissivity values for the remaining channels. The RCM is the simplest method for the emissivity retrieval from space, and it suffers from some limitations. First, it is difficult to find a unique emissivity value that is appropriate for all surface materials in one reference channel. (Gillespie et al., 1996; Li et al., 1999b). Second, there is no emissivity spatial information in reference channel. Third, the emissivities derived for adjacent channels are significantly affected by the constant value of emissivity in this channel and appear to be very noisy (Hook et al., 1992). The superiority of the method RCM is simplicity, and the simultaneous retrieval of surface temperature and emissivity for the remaining channels. The limitations and disadvantages are: 1) require accurate atmospheric corrections in TIR channels; 2) inappropriate to assign a unique value for all the surface materials in a specific channel; 3) accuracy of emissivity and temperature depends largely on the assigned constant value.

(3) **Normalisation emissivity method (NEM).** This method, which is an improvement of RCM as the channel with the maximum emissivity can be different in the NEM for different materials, was first described by Gillespie (1985) and used by Realmuto (1990). This method assumes a constant emissivity in all *N* channels for a given pixel, which enables *N* temperatures to be calculated for each pixel from their measured radiance provided that the atmospheric quantities involved in the RTE are known. The maximum of those *N* temperatures is considered to be the LST and used to derive LSEs for the other channels as is done with RCM. The superiority of this method are: 1) simplicity; 2) channel with the maximum emissivity is not specified, and may be different between pixels; 3) having better performance than RCM. In another hand, require accurate atmospheric corrections in TIR channels, and the accuracy of emissivity and temperature depends largely on the assigned maximum emissivity value are the method's limitations and disadvantages.

(4) **Temperature emissivity separation (TES) method.** TES is an algorithm initially developed for retrieving LST and LSE from ASTER images (Gillespie et al., 1998; Abrams 2000). This algorithm hybridizes three mature modules: NEM, spectral ratio (SR) and min-max difference (MMD). TES first uses the NEM module to estimate the initial surface temperature and the normalised emissivities from the atmospherically corrected

radiances at ground level; the SR module is subsequently used to calculate the ratio of the normalised emissivities to their average; finally, on the basis of the spectral ratio, the MMD module is used to find the spectral contrast in *N* channels and establishes an empirical relationship between the minimum emissivity in *N* channels and MMD. This method is operationally applied to the ASTER TIR data for recovery of LST and LSEs. Numerical simulations demonstrate that the TES algorithm can recover temperature within about ±1.5K, and emissivities within about ±0.015 for ASTER data if the atmospheric effects are accurately corrected (Abrams, 2000). The superiority of this method is: 1) refines the values of the maximum emissivity used in the NEM; 2) does not need any assumptions on emissivity; 3) retrieve simultaneously LST and LSEs for any kinds of surfaces. The limitations and disadvantages are: 1) require accurate atmospheric corrections in TIR channels; 2) require at least three TIR bands in atmospheric windows; 3) accuracy depends on atmospheric compensation and the empirical relationship between the minimum emissivity and MMD; 4) uncertainty is more serious for gray bodies, for example agricultural areas.

1.1.3 Physically based methods (PBM)

The methods reviewed above generally assume that the atmospheric effects on the radiances measured at the TOA have been accurately corrected for or that the radiances are measured at ground level. As far as the estimation of LST and LSEs from space measurements is concerned, in addition to the unknown LST and LSEs, there are some additional unknowns from the spectral absorption and emission in the intervening atmosphere. With *N* spectral measurements from space, the solution for temperature and *N* spectral LSEs is underdetermined. There are three of the early physically based methods that have been fairly widely used to approach this problem using various physically based assumptions or constraints. These methods include the Day/night temperature-independent spectral-indices (TISI) based method (Becker and Li, 1990a; Li and Becker, 1993; Li et al., 2000), the physics-based day/night operational method (Wan and Li, 1997), and the two-step physical retrieval method, which uses the principal component analysis (PCA) technique to decrease the number of unknowns (Ma et al., 2000 and 2002; Li et al., 2007).

(1) Day/night TISI-based method. Becker and Li (1990a), and Li and Becker (1990) first proposed a TISI-based method to perform spectral analysis in the TIR region.

Subsequently, assuming that the $TISI_{ij}$ (*i* is the MIR channel and *j* is the TIR channel) in the daytime without the contribution of solar illumination is the same as the $TISI_{ij}$ in the night-time, Li and Becker (1993) and Li et al. (2000) further developed a day/night TISI-based method to first extract the bidirectional reflectivity in MIR channel *i* by eliminating the emitted radiance during the day in this channel by comparing the $TISI_{ij}$ in the daytime and the night time. Once the bidirectional reflectivity in an MIR channel is retrieved, the directional emissivity in that MIR channel can be estimated to be complementary to the hemispheric-directional reflectivity, which can be estimated from a bidirectional reflectivity data series using either an angular form factor (Li et al., 2000), a semi-empirical phenomenological model (Petitcolin et al., 2002) or a kernel-driven bidirectional reflectivity model (Jacob et al., 2004; Jiang and Li, 2008a; Lucht and Roujean, 2000; Roujean et al., 1992; Wanner et al., 1995). Finally, based on the concept of the TISI, the LSEs in the TIR channel j can be obtained from the two-channel TISI and the emissivity in the MIR channel (Jiang et al., 2006; Li et al., 2000).

Because of its physical basis, the day/night TISI based method does not require any a priori information about the surface and can be applied to any surface, even those with strong spectral dynamics. Generally, the time-invariant TISI assumption appears to be reasonable in most situations. The TISI, which is a ratio on emissivities, will remain unchanged over several days unless rain and/or snow occur. It is worth nothing that night time dew formation may affect the assumption, especially for low-emissivity surfaces in dry areas (Snyder et al., 1998). Although the frequency of dew occurrence is not so high in most semi-arid and arid regions, it is worth to try checking the relative humidity value in the low boundary layer to avoid heavy dew events becoming a serious problem (Wan, 1999). Therefore, this method is superior to the (semi-) empirical stepwise retrieval methods above, especially on bare and geologic substrates that exhibit contrast emissivities.

However, several requirements may limit the usage of this algorithm in LSE retrieval from space. First of all, approximate atmospheric corrections and concurrence of both MIR and TIR data are required (Sobrino and Raissouni, 2000). Then, accurate image co-registration must be performed (Dash et al., 2005). Additionally, the surfaces must be observed under similar observation conditions, e.g., viewing angle, during both day and night (Dash et al., 2005).

(2) Physics-based day/night operational (D/N) method. The physical method usually faces more unknowns simultaneously; in other words, the physical method needs more channels than other methods. To simultaneously retrieve LSEs and LST without an accurate *a priori* knowledge of emissivity information and atmospheric parameters, Wan and Li (1997) proposed a physics-based retrieval method using day/night pairs of combined MIR and TIR data. The main purpose of this method is to retrieve LST and LSEs in semiarid and arid regions where the surface emissivity varies spatially over a wide range (Wan, 1999). The method is based on three assumptions of surface optical properties. First, the surface emissivity does not significantly change in the day/night times in several days unless rain and/or snow occur during the short period of time. Second, the angular form factor f_i has very small variation (<2%) in the wavelength range of interest in MIR. And third, the Lambertian approximation of surface reflection for downwelling diffuse solar irradiance and atmospheric thermal irradiance does not introduce significant error in the 3-14 μm regions. The radiance measured can be expressed as

$$L_i = \tau_{1i}\varepsilon_i B_i(T_S) + R_{ati\uparrow} + R_{sli\uparrow} + \frac{1-\varepsilon_i}{\pi}[\tau_{2i} f \mu_0 E_i + \tau_{3i} R_{sli\downarrow} + \tau_{4i} R_{ati\downarrow}], \qquad (1.3)$$

where $R_{ati\uparrow}$ and $R_{sli\uparrow}$ are the thermal path radiance resulting from the atmosphere and scattering of solar radiation, respectively, μ_0 is cosine of the solar zenith angle, and τ_{ji}, $j = 1,...,4$ are band effective-transmission functions for the corresponding terms. To reduce the uncertainties in the initial atmospheric conditions, two variables are used to modify the initial atmospheric profiles. One is the air temperature at the surface level (T_a) and the other is the total atmospheric column water vapour (CWV). With two measurements (day and night) in N bands, the numbers of unknowns are N+7 (N band ε, 2 T_s, 2 T_a, 2 CWV and 1 f). To make the equations deterministic, the number of observations (2N) must be equal to or greater than the number of unknowns (N+7), which makes $N \geqslant 7$. Because 2N equations are nonlinear, a statistical regression method is used to give the initial values of N+7 unknowns. Next, a numerical algorithm, such as the least-squares-fit (χ^2) method, is used to find an accurate solution for N+7 unknowns from 2N measurements (2N equations) (Wan and Li, 1997). In the day/night algorithm, a look-up table of atmospheric parameters is also employed for high efficiency. More details on the MODIS *D/N* method can be found in Wan and Li (1997), Wan (2008) and Wan and Li (2010).

The superiority of this method is: 1) does not require *a priori* accurate atmospheric profiles; 2) solution is more stable and accurate by introducing MIR channels; 3) accuracy of LSTs and LSEs is largely improved by modifying the atmospheric profiles in the retrieval; 4) retrieve accurately both LSTs and LSEs on the physical basis. The limitations and disadvantages are: 1) require multi-temporal data in several channels in the MIR and TIR atmospheric windows; 2) require accurate geometric registration; 3) approximate shapes of the atmospheric profiles need to be given a priori; 4) retrieval process is complicated and initial guess values are required.

(3) Two-step physical retrieval method (TSRM). Although MODIS is not specifically designed as a sounding instrument, it has 16 bands in the MIR and TIR regions, several of which match the corresponding bands on the high-resolution infrared radiation sounder (HIRS). MODIS can be therefore used to extract atmospheric profiles (Menzelet al., 2006). However, due to the coupling between the atmospheric information and surface temperature by both the surface emissivity and atmospheric transmittance, the retrieval process is a difficult task. Ma et al. (2000) made a first attempt to simultaneously retrieve LST, atmospheric temperature-humidity profiles by assuming that emissivities are constant in MIR and TIR regions respectively and the solar contribution in MIR is ignored. Nevertheless, these assumptions may degrade the accuracy of atmospheric parameter retrievals in the troposphere (Ma et al., 2000). Li et al. (1999c) demonstrated that surface emissivity spectra of more than 50 soil and vegetation samples measured in the laboratory could be reconstructed with an uncertainty of 0.005 by six selected bands in the 8-13 μm. Due to the fact that emissivity spectra can be recovered by a few number of unknowns in the interest spectral region, Ma et al. (2002) proposed an extended two-step physical retrieval method to extract LSEs, LST and atmospheric temperature-humidity profiles with MODIS MIR and TIR data by taking the solar contribution into account.

The main idea of this method inherits that of atmospheric profiles retrieval. First, the atmospheric RTE is tangent-linearized with respect to the atmospheric temperature-humidity profiles, LST and LSEs. Giving an initial guess of LSEs, LST and atmospheric temperature-humidity profiles, a set of equations based on the tangent-linearized RTE can be derived with the MODIS measurements. However, this is still a nondeterministic problem because the number of unknowns is still larger than the number of equations. Consequently, the PCA technique is applied to the atmospheric

temperature-humidity profiles as well as to the surface emissivity spectra so that the number of retrieved parameters is reduced and the solution of the set of equations becomes deterministic. On this basis, Ma et al. (2000, 2002) proposed a two-step physical retrieval method to extract emissivity, together with LST, atmospheric temperature and moisture profiles by using one after the other the Tikhonov regularisation and Newton iterative algorithms. The Tikhonov regularisation is used to stabilize the ill-posed problem and to obtain a meaningful solution, while the Newton iterative algorithm is used to further improve the solution. Thus, the name of the technique is "two steps".

There are some assumptions involved in the linearization of the RTE. These assumptions include a horizontally homogeneous atmospheric condition, a specular surface reflection to simplify the integral of the downwelling atmospheric radiation, and a constant anisotropic factor (angular form factor) in MIR region to describe the non-Lambertian distribution of the bidirectional reflectance. However, these plausible assumptions may introduce some errors in the retrieval, but play only a secondary role. As discussed by Ma et al. (2002), one possible improvement of this type of method is to improve the first-guess of the profiles and LSEs. They suggested using a model-based first guess of the MODIS retrieval, the Atmospheric Infrared Sounder (AIRS) retrievals, and the first-guess of LSE retrieved by *D/N* method. In addition, this method can be used to process the hyperspectral TIR data, such as AIRS and Interferometer Atmospheric Sounding Instrument (IASI). These sensors have thousands of channels in 3-14 μm. Although the physical method gives definitely physical meaning for each parameter, it is of great complexity. Similar to the above procedure, Li et al. (2007) retrieved global TIR emissivity spectra from AIRS data using the physical method. However, more work, such as the quality assurance, need to be done before taking this approach for operational process.

Generally, the superiority of this method are: 1) do not need *a priori* atmospheric corrections; 2) retrieve simultaneously the atmospheric profiles, LST and LSEs; 3) PCA and Tikhonov regularisation can be used to make the solution more stable and accurate. The limitations and disadvantages are: 1) complexity; 2) low computational efficiency limits the application; 3) require adequate numbers of channels; 4) require an initial guess of LSEs, LST and atmospheric temperature-humidity; 5) the solution is more dependent on the initial guess.

1.2 Overview of LSE retrieval methods from passive MW data in the past decades

As TIR remote sensing has its own limitations, the importance of the passive MW remote sensing has been gradually shown in recent years. The first Earth observing satellite was the Russian COSMOS-243 with one of microwave radiometers at 37 GHz onboard. Through the years, remote sensing became more sophisticated and in 1978 the American NIMBUS-7 satellite carried the Scanning Multichannel Microwave Radiometer (SMMR), providing global coverage at several microwave bands. In the next three decades many increasingly advanced missions followed (Holmes, 2008).

The most important reason for using MW is its capability to penetrate clouds and to some extent rain to view land surface. Passive MW can be therefore used in nearly all-weather conditions with multi-polarization modes. The second reason for the use of MW sensors is that they are able to penetrate more deeply into vegetation than optical light can. The third reason is that MW and TIR complement to each other under some circumstances. Generally, the microwave remote sensing has some unique advantage on monitoring land surface parameters, particularly soil moisture, LSE and LST monitoring. In recent years, with the widespread use of the passive MW data, there are three main methods dedicated to LSE retrieval. The first is a stepwise retrieval method that determines the LSE and the LST separately. The LST is estimated first, and then the LSE is retrieved. The second is a simultaneous retrieval method that treats both the LST and the LSE as unknowns and resolves both of them from the atmospherically corrected radiances. The third is the artificial neural network (ANN) method which simultaneously retrieves the LST and the LSE without exact knowledge of the complex physics mechanisms.

1.2.1 Stepwise retrieval methods

This type of method retrieves the LSE using two consecutive steps. First, the LST is (semi-)empirically determined from MV measurements at different frequencies and polarizations or physically estimated from TIR measurements. Then, the LSE is estimated by the inversion of the radiative transfer equation in MV, provided that the atmospheric effects could be removed or corrected (Jones and von der Haar 1990; McFarland et al.1990; Prigent 1997; Jones et al. 2011; Moncet et al., 2011).

1.2.2 Simultaneous LSE and LSTretrieval methods with known atmospheric information

Because the accuracy of the retrieved LSE is primarily dependent on the accuracy of the LST, simultaneous determination of the LSE and the LST has been proposed to improve the retrieval accuracy. Many simultaneous LST and LSE retrieval methods with given known atmospheric information have been developed since the 1990s. These methods can be roughly grouped into two categories: the multi-temporal and multi-spectral retrieval methods. The multi-temporal retrieval methods primarily make use of measurements at different times to retrieve the LSE and the LST under the assumption that the LSE is time-invariant. The representatives of these methods is the two-temperature method (Xiang and Smith, 1997), aiming to reduce the number of unknowns in the retrievals. The multi-spectral retrieval methods rely on the intrinsic spectral behaviour of the LSE at different polarizations or different frequencies rather than temporal information. The representatives of the multi-spectral methods is the linear emissivity constraint method (Fily et al. 2003), which uses the empirical linear relationship between LSEs at different polarizations to increase the number of equations.

1.2.3 Artificial neural network (ANN)method

Over the past decade there have been considerable increases in both the quantity of remotely sensed data available and the use of neural networks. These increases have largely taken place in parallel. An increasing awareness of the significance of neural network technique has been made by some researchers, because the radiative transfer and the interaction of physical processes in the microwave inversion of surface parameters is non-linear.They tried to retrieve surface parameters by neural network for getting higher accuracy product. As the solution and stability is unknown, the resolution is always ill. Using the priori initial value is very important for eliminate these uncertainties. Aires et al. (2001) proposed a neural network approach for retrieving atmospheric water vapor, cloud liquid water path, surface temperature, and emissivites over land between 19 and 85 GHz from SSM/I observations. They showed that the neural network with first guess and variational assimilation approaches shares important theoretical concepts and highlight some of the technical differences. The LSEs were retrieved with an accuracy of better than 0.008 in clear conditions and 0.010 in cloudy conditions.

1.3 Problems/issues

The LSE has already been recognised as a crucial parameter for the discrimination and sometimes the identification of various surface types and for the determination of LST by radiometry. Although various methods have already been developed, there is still no best method to retrieve LSE from space. All of the methods either rely on statistics relationships or on assumptions and constraints to solve the inherent ill-posed retrieval problem. Therefore, they might not hold true under some circumstances, and it is necessary to choose the optimum approach to estimate LSEs from space for a particular case by taking the sensor characteristics, the required accuracy, computation time, as well as the availability of atmospheric temperature and water vapour profiles into accounts. From the previous discussion, the main restricting factors in the estimates of LSEs from remotely sensed data are actually the following:

(1) The difficulty of the atmospheric corrections: The presence of the atmosphere between the land surface and the sensors at satellite level disturbs the radiances measured by a radiometer at the TOA. These radiances result primarily from the emission/reflection of the surface modulated by the effects of the absorption, diffusion and emission of the atmosphere. To minimise these atmospheric effects, spectral channels are always built in the windows where the atmosphere is most transparent. The atmospheric corrections thus consist of correcting the radiance measured by the sensors for the effects of atmospheric absorption, emission and emission-reflection. These effects can be variable because of the great variability of the vertical profiles of atmospheric water vapour and temperature.

(2) The difficulty in decoupling the LST and LSEs in the measured radiances. Independent of the atmospheric problems presented in all spectral regions, the spectral radiance emitted by a surface is a product of the spectral LSEs of this surface and the spectral radiance of the black body at the LST. Therefore, it is not possible in passive radiometry to separate, on a physical basis, the contributions due to LSE from the contributions due to LST in the observed radiance. For this reason, the LSE determination from space requires not only atmospheric corrections but also knowledge of the LST and vice versa.

(3) The difficulty of physical interpretation of the measurement. The difficulties raised by the atmospheric corrections and the temperature-emissivity coupling are, to some extent, of a technical nature. On the other hand, the scaling problem is much more fundamental because it implies a conceptual analysis of the physical significance of the measured

quantities (variables). Indeed, the diversity of continental surfaces involves spatial (vertical and horizontal) and radiometric heterogeneities of surface. Considering that the spatial resolution of the current on board systems varying from 10^{-2} to 2500 km2, it is therefore necessary to be able to define and correctly interpret surface parameters (variables) independently of the scale used and the processes necessary to validate this definition.

(4) The difficulty of validation of the LSEs retrieved from space at satellite pixel scale: Comparisons between LSEs derived from space and in-situ measurements are required to evaluate the reliability and accuracy of the LSE retrieved methods. Although it may be feasible and reasonable to validate LSEs derived from remotely sensed data with traditional measurements, mainly conducted at the "point" scale over uniform areas, problems will be encountered when the validation is performed over complicated land-surface areas.

1.4 Main research contents

Focused on the issues/problems identified above through a complete overview of the regional emissivity estimation methods from remotely sensed data, this work thus concerns on the methodological development permitting to determine both the temperature and surface emissivity from data of the SEVIRI (Spinning Enhanced Visible and Infra-Red Imager) instrument flown on the Second Generation of Meteosat satellites (MSG) and data from AMSR-E and MODIS instruments onboard the same Aqua platform. It is part of the CEOP-AEGIS project (Coordinated Asia-European long-term Observing system of Qinghai - Tibet Plateau hydrometeorological processes and the Asian monsoon systEm with Ground satellite Image data and numerical Simulations) funded by the European Commission under the programme FP7 for a period of 5 years from May 1, 2008. One of the objectives of this project is to develop methodologies for retrieving the geophysical parameters from satellite data.

This thesis is composedof six chapters.

In the above first chapter, the importance of the land surface emissivity is described first, and then the state of the art on the methodologies to estimate regional LSE from satellite data

in both TIR and MW spectral regions is given in detail, at the end of this chapter,the structure of this thesis is presented.

Chapter 2 recalls the fundamental principles of physics used in the determination of LSE from satellite data.

Chapter 3 is devoted to describe the sensors, data and models used in this work as well as the areas studied in this work.

Chapter 4 refers to the determination of LSE and LST from passive MV data.

Chapter 5 presents an improved algorithm to simultaneously retrieve both LSE and LST from SEVIRI data.

The conclusions of this work and some future trends and prospects are given in the sixth chapter.

Chapter 2

Fundamental radiometric theory

2.1 Thermal radiation

All substances at a finite absolute temperature emit electromagnetic energy (Ulaby et al., 1981). Any object that is hot gives off light known as thermal radiation. The hotter an object is the more energy it emits. As the temperature of the object increases, it emits most of its light at higher energy level (higher energy level means shorter wavelength light). The relationship between the amounts of energy emitted, its wavelength and temperature of the object is an equation known as the Planck Law.

2.1.1 Planck's Blackbody Radiation Law

In general, of the radiation incident upon the surface of a solid (or liquid) substance, a certain fraction is absorbed and the remainder is reflected. A blackbody is defined as an idealized, perfectly opaque material that absorbs all the incident radiation at all frequencies, reflecting none. The quantum-mechanical model of a blackbody may be described as consisting of such a large number of quantized energy levels with a correspondingly large number of allowable transitions, that any photon, whatever its energy or frequency, is absorbed when incident upon the blackbody. In addition to being a perfect absorber, a blackbody is also a perfect emitter, since energy absorbed by a material would increase its temperature if no energy is emitted.

According to Planck's radiation law, the spectral emittance of electromagnetic radiation from a blackbody is related to the temperature T (K):

$$E(T,\lambda) == \frac{2\pi c^2 h}{\lambda^5}\left(\exp\frac{ch}{k\lambda T}-1\right)^{-1} = \frac{C_1}{\lambda^5}\left(\exp\frac{C_2}{\lambda T}-1\right)^{-1}, \quad \left[W\cdot m^{-2}\cdot \mu m^{-1}\right] \tag{2.1}$$

where

$E(T,\lambda)$ is the energy that is quantifiable in terms of spectral emittance, defined as the energy per unit time per unit wavelength crossing an unit area perpendicular to the viewing direction of the sensor;

h is the Plank constant;

λ is the wavelength in μm;

c is the speed of light;

k is the Boltzmann constant;

$C_1 = 3.7418 \times 10^{-16} W \cdot m^2$ and $C_2 = 1.43877 \times 10^4 \, \mu m \cdot K$.

A blackbody radiates uniformly in all directions with a spectral radiance $B_{\lambda,T}$ given by

$$B_{\lambda,T} = \frac{E(T,\lambda)}{\pi}, \quad \left[W \cdot m^{-2} \cdot sr^{-1} \cdot \mu m^{-1} \right] \tag{2.2}$$

where $B_{\lambda,T}$ is Blackbody spectral radiance and it is the power per unit area per unit solid angle per unit wavelength.

It is sometimes of interest to express the spectral radiance on terms of $B_{f,T}$ ($f = frequency, cm^{-1}$) rather than $B_{\lambda,T}$, the radiance is given by

$$B_{f,T} = \frac{2hf^3}{c^2} \left(\exp \frac{hf}{kT} - 1 \right)^{-1}, \quad \left[W \cdot m^{-2} \cdot sr^{-1} \cdot cm \right] . \tag{2.3}$$

The total radiance B for a blackbody at a temperature T is the integral of $B_{f,T}$ (or $B_{\lambda,T}$) over all frequencies (or all wavelengths). One relationship was obtained, as written

$$B = \frac{\sigma T^4}{\pi}, \quad \left[W \cdot m^{-2} \cdot sr^{-1} \right] \tag{2.4}$$

which is known as the Stefan-Boltzmann law. Here,

σ is called the Stefan-Boltzmann constant. $\sigma = 5.673 \times 10^{-8} Wm^{-2} K^{-4} sr^{-1}$.

The low-frequency counterpart to the Wien radiation law is known as the Rayleigh-Jeans law. If $hf / kT \ll 1$, the approximation can be used to simplify equation (2.3) to

$$B_{f,T} = \frac{2f^2 kT}{c^2} = \frac{2kT}{\lambda^2} . \tag{2.5}$$

This approximation is very useful in the microwave region.

2.1.2 Non-blackbody radiation

A blackbody is an idealized body which, when in thermodynamic equilibrium at a temperature, radiates more energy than any other body at the same temperature. Actual materials emit less than a blackbody does and do not necessarily absorb the entire energy

incident upon them. An important parameter connected to the spectral radiance is the spectral emissivity, $\varepsilon(\theta,\lambda)$, which is the ratio of the spectral radiance actually emitted by an object at some temperature to the spectral radiance emitted by a blackbody at the same temperature given by equation (2.3). According to the definition, only the black body has an emissivity of 1, and the natural bodies are usually non-black bodies, $0<\varepsilon(\theta,\phi)<1$ $\lambda(\mu m)$ from a non-black body at temperature $T(K)$ is given by the spectral emissivity times the Planck's function:

$$R(\theta,\lambda)=\varepsilon(\theta,\lambda)B(T,\lambda)=\varepsilon(\theta,\lambda)\frac{2c^2h}{\lambda^5\left(\exp\frac{ch}{k\lambda T}-1\right)}. \tag{2.6}$$

If the spectral radiance, which may be direction-dependent, is $R(\theta, \lambda)$ and its physical temperature is T, a blackbody equivalent radiometric temperature, which is usually called the brightness temperature, $T_B(\theta)$, may be defined by.

$$B(T_B,\theta,\lambda)=R(\theta,\lambda)=\varepsilon(\theta,\lambda)B(T,\theta,\lambda). \tag{2.7}$$

In microwave region, the brightness temperature $T_B(\theta)$ of the material relative to that of a blackbody at the same temperature becomes:

$$T_B(\theta)=\varepsilon(\theta)T. \tag{2.8}$$

2.2 Emission and scattering

To examine quantitatively the interaction of radiation with a dielectric slab, the effective reflectivity ρ, the effective transmissivity$t$ and the effective absorptivity α are derived expressions, where the adjective "effective" refers to the steady-state solution incorporating all multiple reflections within the slab. These three parameters are related by:

$$\alpha+t+\rho=1. \tag{2.9}$$

If the material remains in thermodynamic equilibrium, its effective emissivity ε should be equal to α. Here,

$$\varepsilon+t+\rho=1, \tag{2.10}$$

which is a statement of energy conservation. For an opaque material, t = 0, in which case equation (2.10) reduces to

$$\varepsilon + \rho = 1 . \tag{2.11}$$

In the MW region, the emission and scattering by natural surface are dependent on roughness of surface, complex dielectric constant, temperature and scattering by surface. Specular reflection is the mirror-like reflections of wave from a surface, the reflectivity of horizontal and vertical polarization (ρ_{oh} and ρ_{ov}) are calculated by Fresnel's equations:

$$\rho_{oh} = \left| \frac{\cos\theta - \sqrt{\varepsilon' - \sin^2\theta}}{\cos\theta + \sqrt{\varepsilon' - \sin^2\theta}} \right|^2 , \tag{2.12}$$

$$\rho_{ov} = \left| \frac{\varepsilon'\cos\theta - \sqrt{\varepsilon' - \sin^2\theta}}{\varepsilon'\cos\theta + \sqrt{\varepsilon' - \sin^2\theta}} \right|^2 , \tag{2.13}$$

where

ε' is the land complex dielectric constant;

θ is the angle of incidence;

p is the polarisation(p = v or h);

ρ (the surface reflectivity) is a function of zenith angle, frequency, polarization and other physical parameters, e.g. temperature and salinity.

For the specular and opaque surface, the specular emissivity can be expressed in terms of the specular reflectivity through

$$\varepsilon(\theta, p) = 1 - \rho(\theta, p) . \tag{2.14}$$

For the rough surface, more general expressions of the emissivity should be given. Scattering by a rough surface is characterized by the bistatic scattering cross-section per unit area $\sigma^o(\theta_0, \phi_0; \theta_s, \phi_s; p_0, p_s)$ which relates the magnitude of the power scattered in the direction (θ_s, ϕ_s) with polarization P_s to the power incident in the direction (θ_0, ϕ_0) with polarization p_0 . (See Fig. 2.1). σ^o is also known as the surface scattering coefficient. If p_0 and p_s are both v or h, σ^o is called the vertically polarized or horizontally polarized

scattering coefficient, respectively, and if p_0 and p_s are different, it is known as the cross-polarized scattering coefficient ($\sigma^o(h,v) = \sigma^o(v,h)$).

Applying Kirchhoff's radiation law to the rough-surface case leads to the expression for the polarized emissivity $\varepsilon(\theta_s, \phi_s, p_s)$ of a surface observed from the direction (θ_s, ϕ_s) in terms of σ^o :

$$\varepsilon(\theta_s, \phi_s, p_s) = 1 - \frac{1}{4\pi} \int_0^{2\pi} \int_0^{\pi/2} \left[\sigma^o(\theta_0, \phi_0; \theta_s, \phi_s; p_s, p_s) + \sigma^o(\theta_0, \phi_0; \theta_s, \phi_s; p_0, p_s) \right] \frac{\sin\theta_0}{\cos\theta_s} d\theta_0 d\phi_0 . \tag{2.15}$$

In addition, radiation from remotely sensed objects in the earth's environment is attenuated in its passage through the atmosphere. The atmospheric transmissivity (*t*) is given by:

$$t = \exp(-\tau) = \exp\left(-\delta / \mu\right), \tag{2.16}$$

where

δ is the nadir optical depth;

μ is the cosine of view zenith angle (θ).

The nadir optical depth δ is defined as the integral over the height z of the volume extinction coefficient k_e

$$\delta(z) = \int_Z^{\infty} k_e(z) dz . \tag{2.17}$$

For the total nadir optical depth δ_0, the integral is taken from $z = 0$ to $z = \infty$.

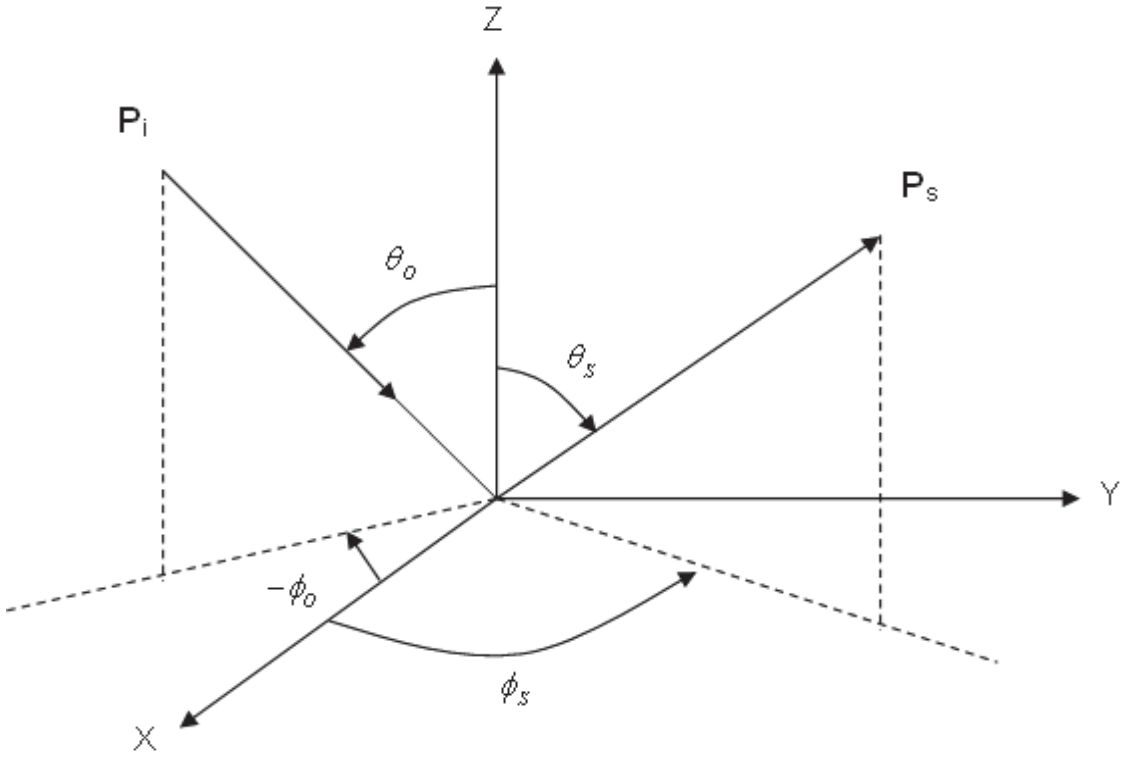

Figure 2.1 Geometry of incident and scattered radiation (Ulaby et al., 1982)

2.3 Radiative transfer equation

For the spectral radiance measured by a sensor at the top of the atmosphere (TOA), the atmospheric effects cannot be ignored. Atmospheric effects include absorption, emission and scattering (França and Cracknell, 1994). Fig. 2.2illustrates the different terms in the radiative transfer equation at a wavelength λ , all of these different terms together form the spectral radiance measured at TOA. As seen from this figure, the surface emission, which is a function of LST and LSE is denoted as [1] and expressed by the first term in the right-hand side of Eq. (2.20). Part of the spectral radiance emitted and scattered by the atmosphere reaches the surface, the so-called atmospheric downwelling radiance, and then reflected by the surface towards the sensor ([3] in Fig. 2.2). For the MIR spectrum in daytime, direct solar irradiance penetrates the atmosphere and part of it reaches the surface, and then is reflected by the surface towards the sensor ([4] in Fig. 2.2). The surface emission, the reflected atmospheric downwelling radiance and the reflected direct solar irradiance ([5] in Fig. 2.2) upwards penetrate the atmosphere and part of them reach the sensor after the absorption and scattering of the atmosphere，meanwhile the atmosphere emits and scatters the radiance directly upwards to the sensor ([6] in Fig. 2.2), which is called the atmospheric upwelling radiance. The total radiance reaching the sensor at wavelength λ is therefore written as:

$$R(\theta_v,\lambda) = R_G(\theta_v,\lambda)t(\theta_v,\lambda) + R_{atm\uparrow}(\theta_v,\lambda) + R_{s\uparrow}(\theta_v,\lambda), \quad (2.18a)$$

where

$R(\theta_v,\lambda)$ is the total radiance reaching the sensor;

λ is thewavelength;

θ_v is the view zenith angle;

$R_G(\theta_v,\lambda)$ is the total spectral radiance measured at ground level;

$t(\theta_v,\lambda)$ is the total atmospheric spectral transmittance;

$R_{atm\uparrow}(\theta_v,\lambda)$ is the upwelling atmospheric spectral radiance resulting from the scattering of solar radiance at zenith angle θ_v;

$R_{s\uparrow}(\theta_v,\lambda)$ is the upwelling atmospheric spectral diffusion radiance resulting from the scattering of solar radiance at zenith angle θ_v,

in term of brightness temperature, it can be expressed as

$$B(T_{B,S},\theta_v,\lambda) = B\left(T_{B,G},\theta_v,\lambda\right)t(\theta_v,\lambda) + R_{atm\uparrow}(\theta_v,\lambda), \quad (2.18b)$$

$T_{B,S}$ refers to the brightness temperature at satellite level;

$T_{B,G}$ is the brightness temperature at ground level;

with

$$\begin{aligned} R_G(\theta_v,\lambda) &= B\left(T_{B,G},\theta_v,\lambda\right) \\ &= \varepsilon(\theta_v,\lambda)B(T_s,\lambda) + \left[1-\varepsilon(\theta_v,\lambda)\right]\left[R_{atm\downarrow}(\lambda) + R_{s\downarrow}(\lambda)\right] + \rho_b(\theta_v,\theta_s,\varphi,\lambda)E_{sun}(\theta_s,\lambda) \end{aligned}, \quad (2.19)$$

where

$R_G(\theta_v, \lambda)$ is the total spectral radiance measured at ground level;

$\varepsilon(\theta_v, \lambda)$ is the emissivity of the land surface;

T_s is the land surface temperature;

1- $\varepsilon(\theta_v, \lambda)$ is the reflectivity of the land surface;

$R_{atm\downarrow}(\lambda)$ is the downwelling atmospheric spectral radiance;

$R_{s\downarrow}(\lambda)$ is the downwelling hemispheric solar diffusion radiance divided by π;

$\rho_b(\theta_v, \theta_s, \varphi,\lambda)$ is the bi-directional spectral reflectivity;

φ is the relative azimuth angle between the view azimuth angle and the solar azimuth angle;

θ_s is the solar zenith angle;

$E_{sun}(\theta_s, \lambda)$ is the direct solar spectral irradiance at ground level.

For the spectral radiance in TIR channels, MW channels and night-time measurements in middle infrared range (MIR) channels, $E_{sun}(\theta_s, \lambda) = 0$ and $R_{s\uparrow}(\theta_v, \lambda) = R_{s\downarrow}(\lambda) = 0$.

As the sensor onboard the satellite has finite range of spectral response, the radiance measured by the sensor in channel i, the so-called channel-averaged radiance, is can be written as (Li et al., 1999):

$$B_i(T_i,\theta_v) = \frac{\int_0^\infty f_i(\lambda)t(\theta_v,\lambda)B(T_{B,G},\theta_v,\lambda)d\lambda}{\int_0^\infty f_i(\lambda)d\lambda} + \frac{\int_0^\infty f_i(\lambda)\left[R_{atm\uparrow}(\theta_v,\lambda)+R_{s\uparrow}(\theta_v,\lambda)\right]d\lambda}{\int_0^\infty f_i(\lambda)d\lambda}, \quad (2.20)$$

where $f_i(\lambda)$ is the spectral response function of the channel i.

Similarly, the radiance measured in channel i at ground level is given by:

$$B_i(T_{g,i},\theta_v) = \frac{\int_0^\infty f_i(\lambda)\left\{\varepsilon(\theta_v,\lambda)B(T_s,\lambda)+\left[1-\varepsilon(\theta_v,\lambda)\right]\left[R_{atm\downarrow}(\lambda)+R_{s\downarrow}(\lambda)\right]+\rho_b(\theta_v,\theta_s,\varphi,\lambda)E_{sun}(\lambda)\right\}d\lambda}{\int_0^\infty f_i(\lambda)d\lambda} \quad (2.21)$$

where $T_{g,i}$ is the brightness temperature at ground level in the channel i.

For the channels with narrow spectral range (~1.0 μm), without introducing significant errors, Eqs. (2.20) and (2.21) can be approximated as (Li et al., 1999):

$$B_i(T_i,\theta_v) = t_i(\theta_v)B_i(T_{g,i},\theta_v) + R_{atm\uparrow i}(\theta_v) + R_{s\uparrow i}(\theta_v), \quad (2.22)$$

with

$$B_i(T_{g,i},\theta_v) = \varepsilon_i(\theta_v)B_i(T_s) + \left[1-\varepsilon_i(\theta_v)\right]\left(R_{atm\downarrow i}+R_{s\downarrow i}\right) + \rho_{b,i}(\theta_v,\theta_s,\varphi)E_{sun,i}(\theta_s). \quad (2.23)$$

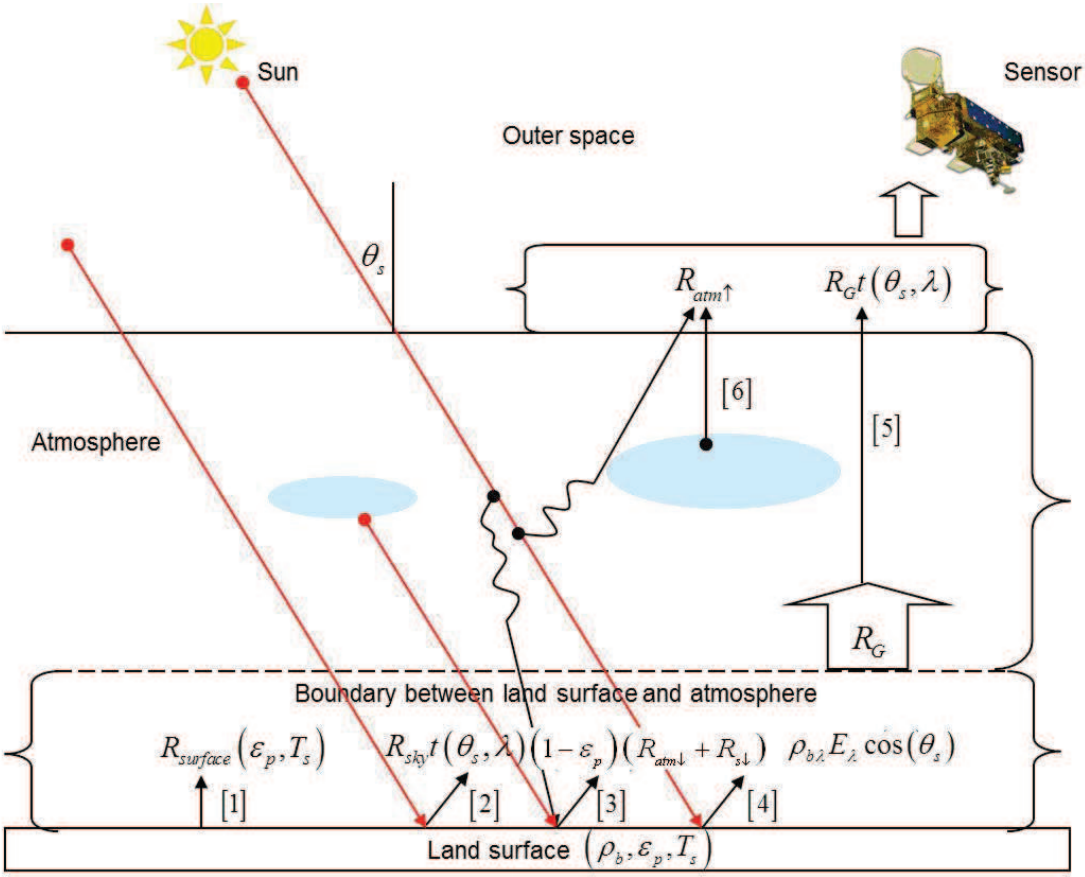

Figure 2.2 Radiative transfer at a wavelength λ (μm), [1] is the emission emitted by the surface; [2] is the space equivalent emission reflected by the surface; [3] is the downwelling atmospheric emission reflected by the surface; [4] is part of direct solar irradiance reaches the surface, and is reflected by the surface; [5] is the surface emission, the reflected atmospheric downwelling radiance and the reflected direct solar irradiance upwards penetrate the atmosphere and part of them reach the sensor; [6] is the upwelling atmospheric emission

In MW region, the brightness temperature at TOA is contributed by four components: the emission by the surface itself ([1] in Fig. 2.2) and attenuated by the atmosphere; the upwelling atmospheric emission ([6] in Fig. 2.2); the downwelling atmospheric emission reflected by the surface ([3] in Fig. 2.2) and attenuated by the atmosphere, and the space equivalent emission reflected by the surface ([2] in Fig. 2.2) and attenuated by the atmosphere. Therefore, assuming a scatter free atmosphere and a specular reflecting surface, the radiative transfer equation in MW region, expressed as brightness temperature at the TOA in the viewing direction θ_v, can be written as:

$$T_{f,p}(\theta_v) = T_{g,f,p} \times t_f(\theta_v) + T_{au,f}(\theta_v), \tag{2.24}$$

$T_{f,p}$ is the brightness temperature measured at TOA by a channel having frequency f and polarization mode p;

$T_{g,f,p}$ is the brightness temperature measured at ground by a channel having frequency f and polarization mode p;

t_f is the atmospheric transmittance at frequency f;

$T_{ad,f}$ is the downwelling atmospheric equivalent temperature at frequency f,

with

$$T_{g,f,p}(\theta_v) = \varepsilon_{f,p}(\theta_v) T_s + \left(1 - \varepsilon_{f,p}(\theta_v)\right)\left[T_{ad,f} + T_{sp} t_f(\theta_\varepsilon)\right], \tag{2.25}$$

$\varepsilon_{f,p}$ is the surface emissivity at frequency f and polarization mode p;

T_s is the surface temperature;

T_{sp} is the equivalent temperature of space, and has the constant value $T_{sp} = 2.7K$;

$\theta_\varepsilon = 54°$,

and

$$t_f(\theta) = \exp\left[-\tau_f(\theta)\right], \tag{2.26}$$

in which τ_f the optical depth of the atmosphere.

2.4 Atmospheric scattering

The earth's atmosphere plays an important role in remote sensing. It scatters and absorbs the incident energy and emits the energy in TIR and MW. Generally, the optical properties (e.g., optical depth, single scattering albedo, phase function) of the medium are determined by the particles that compose the medium and their properties. If the molecular particles in the atmosphere are far smaller than the wavelength (λ), scattering patterns can be calculated by the Rayleigh scattering law. For spherical particles, their scattering behaviours depend on the refractive index and size parameter defined as:

$$\chi = \frac{2\pi r_s}{\lambda}, \tag{2.27}$$

where r_s is the radius of the sphere.

If χ is smaller than 0.01, then the Rayleigh scattering formulas are valid. Rayleigh scattering is easy to handle in remote sensing because its principles are easily understood. The

only variable is the optical depth, which is quite stable globally. It depends mainly on the surface elevation (Russell et al., 1993) and can be calculated by:

$$\tau = \frac{P}{P_0}\left(0.00864 + 6.5\times10^{-6} z\right)\lambda^{-\left[3.916+0.074\lambda+\left(0.05/\lambda\right)\right]}, \qquad (2.28)$$

where

P is the ambient pressure in millibars;

P_0 = 1013.25 mbar;

z is the height above sea level (km);

λ is the wavelength (μm).

Since the optical depth decreases quickly as wavelength increases as shown in Eq. (2.28), taking Rayleigh scattering into account is meaningful only in the shorter wavelengths in this case.

If the particle size is close to the length of the wavelength ($0.1 < \chi < 50$), such as the most aerosol particles in the atmosphere, their scattering behaviour can be characterized by Mie theory.

2.5 Absorption by atmospheric gases

Atmospheric absorption is caused mainly by atmospheric gases, such as water vapor, carbon dioxide, ozone, oxygen. Through an understanding of the scattering, absorption, and emission behaviour of atmospheric constituents, microwave remote sensing techniques can be employed to monitor atmospheric parameters and weather conditions. Atmospheric absorption affects mainly the visible and infrared regions. The microwave spectrum offers a wide range of transmission conditions. In the 1-15 GHz region, the atmosphere is practically transparent even in the presence of clouds and moderate rainfall rates, which makes this frequency region especially attractive for terrain and ocean observations from satellite platforms (Ulaby et al., 1982).

In addition to oxygen and water vapor, other atmospheric gases and pollutants have absorption lines. The attenuation coefficient is defined as the sum of absorption and scattering coefficients of atmosphere

According to the quantum theory, the absorption (or emission) spectrum of a molecule consists of sharply defined frequency lines corresponding to transitions between sharply defined (quantized) energy levels of the molecule.

2.5.1 Water vapor absorption

Water vapor has most significant absorption for electromagnetic radiation, and has rotational absorption lines in both TIR and MW region. Distribution of water vapor varies widely over time and location. The greater the water vapor content, the more serious the absorption is. In TIR region, there are many water vapor absorption bands: two strong absorption bands, 4.9~8.7 μm and 2.27~3.57 μm; two narrow absorption bands, 1.38 μm and 2.0 μm; one narrow weak absorption band, 0.7~1.23 μm. In MW region (1-200 GHz), there are two water vapor absorption lines, one at 22.235 GHz and another at 183.31 GHz.

2.5.2 Carbon dioxide

Carbon dioxide is one of the most important infrared absorption gases in Earth's atmosphere. Its absorption bands are mainly located in the infrared region greater than 2 μm. There are four main carbon dioxide absorption bands: one around 4 μm, one absorption band from 14~18 μm and two narrow absorption bands at1.38 μm and 2.0 μm.

2.5.3 Ozone absorption

Ozone is a tri-atomic molecule, consisting of three oxygen atoms. It is an allotrope of oxygen that is much less stable than the diatomic allotrope. In the upper atmosphere, the sun's ultraviolet radiation breaks down oxygen molecules into atoms. The oxygen atoms then combined to a three atoms molecule (ozone) in certain conditions. Ozone is mainly in the 10 to 40 km altitude of atmosphere.

Ozone absorbs all the short-wave solar radiation under 0.3 μm, but it is very weak in long-wave absorption, except for a narrow TIR absorption band around 9.6 μm.

2.5.4 Oxygen absorption

Absorption spectrum of oxygen consists of a large number of absorption lines spread out over the 50-70 GHz frequency range (known as the 60 GHz oxygen complex) and an

additional line at 118.75 GHz. As characteristic of the lower part of the earth's atmosphere, pressure broadening causes the complex of lines to blend together, forming a continuous absorption band centred around 60 GHz (Ulaby et al., 1980).

2.5.5 Extinction by clouds and precipitation

The interaction of electromagnetic radiation with particles (such as those in clouds, or rain) is different in nature and may involve both absorption and scattering. The volume extinction coefficient is governed by the density, shape, size distribution, and dielectric properties of the particles contained in the volume. In extending the results for a single particle to the ensemble containing many particles, the particles usually are assumed to be randomly distributed within the volume, and therefore the contributions of the individual particles can be summed assuming an incoherent process. In addition to the above assumptions, spherical particles are further assumed.

Chapter 3

Data collection and pre-processing

3.1 Study areas

3.1.1 Study area for retrieving LSE from MW data (study area A and C)

Both MW data and TIR data onboard satellite Aqua over the whole China, covering area from longitude 71.875°E to 134.875°E and from latitude 4.125°N to 54.125°N, are used to map LSE in different MW channels using the method proposed in this thesis for the whole year 2006.

The China's vast size gives it a wide variety of landscapes and climates. A major environmental issue in China is the continued expansion of its deserts. China's climate is mainly dominated by dry seasons and wet monsoons, which lead to a pronounced temperature differences between winter and summer. In the winter, northern winds coming from high-altitude areas are cold and dry; in summer, southern winds from coastal areas at lower altitudes are warm and moist. The climate in China differs from region to region because of the country's extensive and complex topography. Fig. 3.1 displays the global NDVI image. The area encompassed in the red rectangle denoted as A on this image is our study area (China) for mapping LSE from MW data.

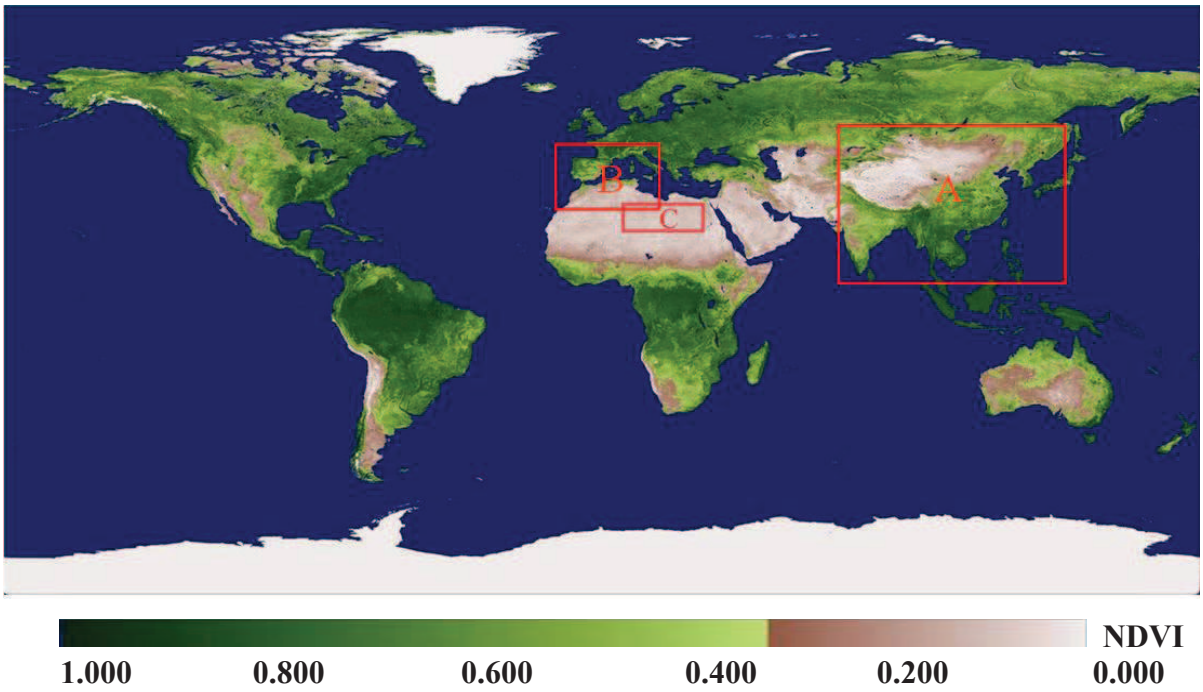

Figure 3.1 The NDVI over world of the 2007

Considering the low resolution of microwave data, another study area encompassed in the red rectangle denoted as C in Fig. 3.1 is our study area (in Saharan Africa spanning from

24.89°N to 29.27°N and 9.89°E to 28.11°E) for LSE retrieval from MW data. This study area is part of the Saharan Africa, with geospatial coverage of latitude 24.89° N to 29.27° N and longitude 9.89° E to 28.11° E.

3.1.2 Study area for retrieving LSE from TIR data (study area B)

A study area encompassed in the red rectangle denoted as B in Fig. 3.1 is our study area for mapping LSE from TIR data. This study area is composed of the Iberian Peninsula and part of the Maghreb, with geospatial coverage of latitude 30° N to 45° N and longitude 15° W to 15° E. The Iberian Peninsula is the westernmost section of the European continent, lying between the Mediterranean Sea and the Atlantic Ocean, occupied by Spain and Portugal. It is dominated by two major climatic groups, namely, the Oceanic or Western Coastal Maritime to the North and the Mediterranean climate, which influences the southern two-thirds of the peninsula. As displayed in land use/land cover (LULC) map (Fig. 3.2), which is generated from the global land cover 2000 produced by the Institute for Environment and Sustainability (IES), the representative LULC in Iberian Peninsula typically consist of cultivated and managed areas (about 53%), tree cover (about 35%) and shrub cover (about 9%). The Maghreb is primarily defined through a series of physical geographic features that separate the area from the rest of Africa. It includes the Northern African nations of Algeria, Tunisia and Morocco and is covered by the Sahara desert and Atlas Mountains. The north of the Maghreb in the study area is dominated by shrub (about 9%) and herbaceous (about 26%), while the south is dominated by bare area (about 52%). Climatically, the Maghreb has a Mediterranean climate in the north, and has the arid in the south.

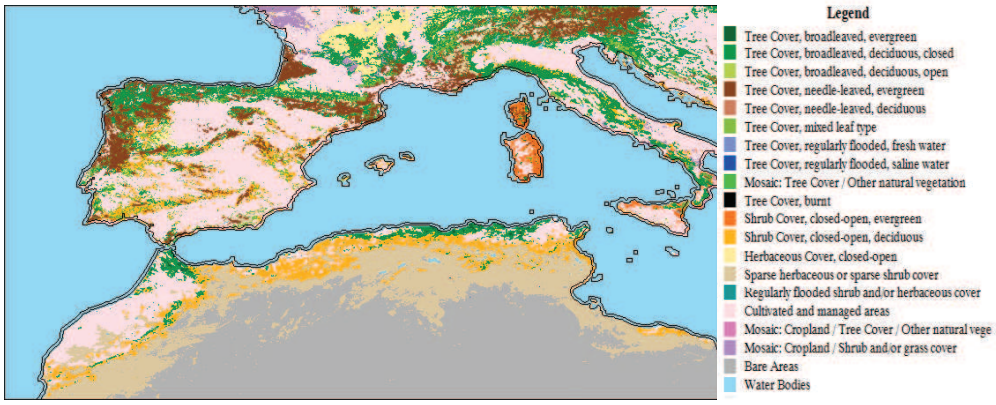

Figure 3.2 The land cover of the study area, generated from the Global Land Cover 2000 produced by IES (**http://bioval.jrc.ec.europa.eu/products/glc2000/products.php**)

3.2 Satellite data and related data

3.2.1 Aqua satellite

The Aqua mission is a part of the NASA-centered international Earth Observing System (EOS). Launched from Vandenderg Air Force Base on May 4th, 2002, the satellite has six different Earth-observing instruments onboard for studies of water on the Earth's surface and in the atmosphere. These six instruments include Advanced Microwave Scanning Radiometer-EOS (AMSR-E); Moderate Resolution Imaging Spectroradiometer (MODIS); Advanced Microwave Sounding Unit (AMSU-A); Atmospheric Infrared Sounder (AIRS); Humidity Sounder for Brazil (HSB) and Clouds and the Earth's Radiant Energy System (CERES). Aqua is polar orbiting with 1:30 A.M. (descending pass)/P.M. (ascending pass) in local time. It is a near-polar low-Earth orbit.

Table 3.1 Aqua (EOS PM-1) orbit information

Operator;	**Launch date;**	**Inclination;**	**Apoapsis;**	**Periapsis;**	**Orbital period;**
NASA;	May 4th, 2002;	98.14°;	708km;	691km;	98.4minutes;

3.2.2 AMSR-E data

The AMSR-E is a twelve-channel, six-frequency (dual polarized), total power passive-microwave radiometer system. It measures brightness temperatures at 6.925, 10.65, 18.7, 23.8, 36.5 and 89.0 GHz with two polarized (vertically and horizontally) measurements taken in all frequencies. The Earth-emitted microwave radiation is collected by an offset parabolic reflector 1.6 meters in diameter that scans across the Earth along an imaginary conical surface, maintaining a constant Earth incidence angle of 55° and providing a swath width array of six feed horns which then carry the radiation to radiometers for measurement. Calibration is accomplished with observations of cosmic background radiation and an on-board warm target. The main operating parameters and characteristics of AMSR-E are shown in Table 3.2.

The AMSR-E gridded brightness temperature data produced at 0.25° resolution by the US National Snow and Ice Data Center (NSIDC) are used in this study.

Table 3.2 AMSR-E performance characteristics

Polarization	Horizontal and Vertical					
Incidence angle (degree)	55					
Cross-polarization (dB)	Less than -20					
Swath (km)	1445					
Center frequency (GHz)	6.925	10.65	18.7	23.8	36.5	89.0
Bandwidth (MHz)	350	100	200	400	1000	3000
Sensitivity (K)	0.3	0.6	0.6	0.6	0.6	1.1
IFOV (km)	74×43	51×30	27×16	31×18	14×8	6×4
Sampling interval (km)	10×10	10×10	10×10	10×10	10×10	5×5
Integration time (msec)	2.6	2.6	2.6	2.6	2.6	1.3
Main beam efficiency (%)	95.3	95.0	96.3	96.4	95.3	96.0
Beamwidth (degree)	2.2	1.4	0.8	0.9	0.4	0.18

3.2.3 MODIS data

MODIS is a key instrument aboard the Terra (EOS AM) the Aqua (EOS PM) satellites. Terra MODIS and Aqua MODIS are viewing the entire Earth's surface every 1 to 2 days, acquiring data in 36 spectral bands, or groups of wavelengths. Its channel characteristics are listed in Table 3.3.

Daily global LST product (MOD11C1/MYD11C1 Daily CMG LST) at 0.05 degree latitude/longitude resolution are used (1) as a reference LST to cross validate LST derived from SEVIRI data using the method improved in this thesis; (2) as a true LST detected by MW channels to retrieve LSE from AMSR-E data.

Table 3.3 Channel characteristics

Primary Use	Band	Bandwidth[1]	Spectral Radiance[2]	Required SNR[3]
Land/Cloud/Aerosols	1	620 - 670	21.8	128
Boundaries	2	841 - 876	24.7	201
Land/Cloud/Aerosol	3	459 - 479	35.3	243
s	4	545 - 565	29.0	228
Properties	5	1230 - 1250	5.4	74
	6	1628 - 1652	7.3	275
	7	2105 - 2155	1.0	110
Ocean Color/	8	405 - 420	44.9	880
Phytoplankton/	9	438 - 448	41.9	838
Biogeochemistry	10	483 - 493	32.1	802
	11	526 - 536	27.9	754
	12	546 - 556	21.0	750
	13	662 - 672	9.5	910
	14	673 - 683	8.7	1087
	15	743 - 753	10.2	586
	16	862 - 877	6.2	516
Atmospheric	17	890 - 920	10.0	167
Water Vapor	18	931 - 941	3.6	57
	19	915 - 965	15.0	250
Primary Use	**Band**	**Bandwidth[1]**	**Spectral Radiance[2]**	**Required NEΔT(K)[4]**
Surface/Cloud	20	3.660 - 3.840	0.45(300K)	0.05
Temperature	21	3.929 - 3.989	2.38(335K)	2.00
	22	3.929 - 3.989	0.67(300K)	0.07
	23	4.020 - 4.080	0.79(300K)	0.07
Atmospheric	24	4.433 - 4.498	0.17(250K)	0.25
Temperature	25	4.482 - 4.549	0.59(275K)	0.25
Cirrus Clouds	26	1.360 - 1.390	6.00	150(SNR)
Water Vapor	27	6.535 - 6.895	1.16(240K)	0.25
	28	7.175 - 7.475	2.18(250K)	0.25
Cloud Properties	29	8.400 - 8.700	9.58(300K)	0.05
Ozone	30	9.580 - 9.880	3.69(250K)	0.25
Surface/Cloud	31	10.780 - 11.280	9.55(300K)	0.05
Temperature	32	11.770 - 12.270	8.94(300K)	0.05
Cloud Top	33	13.185 - 13.485	4.52(260K)	0.25
Altitude	34	13.485 - 13.785	3.76(250K)	0.25
	35	13.785 - 14.085	3.11(240K)	0.25
	36	14.085 - 14.385	2.08(220K)	0.35

[1]Bands 1 to 19 are in nm; Bands 20 to 36 are in μm
[2]Spectral Radiance values are (W/m^2-μm-sr)
[3]SNR = Signal-to-noise ratio
[4]NEΔT = Noise-equivalent temperature difference
Note: Performance goal is 30-40% better than required

3.2.4 MSG-2/SEVIRI data

Meteosat Second Generation (MSG) is a series of four geostationary satellites developed by European Space Agency (ESA) and EUMETSAT, the latest satellite MSG-2 was launched in December 2005. Its main payload SEVIRI images an Earth disk with view zenith angle (VZA) ranging from 0° to 80° with 3-km nadir spatial resolution, and provides data in 12

spectral bands (three visible and near-infrared bands, eight infrared bands and a visible broadband band, see Table3.4 every 15 minutes, making it particularly suitable for LSE determination on the day/night TISI concept and then deriving LST with split-window method. The spectral responses function for SEVIRI channels 4, 7, 9 and 10 are shown in Fig. 3.3. SEVIRI data are used to test and develop the improvement of LSE retrieval method from TIR data in this thesis.

Table 3.4 Spectral channel characteristics of MSG-2/SEVIRI instrument

Channel No.	Channel name	Characteristics of spectral channel (μm)			Radiometric error performances	Main gaseous absorber or window
		$\lambda_{central}$	λ_{min}	λ_{max}		
1	VIS0.6	0.653	0.56	0.71	0.27 at 5.3 $Wm^{-2}sr^{-1}\mu m^{-1}$	Window
2	VIR0.8	0.81	0.74	0.88	0.21 at 3.6 $Wm^{-2}sr^{-1}\mu m^{-1}$	Window
3	NIR1.6	1.64	1.50	1.78	0.07 at 0.75 $Wm^{-2}sr^{-1}\mu m^{-1}$	Window
4	IR3.9	3.92	3.48	4.36	0.17 K at 300 K	Window
5	WV6.2	6.25	5.35	7.15	0.21 K at 250 K	Water vapor
6	WV7.3	7.35	6.85	7.85	0.12 K at 250 K	Water vapor
7	IR8.7	8.70	8.30	9.10	0.10 K at 300 K	Window
8	IR9.7	9.66	9.38	9.94	0.29 K at 255 K	Ozone
9	IR10.8	10.8	9.80	11.8	0.11 K at 300 K	Window
10	IR12.0	12.0	11.00	13.0	0.15 K at 300 K	Window
11	IR13.4	13.40	12.40	14.4	0.37 K at 270 K	Carbon dioxide
12	HRV	0.75	Broadband visible		0.63 at 1.3 $Wm^{-2}sr^{-1}\mu m^{-1}$	Window /watervapor

*Central wavelength was calculated by $\lambda_{central} = \int_0^\infty \lambda f_i(\lambda) d\lambda / \int_0^\infty f_i(\lambda) d\lambda$

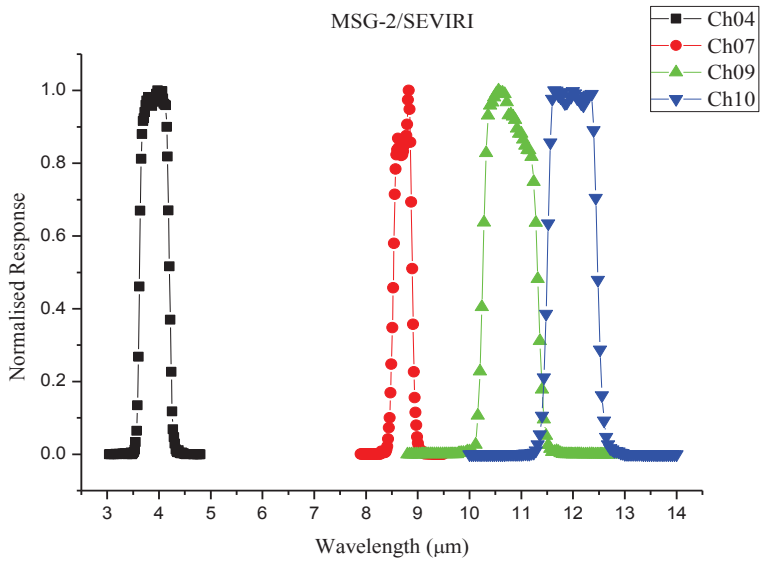

Figure 3.3 Normalized spectral function response of SEVIRI channels 4, 7, 9 and 10

3.2.5 Cloud MASK

Another useful product is the MSG cloud mask. The MSG cloud mask product is an image-based product derived from the results of scenes analysis and provides, for every cycle, information on the possible occurrence of clouds within each pixel. A central objective is to delineate all absolutely cloud-free pixels in a satellite scene with a high degree of confidence. The MSG cloud mask product provides the following information: (1) no cloud, clear surface; (2) no cloud, surface types snow/ice; (3) no cloud, sun-glint over sea; (4) cloudy, 50%, 75% and 100% probabilities; (5) no-processed or missing data. The MSG cloud mask data are stored in the Native files and are used to select SEVIRI data for clear sky in this study (http://archive.eumetsat.org).

3.2.6 Synchronous atmospheric quantities

The atmospheric quantities for atmospheric correction are estimated from the atmospheric profile data provided by European Centre for Medium-Range Weather Forecasts (ECMWF) at 00:00, 06:00, 12:00 and 18:00 UTC. Atmospheric profile data have 21 levels and cover from Latitude -10°N to 60°N and Longitude -20°E to 160°E at a spatial resolution of 1°×1° over the whole year 2006 for study area A (see Table 3.5). However, over the whole year 2008 for study area B, 25 levels at a spatial resolution of 0.25°×0.25° are available (see Table 3.6).

Table 3.5 Description of the ECMWF data of the year 2006 used for atmospheric correction of AMSR-E data

Data: Pressure (hPa), air temperature (K), relative humidity (%) and geo-potential (GP)		
Sampling	**Step**	**Limits**
Temporal	6hours	
Geographical: Latitude	1°	10°S-60°N
Geographical: Longitude	1°	20°W-160°E
Vertical	21 levels*	To altitude about 48 km

*Levels of pressure are 1000, 925, 850, 700, 500, 400, 300, 200, 150, 100, 70, 50, 30, 20, 10, 7, 5, 3, 2 and 1hPa

Table 3.6 As table 3.5, but for atmospheric correction of SEVIRI data in year 2008

Data: Pressure (hPa), air temperature (K), relative humidity (%) and geo-potential (GP)		
Sampling	**Step**	**Limits**
Temporal	6hours	
Geographical: Latitude	0.25°	0°N-60°N
Geographical: Longitude	0.25°	20°W-40°E
Vertical	25 levels*	

*Levels of pressure are 1000, 950, 925, 900, 850, 800, 700, 600, 500, 400, 300, 250, 200, 150, 100, 70, 50, 30, 20, 10, 7, 5, 3, 2 and 1hPa.

3.2.7 DEM

HYDRO1k, developed at the U.S. Geological Survey's (USGS) EROS Data Center (http://esp.cr.usgs.gov/), is a geographic database providing comprehensive and consistent global coverage of topographically derived data sets. Developed from the USGS' recently released 30 arc-second digital elevation model (DEM) of the world, HYDRO1k provides a standard suite of geo-referenced data sets (at a resolution of 1 km) that will be valuable for all users who need to organize, evaluate, or process geographic information on a continental scale. The DEM is used to modify the atmospheric profiles from ECMWF.

3.3 Data pre-processing

3.3.1 MODIS data pre-processing

As MODIS and AMSR-E are both onboard on the same satellite Aqua, MODIS LST product can be used as a true LST detected by MW to retrieve LSE from AMSR-E data. Due to the different spatial resolutions of these two products as described in sections 3.2.2 and 3.2.3, they should be matched spatially. To get LST at AMSR-E pixel scale from MODIS LST product, first MODIS pixels have to be matched spatially with AMSR-E pixel using a simple coordination matching (longitude/latitude matching) method as illustrated in Fig. 3.4

control condition. Secondly, the average of all of MODIS LSTs corresponding to clear sky within an AMSR-E pixel is computed using Eq. (3.1) leading to a LST measured at 0.25°× 0.25° (AMSR-E pixel resolution).

$$T_{AMSR-E} = \sum_{i=1}^{20 \le N \le 25} T_{MODIS}^{i} \Big/ N \tag{3.1}$$

where

$T_{AMSR\text{-}E}$ is the LST at AMSR-E pixel;

T_{MODIS}^{i} is the MODIS-derived LST corresponding to the ith MODIS pixel within an AMSR-E pixel;

N is the total number of MODIS clear pixels within an AMSR-E pixel. If N<20, the AMSR-E pixel is discarded in this study.

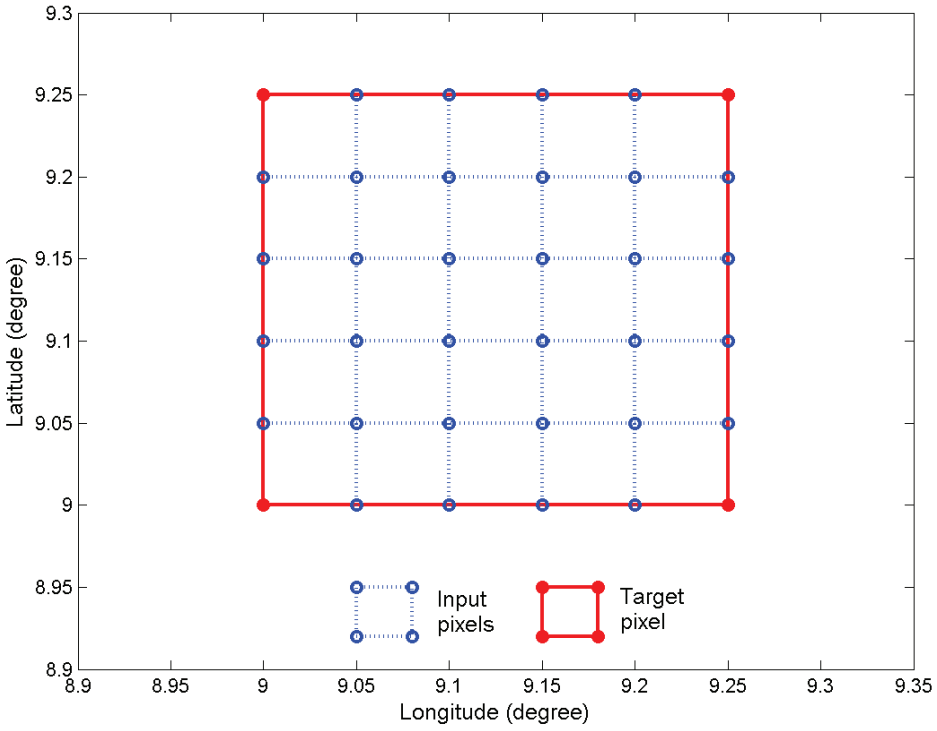

Figure 3.4 Illustration of coordination matching between AMSR-E and MODIS pixels. The red rectangle represents an AMSR-E pixel and small blue rectangle represents an MODIS pixel

3.3.2 Estimation of atmospheric quantities at spatial resolution of AMSR-E pixel from the quantities at 1°×1°

The atmospheric profiles provided by the ECMWF mainly include pressure (P), temperature (T), relative humidity (RH) and geo-potential (GP) for each pressure level from 1000hpa to 1hpa. To make these atmospheric profiles suitable for atmospheric correction with the radiative transfer models, they have to be merged with DEM data to take into account the topographic variation. These modified atmospheric profiles are then used to calculate the atmospheric quantities (transmittance, upwelling and downwelling atmospheric radiance) at resolution of 1°×1° with radiative transfer models such as Modtran and MonoRTM. Finally, the bilinear spatial interpolation method is employed to obtain the atmospheric quantities at spatial resolution of 0.25°×0.25° from those at spatial resolution of 1°×1°.

3.3.3 MODTRAN

MODTRAN (MODerate resolution atmospheric TRANsmission and radiance) code is a computer program designed to model atmosphericpropagation of electromagnetic radiationfor the 100-50,000 cm^{-1} (0.2 to 100 μm) spectral range. MODTRAN code calculates atmospheric transmittance and radiance for frequencies from 100 to 50,000 cm^{-1} at moderate spectral resolution, primarily $2cm^{-1}$ ($20cm^{-1}$ in the UV).

MODTRAN 4.0 is the current version of MODTRAN. Compared with MODTRAN 3, it adds some new features, such as two Correlated-K (CK) options, azimuth dependent DISTORT option, upgraded ground surface modelling, high-speed option, making the calculation more accurate than the former version (Berk et al., 1998; MODTRAN 4.0 User's Manual).

MODTRAN prescribes six standard model atmospheres: Tropical, Mid-Latitude Summer, Mid-Latitude Winter, Sub-Arctic Summer, Sub-Arctic Winter and 1976 U.S. Standard. The air temperatures of the first boundary and the total column water vapor contents of these six standard atmospheres are listed in Table 3.7.

In addition to the six standard model atmospheres, MODTRAN also provides New Model Atmosphere option to enable users to define their own atmospheric profiles, such as radio sounding data or ECMWF data.

MODTRAN 4.0 is used in this work to estimate the atmospheric quantities, which are used to perform atmospheric corrections in TIR and middle infrared (MIR).

Table 3.7 Air temperature at the first boundary and the total water vapor contents of the six standard model atmospheres prescribed in MODTRAN

Model atmosphere	T_0(K)	W(g/cm^2)
Tropical	299.7	4.11
Mid-Latitude Summer	294.2	2.92
Mid-Latitude Winter	272.2	0.85
Sub-Arctic Summer	287.2	2.08
Sub-Arctic Winter	257.2	0.42
1976 U S Standard	288.2	1.42

*T_0 is the air temperature at the first boundary and W represents the total column water vapor content.

Chapter 4

LSE and LST retrieval from AMSR-E data

4.1 Introduction

Land surface remote sensing satellite observations are affected by both the land surface and the atmosphere. To retrieve land surface parameters from a satellite measurement, the influence of atmosphere must first be removed.

The influence of the atmosphere on the measurement and retrieval of LSE and LST, using infrared remote sensing data, is obvious and needs to be considered (Li et al.,2013a; Li et al, 2013b; Nerry et al., 2004; Ouyang et al., 2010). Compared to optical and infrared remote sensing, passive MW remote sensing is considered to be an effective tool for all-weather monitoring of land surface processes. The long wavelengths used in passive MW remote sensing resist atmospheric disturbances and are even able to penetrate clouds and some rainfall. Therefore, after correcting for the atmosphere, passive MW remote sensing data can be used to retrieve land surface parameters under almost any weather conditions.

Satellite data simulation must be performed with an accurate radiative transfer model to develop methodologies for LSE and LST retrievals from passive MW data. Unfortunately, there is still a lack of the soil-atmosphere radiative transfer model in MW region, the influences of soil physical properties, atmospheric properties, surface roughness and vegetation are also unclear. Therefore, one of the objectives of this chapter is to develop a comprehensive soil-atmosphere radiative transfer model in MW, which is used subsequently to propose LST and LSE retrieval methods.

To date, a great deal of attention has been paid to the use of space-borne passive MW data. In previous studies, at low MW frequencies, the atmospheric effects are usually considered to be negligible. The observed brightness temperature was used to estimate land surface parameters without atmospheric correction. By contrast, at high frequencies, atmospheric effects on observations should be considered, and it is necessary to correct for atmospheric effects before the data can be used. Meteorological reanalysis and radiosonde data have typically been used to estimate the atmospheric parameters and remove atmospheric effects in previous research (Prigent et al., 1997; Karbou et al., 2005). However, it is difficult to match both the time and location of different data sources, which may introduce errors into the retrieval process and lead to larger uncertainties in the estimation of land surface parameters. Although some researches on atmospheric effects and correction algorithms has been performed (Snider et al., 1994), there is little quantitative analysis describing the atmospheric

effects on AMSR-E data or on when it is necessary to correct for atmospheric conditions. One of the objectives of this chapter is to first analyze atmospheric effects on AMSR-E data and then to propose an atmospheric correction algorithm at 18.7 GHz vertical polarization for LST retrieval.

LSE is essential for deriving land surface geophysical parameters from remotely sensed data. In many applications, the uncertainty in LSE directly affects the accuracies of the estimated parameters, such as LST and soil moisture. In reality, it is difficult to obtain LSE from passive radiometers because the number of measurements is always less than the number of unknowns. Although more accurate physics-based models have been developed in the past decades (Chen et al., 2003; Fung et al., 1992; Fung et al., 1994; Tsang et al., 1985; Ulaby et al., 1982), their complexity often makes them difficult to use for retrieving geophysical parameters. To make the solutions deterministic, additional assumptions, semi-empirical relationships and extra constraints have been used in previous studies (Choudhury et al., 1979; Fily et al., 2003; Gao et al., 2008; Jones et al., 2007; Mo and Schmugge, 1987; Prigent et al., 2003; Shi et al., 2005; Wang and Choudhurry, 1981; Wegmuller and Matzler, 1999; Weng and Grody, 1998; Wigneron et al., 2001). One of objectives of this chapter is to first develop a parameterized relationship between the vertical and horizontal polarization emissivities that is helpful in understanding the emission of a natural surface and then to propose an algorithm for retrieving LSE from AMSR-E data in combination of MODIS LST product.

4.1.1 Land surface model (AIEM)

Random surface roughness is commonly described by two statistical parameters: root mean square height (s) and surface correlation length (l). Electromagnetically, a surface is considered smooth if its height (z) variations are much smaller than the wavelength of the radiation. As rough surface scatters the incident energy in all direction, its characterization is very important for describing land surface-atmosphere interaction in MW. Root mean square height (s) and surface correlation length (l) are mathematically expressed as:

$$s = \left[\frac{1}{N-1} \left(\sum_{i=1}^{N} (z_i)^2 - N\left(\bar{z}\right)^2 \right) \right]^{1/2}, \tag{4.1}$$

with

$$\bar{z} = \frac{1}{N}\sum_{i=1}^{N} z_i \,. \tag{4.2}$$

On the other hand, the surface correlation function ρ (x) and l, are parameters used for the horizontal description of the surface roughness. In the discrete case, the normalised surface correlation function for a spatial displacement $x' = (j\text{-}1)\triangle x$ is given by

$$\rho(x') = \sum_{i=1}^{N+1-j} z_i z_{j+i-1} \Big/ \sum_{i=1}^{N} z_i^{\,2} \,, \tag{4.3}$$

in which z_{j+i-1} is a point with the spatial displacement from the point x_i (Fung, 1994). The l is defined as the displacement x' for which ρ (x') between two points inhibits values smaller than 1/e (Euler's Value $\approx$ 2.7183)

$$\rho(l) = 1/e \,. \tag{4.4}$$

Thus, the surface correlation describes the statistical independence of two points on a surface and increases with the correlation between two neighbouring points. For a smooth surface $l = \infty$.

In this chapter, the Advanced Integral Equation Model (AIEM) is used to calculate the emissivity of rough land surface. AIEM is an improved version of Integral Equation Model (IEM), hereafter called advanced IEM (AIEM). Generally, the AIEM model provides a simple and accurate connection between the surface emission at different frequencies and polarization, as well as the commonly used surface roughness parameter measurements. It can be applied to the measurements from both single-pass and multi-pass measurements for the time series analyses.

The AIEM retained the absolute phase term in Green's function so that the upward and downward re-radiation over the surfaces is included (Jiang et al., 2012). AIEM model uses the Dobson module to calculate the soil dielectric constant. This model was used for built a complete theoretical simulation land surface emissivity database. The database is used to the next step calculation; the Fig. 4.1 shows the input parameters and the modules which composited the AIEM model.

Dielectric constant, which is estimated by DOBSON module, is very important input parameters for AIEM model to calculate emissivity and reflectivity. The major input

parameters of DOBSON include frequency, temperature, soil moisture and some land surface parameters (volumetric contents of sand, volumetric contents of soil, volumetric contents of clay). The soil temperature is set to be between 0 to 40℃with a step of5℃; according to soil physics, soil moisture is set to be between 2% to 44% with a step of 2%; the volumetric contents of soil solid is 0.4 to 0.7, step is 0.05; the combination of sand and clay is based on the international soil texture classifications which is a qualitative classification tool used to determine classes for soils based on their physical texture, the range is from 0% to 100% with a step of 10%.

The incidence angle, land surface correlation length and land surface root mean square (RMS) height are inputs for AIEM model. We set the land surface correlation length from 2.5cm to 30cm with a step of 2.5cm and the land surface RMS height from 0.25cm to 3.0cm with a step of 0.25cm. The emissivities and reflectivities are outputs of AIEM model.

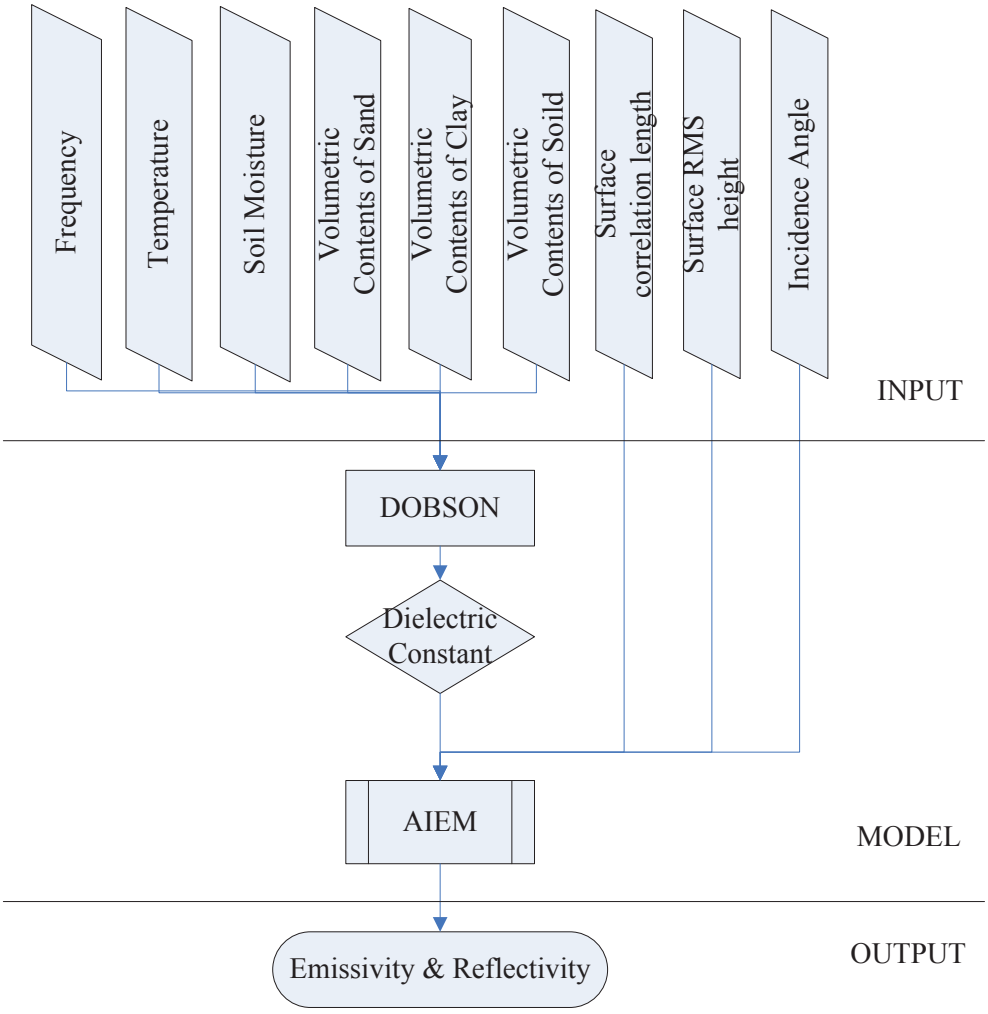

Figure 4.1 Simulation of LSE from AIEM

4.1.2 Atmospheric radiative transfer model (MonoRTM)

The key issue to accurately estimate the land surface radiance from at-sensor radiance is to get the accurate influence of atmosphere. In order to research the influence of atmosphere, this thesis uses the MONOchromaticRadiative Transfer Model (MonoRTM) which is particularly useful in the MW spectral region. The Fig. 4.2 shows the input parameters, the output parameters and the modules which composited the MonoRTM model.

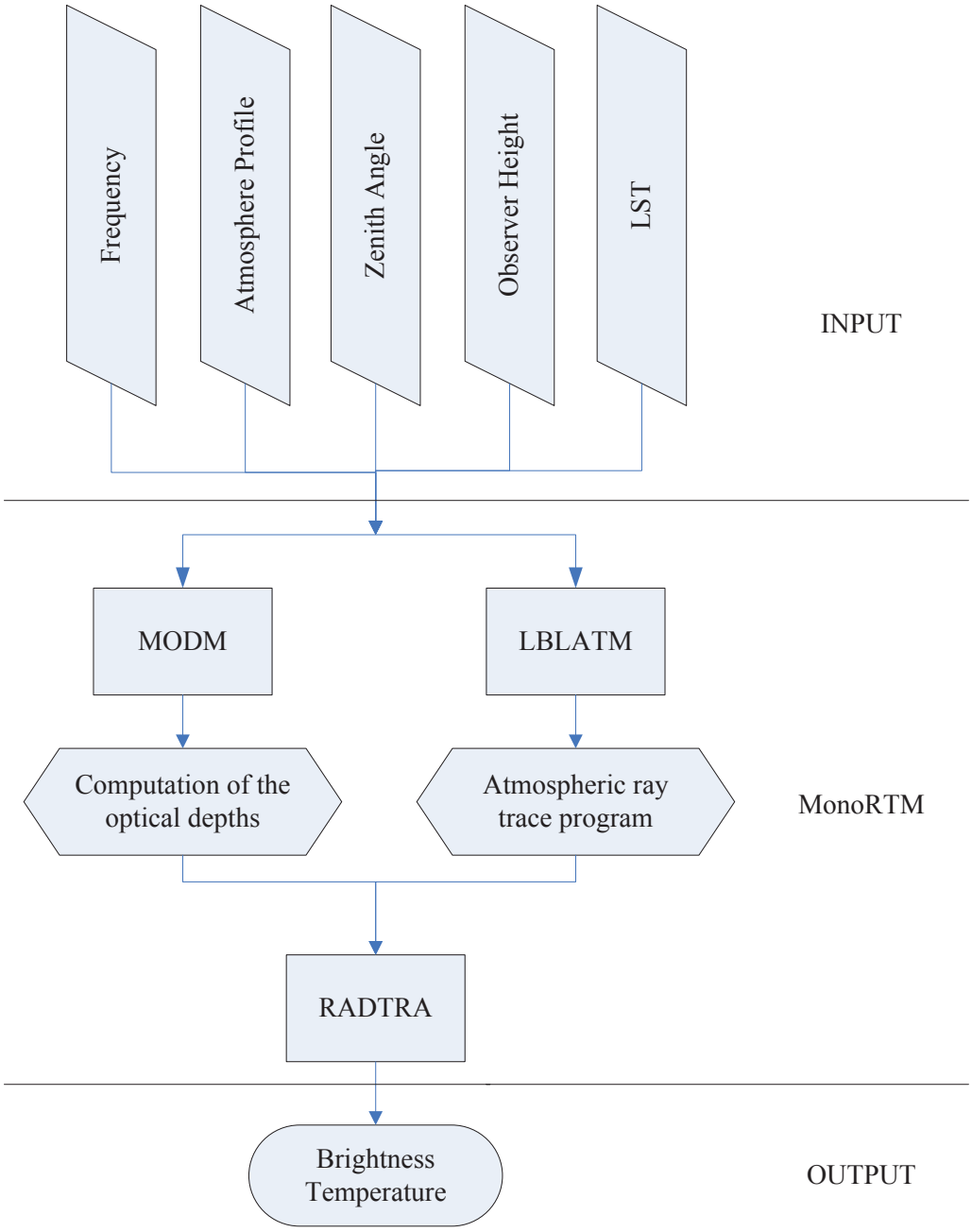

Figure 4.2 MonoRTM

MonoRTM is a radiative transfer model, designed to process one or a number of monochromatic wave number values. It was developed and distributed by Atmospheric and Environmental Reasearch, Inc. The model is publicly available and may be downloaded from http://rtweb.aer.com. Although the model was initially developed for use in the microwave region, MonoRTM versions numbered v4.0 may also be used at any frequency from microwave to ultraviolet. It is particularly useful in the MW spectral region. It is also applicable for atmospheric laser propagation studies. MonoRTM utilizes the same physics and continuum model as Line-By-Line Radiative Transfer Model (LBLRTM) which is an atmospheric ray tracing program. MonoRTM is suitable for the calculation of radiance associated with atmospheric absorption by molecules in all spectral regions and cloud liquid water in the microwave region. MonoRTM is a forward model, which is composed of three modules as shown in Fig. 4.2: (1) MODM (Monochromatic Optical Depth Model) module for the optical depth computation; (2) LBLRTM module for generating the internal inputs; (3) RADTRA (radiative transfer model) module for simulating the radiance/brightness temperature. The flowchart of the MonoRTM is shown in Fig. 4.2, the inputs of MonoRTM are frequency, atmosphere profile, observer height, LST, zenith angle and atmosphere profile, the output is brightness temperature which is calculated by Eq. (4.5).

$$T_{Bp-TOA} = T_{au} + t \times \left[\varepsilon_p T_s + r_p \left(T_{ad} + t \times T_{sp} \right) \right] \tag{4.5}$$

where

$T_{Bp\text{-}TOA}$ is the brightness temperature at TOA;

T_{au} is the upwelling atmospheric equivalent temperature;

T_{ad} is the downwelling atmospheric equivalent temperature;

t is the atmospheric transmittance;

ε_p is the surface emissivity;

r_p is the surface reflectivity;

T_{sp} is the equivalent temperature of space, T_{sp} = 2.7K.

MonoRTM prescribes six standard model atmospheres: Tropical, Mid-Latitude Summer, Mid-Latitude Winter, Sub-Arctic Summer, Sub-Arctic Winter and 1976 U.S. Standard. The model atmosphere defines a multi-layer atmosphere and contains the following data for each layer: altitude, pressure, temperature, layer column amount of molecular.

4.1.3 Soil-atmosphere radiative transfer model (SARTM)

Soil-atmosphere radiative transfer model (SARTM) is built from MonoRTM and AIEM as shown in Fig. 4.3. It includes three modules. Module 1 is used to read atmospheric parameters and land surface parameters; module 2 is used to calculate the atmospheric cross-section data and simulate surface emissivity; module 3 is used to complete the radiative transfer computation to get the zenith observations of MW brightness temperature. In this model, LSE is obtained from AIEM, soil dielectric constant is obtained from Dobson model, atmospheric spectral line parameters are based on HITRAN 2004 with a few selected exceptions, namely, the parameters for the oxygen lines and for the four strong water vapor absorption and line coupling coefficients are from Tretyakov et al. (2005) and have been validated using ground-based radiometers by Cadeddu et al. (2007). The line strengths for the 22- and 183-GHz water vapor lines are based on an analysis of the Stark-effect measurements described in Clough (2005). The air-broadened half width for the 22-GHz water vapor line is from Payne (2008), while the half widths of the 183- and 325-GHz lines are from a calculation by Gamache (Payne et al., 2008). The self-broadened half width of the 325-GHz line is from Koshelev (2007). The temperature dependences of the half widths and the pressure shifts for these four water lines are from Gamache's calculations.

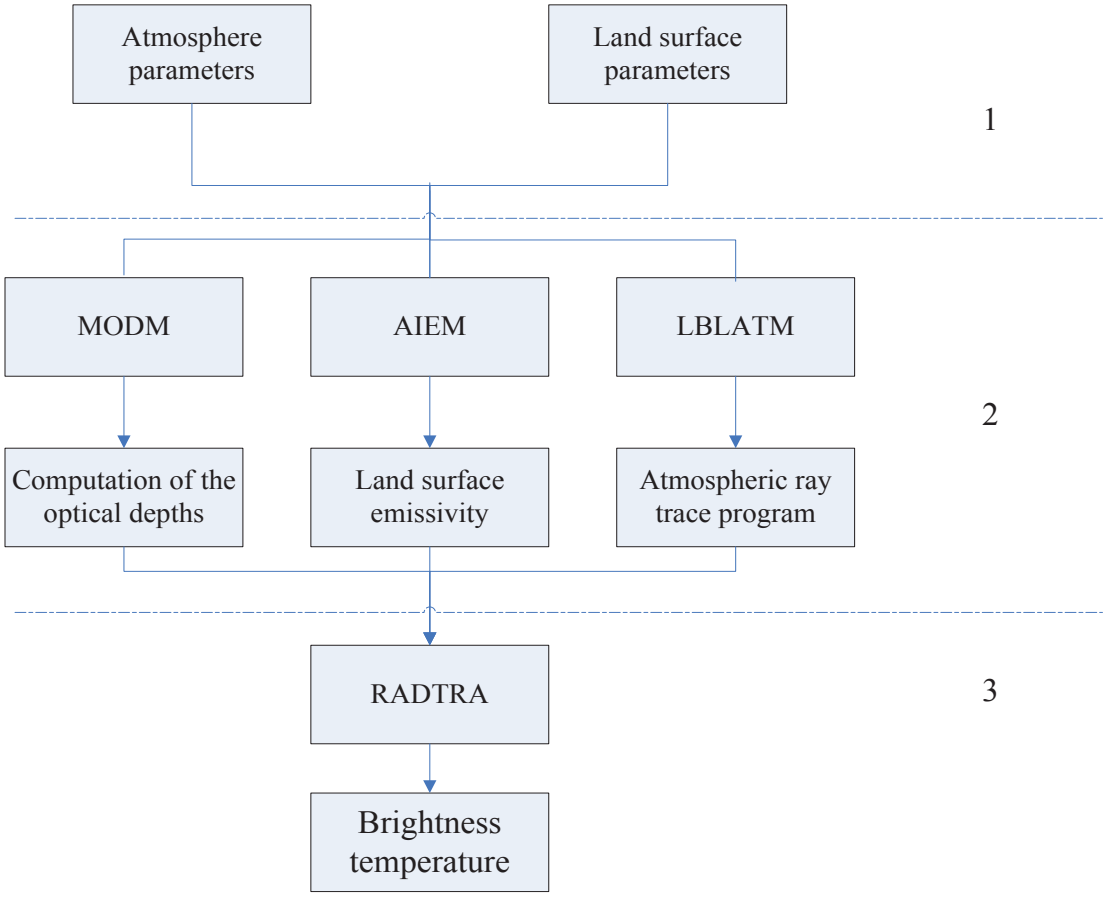

Figure 4.3 Land surface-atmosphere radiative transfer model, module 1 is used to read atmospheric parameters and land surface parameters; module 2 is used to calculate the atmospheric cross-section data and simulate surface emissivity; module 3 is used to complete the radiative transfer computation to get the zenith observations of microwave brightness temperature

SARTM is composed by two parts, one is AIEM to simulate the land surface emissivity and another is MonoRTM to calculate atmospheric transmittance and radiance (brightness temperature) for microwave frequencies. The radiances in MW frequencies are extracted or calculated using FORTRAN programs, and the model is written by FORTRAN language. Fig. 4.4 shows the flowchart of SARTM. Inputs of SARTM include frequency, incidence angle, soil moisture, LST, volumetric contents of sand, volumetric contents of clay, volumetric contents of solid, surface correlation length, root mean square height, atmosphere profile, observer height and zenith angle. The brightness temperatures at TOA are got by SARTM.

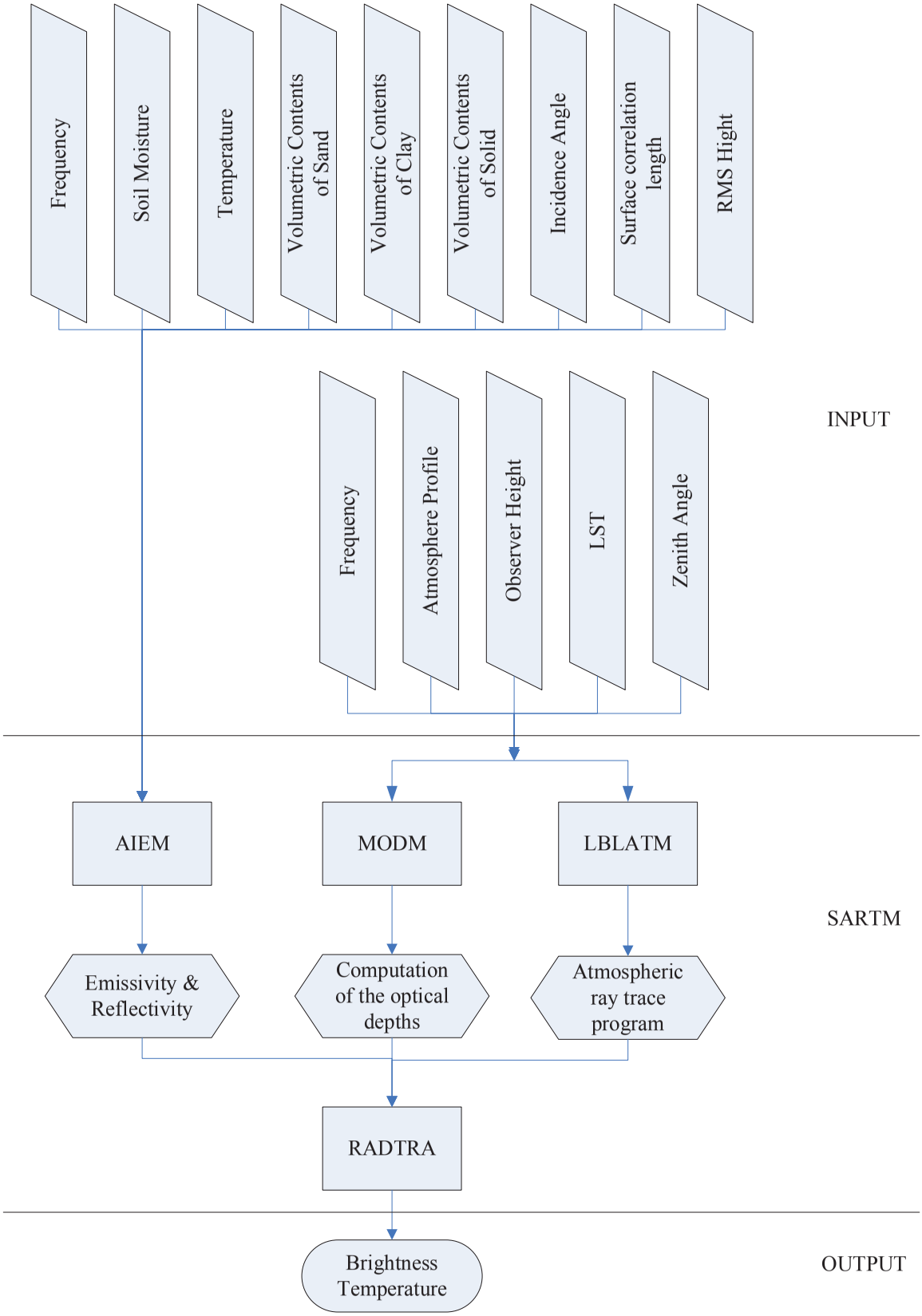

Figure 4.4 Simulation of brightness temperature at sensor

4.2 LSE retrieval

This section is devoted to (1) developing an empirical relationship between the vertical and horizontal polarization soil MW emissions and (2) developing a method to retrieve LSE from AMSR-E data, provided that the LST is known or can be estimated in other ways.

4.2.1 Relationship of LSE

As an example, Fig. 4.5 shows the atmospheric transmittance calculated by our SARTM in function of frequency for the U.S. standard 1976 model atmospheric profile. It shows that the percentage of transmittance through the U.S. standard 1976 model atmospheric profile under clear sky conditions in microwave region increase with the increase of wavelength.

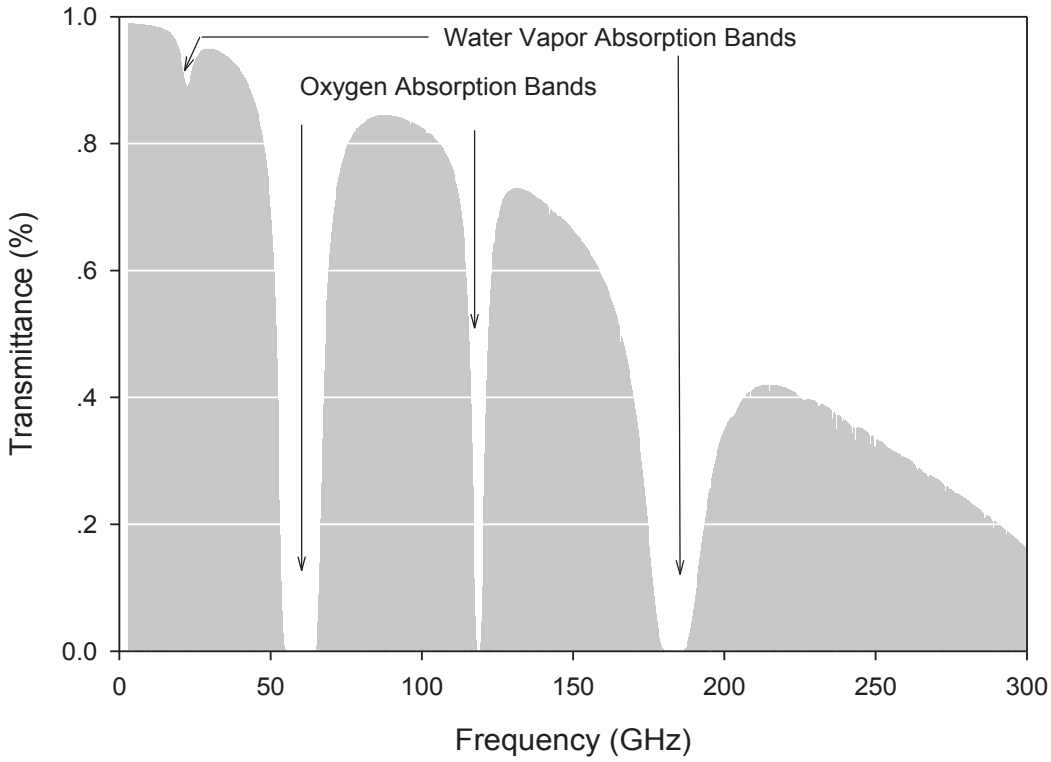

Figure 4.5 Percentage transmission through the U.S. standard 1976 model atmospheric profile, under clear sky conditions

Although MW has a strong penetrating ability to penetrate clouds and rain, the atmosphere is not completely transparent. There are still scattering, absorption and emission behaviour of atmospheric in the microwave region. As shown in the Fig. 4.5, in the low frequency region (6.925 GHz and 10.5 GHz), the atmosphere is practically transparent even in the presence of clouds and moderate rainfall rates.

The super-high-frequency (SHF) range from 3 to 30 GHz is used for most of the remote-sensing radar systems, but bas many other applications as well. The remote-sensing radars are concentrated in the region between 9 GHz and 10 GHz and around 14 to 16 GHz. Satellite communications use bands near 4 GHz and 6 GHz and between 11 GHz and 13GHz as well as some higher frequencies. Point-to-point radio communications and various kinds of ground-based radar and ship radar are scattered throughout the range, as are aircraft navigation systems. Because of water-vapor absorption near 22 GHz (see Fig. 4.5), that part of the SHF region near 22 GHz is used almost exclusively for radiometric observations of the atmosphere. Additionally, remote sensing radiometers operate at several points within the SHF range, primarily within the radio-astronomy allocations centred at 4.995 GHz, 10.69 GHz, 15.375 GHz and 19.35GHz (Ulaby et al., 1981).

Most of the extremely-high-frequency (EHF) range from 30 to 300 GHz is used less extensively, although the atmospheric-window region between 30 GHz and 40 GHz (Fig. 4.5) is rather widely used and applications in the neighbourhood of 90 to 100GHz are increasing. Because of the strong oxygen absorption in the neighbourhood of 60 GHz (Fig. 4.5), frequencies in the 40-70 GHz region are not used by active systems. However, multi frequency radiometers operating in the 50-60 GHz range are used for retrieving the atmospheric temperature profiles from radiometric observations. Radars are operated for remote sensing in the 32-36 GHz region, and some military imaging radars are around 95 GHz. Radio-astronomy bands exist at 31.4 GHz, 37 GHz, and 89GHz, and these are, of course, used by microwave radiometers for remote sensing as well (Ulaby et al., 1981).

In the 1- 15 GHz region, the atmosphere is practically transparent even in the presence of clouds and moderate rainfall rates; absorption (and therefore emission) resonances due to water vapour (at 22.2 and 183.3 GHz) and oxygen (in the 50-70 GHz region and at 118.7 GHz) can be used to determine the height profiles of atmospheric water vapour and temperature through radiometric measurements at and near the absorption maxima.

To develop parameterized relationships between emissivity at different frequencies, an emission database for bare surfaces was simulated for the configuration of AMSR-E, i.e., 6.925, 10.65, 18.7, 23.8, 36.5 and 89 GHz at vertical and horizontal polarization with a 55° incident angle as shown in Fig. 4.6. There are 2904 cases in each plots of Fig. 4.6. The soil surface dielectric constants are described by volumetric soil moisture (*sm*), which is varied from 2% to 44% at 2% intervals by Dobson's dielectric mixing model (Dobson et al., 1985),

for a given soil texture. The applicability of the AIEM has proven by comparing the simulation of AIEM with simulated data of a three-dimensional Monte Carlo model and field data (Chen et al., 2003; Chen et al., 2010; Shi et al., 2005). The results show that the AIEM is capable of simulating natural surface soil emissions. The surface roughness parameters, which are also necessary input parameters of AIEM, are set with a root-mean-square height (*s*) from 0.25 to 3.0 cm at a 0.25 cm interval and a correlation length (*cl*) from 5 to 30 cm at a 2.5 cm interval. A ratio of *s* to *cl* (*s/cl*) that is positively correlated with surface roughness condition is used to describe the surface roughness in the following analysis.

Based on the simulated database, the effect of soil moisture and surface roughness on the bare surface emission and the relationship between vertical (ε_v) and horizontal polarization (ε_h) emissivity were analyzed. The resulting scatter plots of the vertical and horizontal polarization emissivities at different frequencies are shown in Fig. 4.7.

There are two clear trends. From points A to B, the value of *s/cl* changes from 0.055 to 0.333, while the volumetric soil moisture remains unchanged at 2%. From B to C, the volumetric soil moisture increases to 44%, while the value of *s/cl* is unchanged. From C to D, the value of *s/cl* decreases from 0.333 to 0.055, while the volumetric soil moisture is constant at 44%. For a given soil moisture condition and in the direction of varying surface roughness, the vertical and horizontal polarization emissivities are negatively correlated, and their relationship is almost linear. The slope and intercept of the linear function may depend on the soil moisture condition. For a given surface roughness and in the direction of varying soil moisture, the vertical and horizontal polarization emissivities are positively correlated, and their relationship is weakly nonlinear over the full range of emissivities for a given surface roughness condition. The slope and intercept are thought to be a function of *s/cl.*

Fig. 4.8 (a,b) displays the upwelling and downwelling atmospheric brightness temperature (T_{au} and T_{ad} computed by our SARTM versus the channels of AMSR-E for six standard atmospheres.

Fig. 4.9 depicts the brightness temperatures at TOA simulated by our SARTM for AMSR-E channels at horizontal and vertical polarizations through the U.S. standard 1976 model atmospheric profile. The *sm* is varied from 2% to 44% at 2% intervals at certain $s = 3$ cm and $cl = 30$ cm.

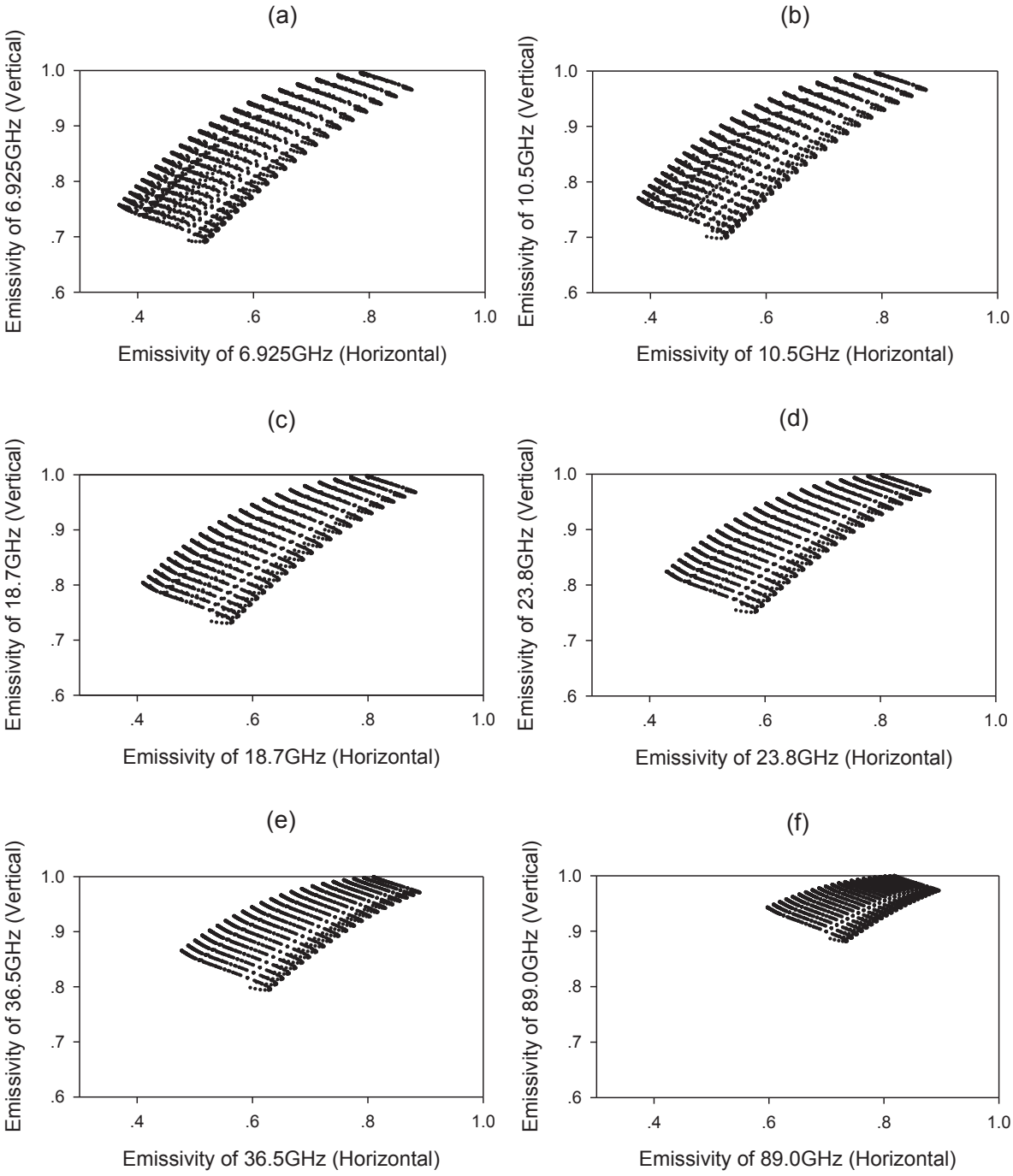

Figure 4.6 Relationships between vertical and horizontal polarized emissivities at each frequency (6.925GHz, 10.5GHz, 18.7GHz, 23.8GHz, 36.5GHz and 89.0GHz)

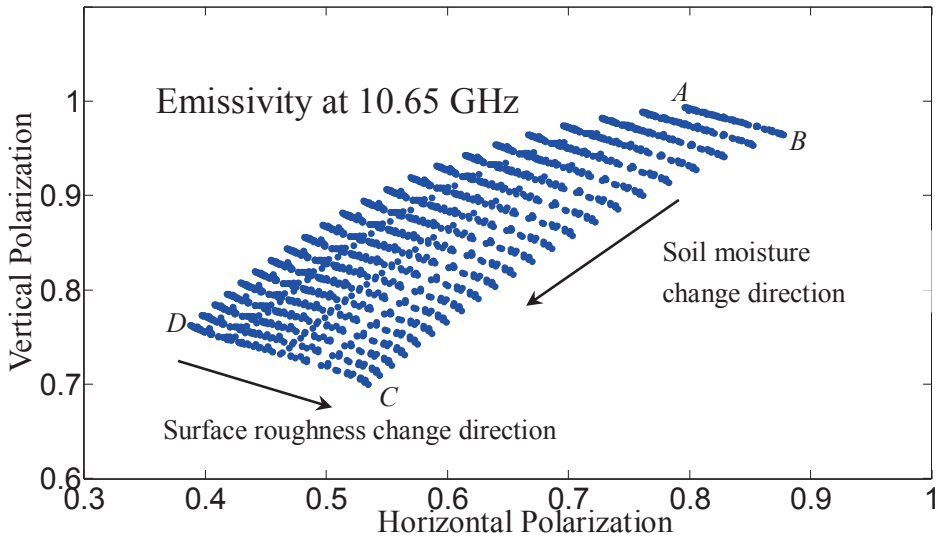

Figure 4.7 Relationship between vertical and horizontal polarization emissivities at 10.65 GHz

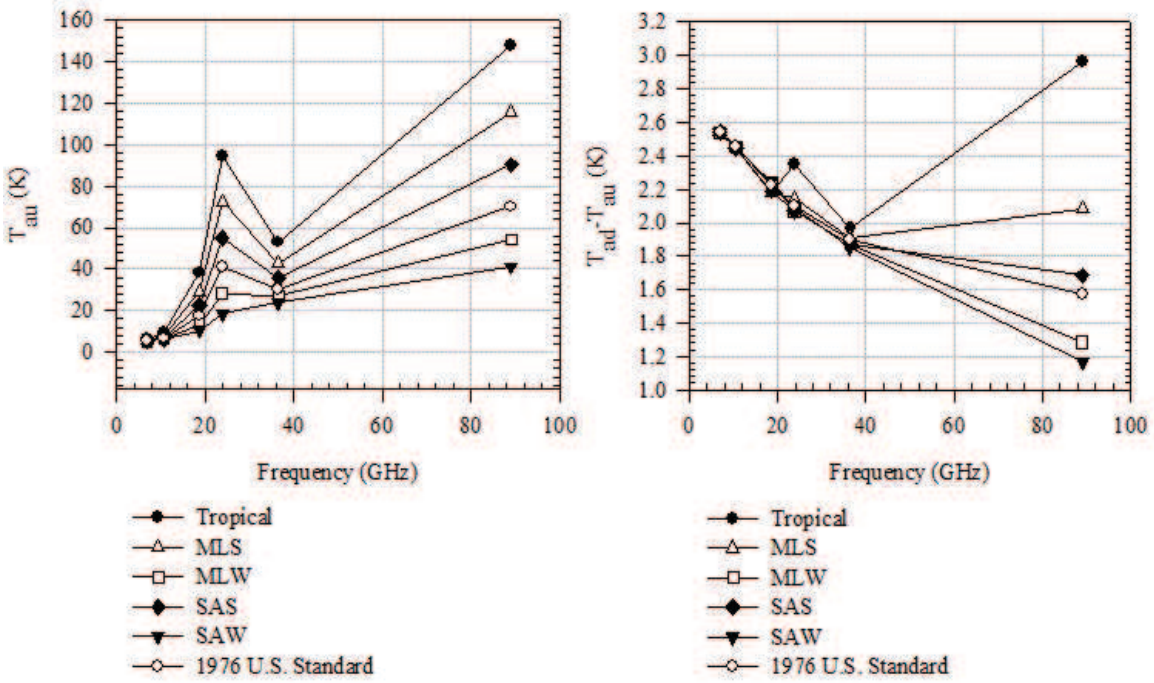

Figure 4.8 The atmospheric upwelling radiation (T_{au}) and the difference of upwelling and downwelling radiation (T_{ad}-T_{au}) for six frequencies (6.925GHz, 10.5GHz, 18.7GHz, 23.8GHz, 36.5GHz and 89.0GHz)

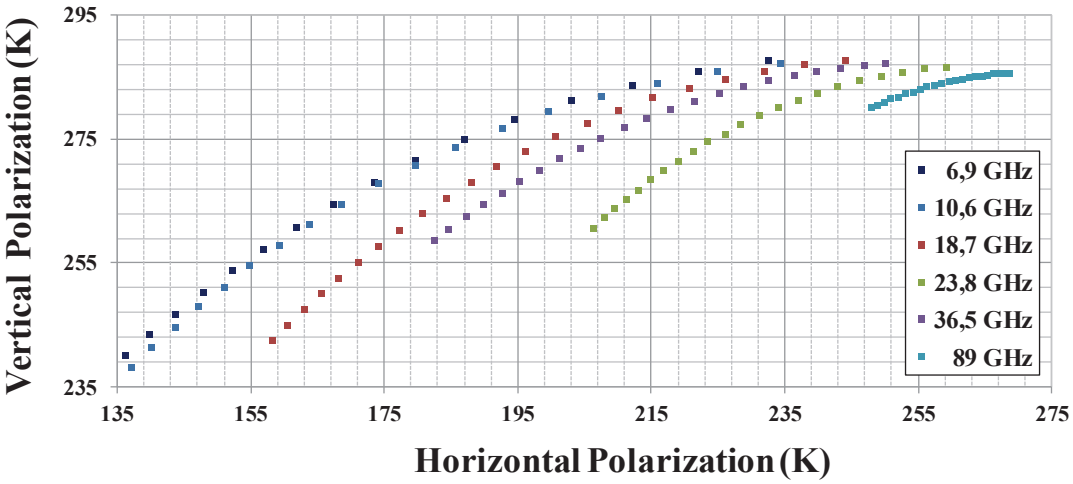

Figure 4.9 Relationship between two polarized brightness temperatures at 6 frequencies simulated by SARTM through the U.S. standard 1976 model atmospheric profile (*sm* = 2% to 44% at step 2%, *s* = 3 cm and *cl* = 30 cm)

Fig. 4.10 illustrates the relationship between vertical and horizontal polarized at-satellite brightness temperature at 36.5 GHz frequency obtained using SARTM model for the 30th June in 2006 at UTC time 0600. The DEM and atmospheric profile used the location longitude 84°and latitude 38° where is sandy desert in China.

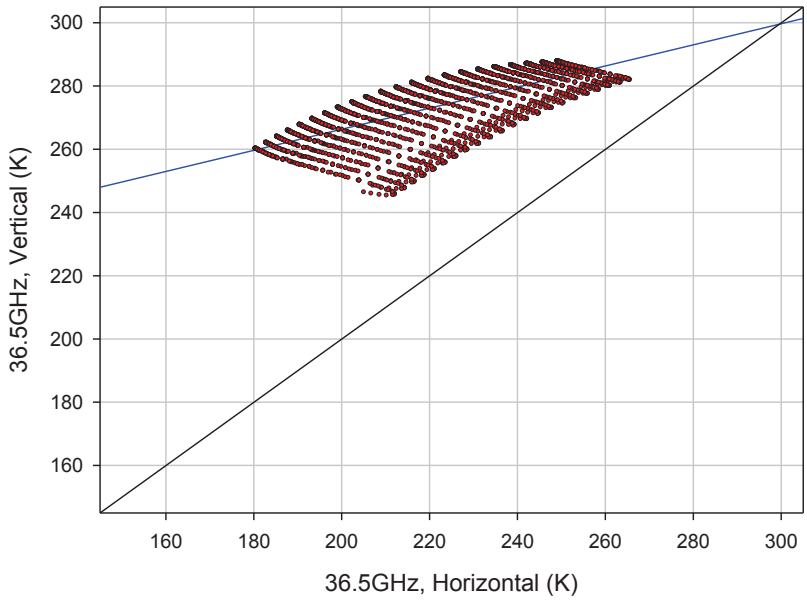

Figure 4.10 Relationship between simulated vertical and horizontal polarized brightness temperature from SARTM Model at 36.5GHz frequency for the 30th June in 2006 at UTC time 0600, the location longitude 84°and latitude 38° where is sandy desert in China

Considering the different effects of soil moisture and surface roughness on emissivity, two empirical parameterized models are developed to characterize the relationship between ε_v and ε_h. The relationship between ε_h and sm is also analyzed.

(1) Parameterized relationship between ε_h and ε_v using sm: As shown in Fig. 4.7, a linear function can be established between $\boldsymbol{\varepsilon}_v$ and $\boldsymbol{\varepsilon}_h$ in the direction of varying surface roughness for a given soil moisture. The coefficients of the function may vary with the relative volumetric soil moisture. Therefore, the slopes and intercepts of a group of sub-parallel lines are dependent on the volumetric soil moisture for a certain frequency, i.e.,

$$\varepsilon_v = A(sm) \times \varepsilon_h + B(sm) \quad (4.6)$$

Fig. 4.11 shows A and B versus sm, which can be expressed by quadratic functions of sm. A comparison between the simulated and estimated ε_v is shown in Fig. 4.12. The estimated $\boldsymbol{\varepsilon}_v$ from Eq. (4.6) shows that the absolute root-mean-square errors (RMSEs) are usually below 0.003, which is sufficient for the applications.

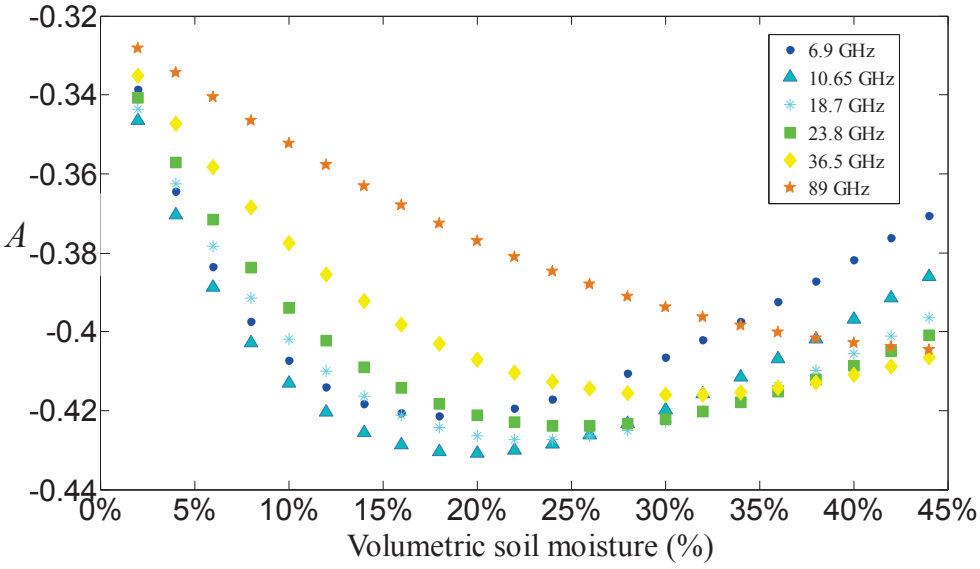

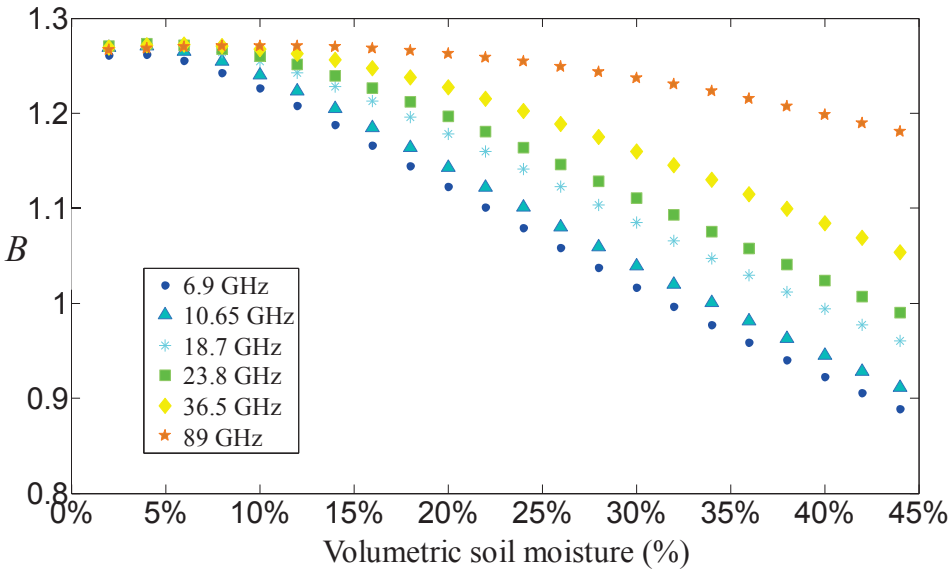

Figure 4.11 Coefficients *A* and *B* versus the volumetric soil moisture

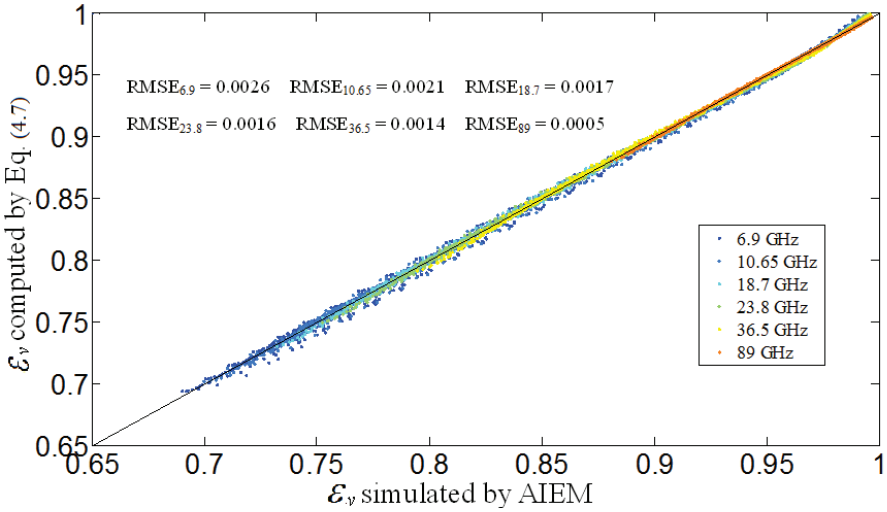

Figure 4.12 Comparison between the vertical polarization AIEM simulated soil surface emissivity and the corresponding emissivity estimated by Eq. (4.6)

Fig. 4.11 shows that the range of A is smaller than the range of B. After further analysis, a simpler form of the relationship is developed, which may be more convenient for application. In this simpler relationship, the coefficient A is constant and B is a quadratic function of sm. Then, Eq. (4.6) can be rewritten as:

$$\varepsilon_v = C \times \varepsilon_h + p_1 \times sm^2 + p_2 \times sm + p_3 \tag{4.7}$$

where C, p_1, p_2 and p_3 are frequency-dependent. Table 4.1 gives the regression coefficients determined using the simulated data. The AIEM simulated soil ε_v and corresponding values calculated using Eq. (4.7) is shown in Fig. 4.13.

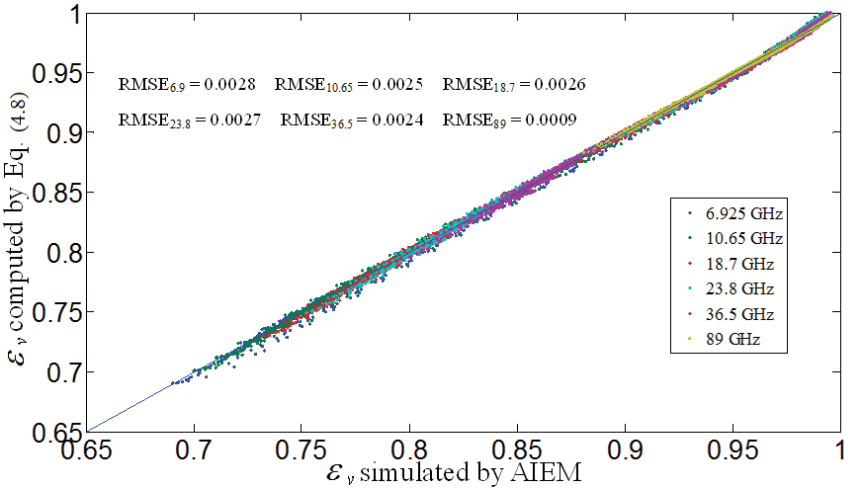

Figure 4.13 Comparison between the vertical polarization AIEM simulated soil surface emissivity and the corresponding emissivity calculated using Eq. (4.7)

Table 4.1 Coefficients in equation Eq. (4.7) for all frequencies of AMSR-E sensor

Coefficients / Frequency(GHz)	C	p_1	p_2	p_3	$RMSE$
6.925	-0.416	0.648	-1.300	1.354	0.0028
10.65	-0.414	0.505	-1.204	1.354	0.0025
18.7	-0.413	0.152	-0.951	1.353	0.0026
23.8	-0.410	-0.035	-0.801	1.350	0.0027
36.5	-0.401	-0.319	-0.525	1.339	0.0024
89	-0.384	-0.386	-0.176	1.318	0.0009

(2) Parameterized relationship between ε_h and ε_v using *s/cl*: The direction in which the soil moisture varies is also important. Although the relationship between the vertical and horizontal polarization emissivities is weakly nonlinear for a varying soil moisture within the full range of emissivities, a linear relationship can also be established under certain conditions. Using the emissivity at 10.65 GHz as an example, this linear relationship can be written as:

$$\varepsilon_v = E(s/cl)\times\varepsilon_h + F(s/cl)\,, \tag{4.8}$$

where the E and F are linear functions of *s/cl*. The RMSE of the estimated ε_v at 10.65 GHz using Eq. (4.8) is 0.0037. Therefore, *s/cl* can be estimated by inverting the linear function with respect to E and F at 10.65 GHz. Fig. 4.14 shows compares between the estimated and actual *s/cl*.

$$s/cl = -1.193\times E - 1.780\times F + 1.796\,,\ RMSE_{10.65}= 0.0082 \text{ and } r^2=0.99, \tag{4.9}$$

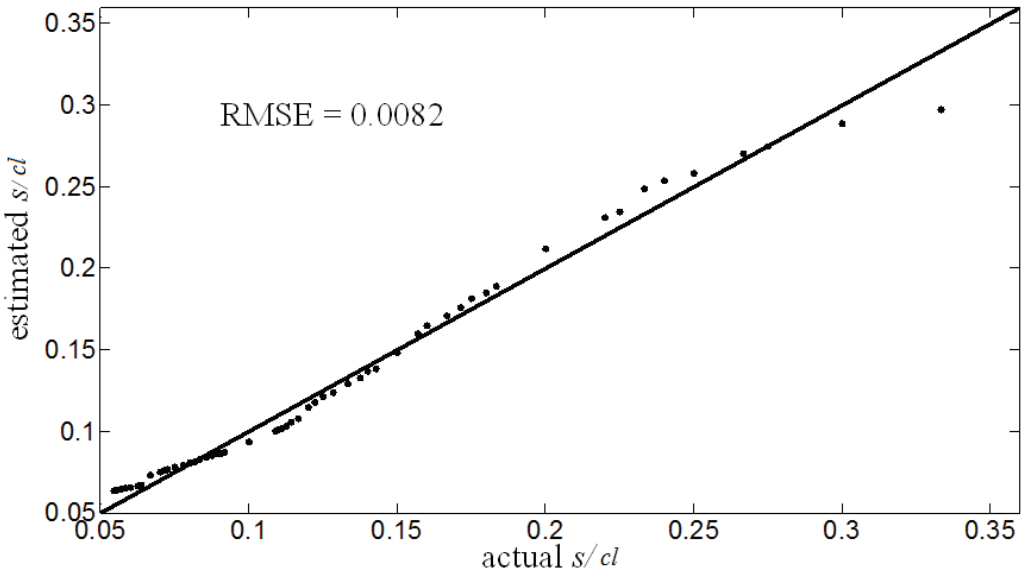

Figure 4.14 Comparison of the estimated and actual *s/cl*

(3) Evaluation and application of the relationships using actual AMSR-E data: Neglecting atmospheric effects, the land surface vertical and horizontal polarization emissivities at 10.65 GHz were computed using the brightness temperature data of AMSR-E and the LST data of the Moderate Resolution Imaging Spectroradiometer (MODIS) as:

$$\varepsilon_p = \frac{T_{Bp}}{T_s}, \tag{4.10}$$

where

ε_p is the land surface emissivity at polarization p;

T_{Bp} is the brightness temperature of AMSR-E;

T_s is the LST from MODIS data.

Considering the low resolution of microwave data, a study area in Saharan Africa, as indicated by the red rectangle in Fig. 4.15, is considered. The vertical and horizontal polarization microwave emissivities at 10.65 GHz in 2004 are computed for this study area using Eq. (4.10).

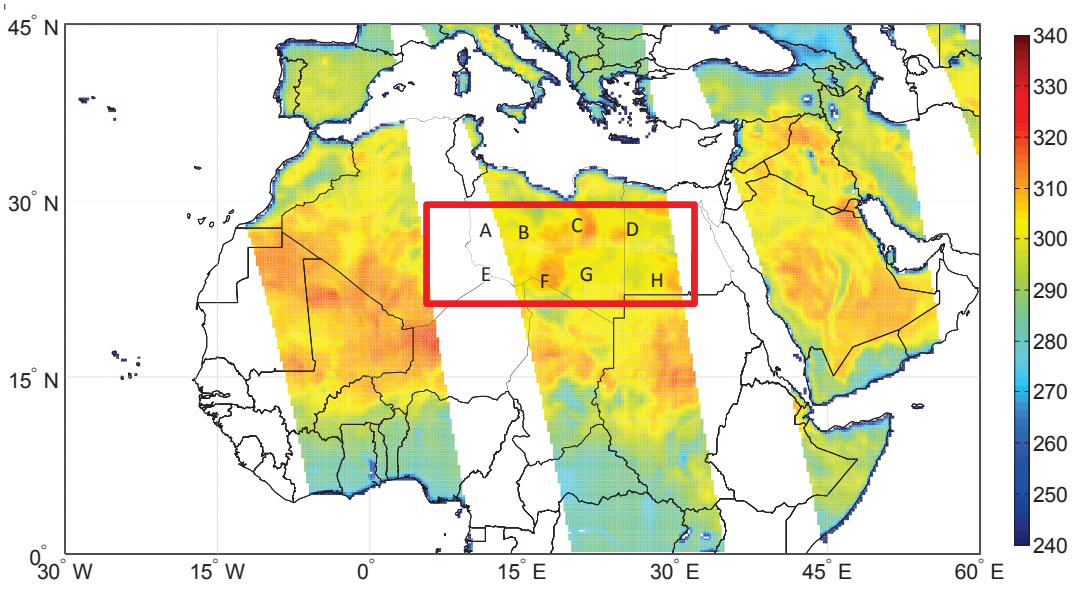

Figure 4.15 Land surface brightness temperature at 10.65 GHz vertical polarization for one day June 2th in 2004. The study area is bounded by the red rectangle and the locations of the eight evaluation sites are labeled from A to H

The computed emissivities are plotted with the simulated data in Fig. 4.16.

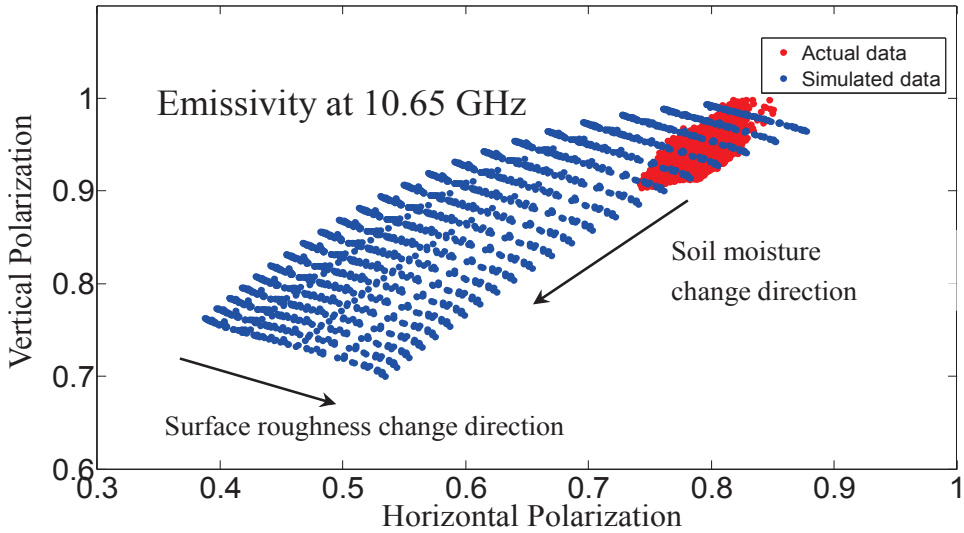

Figure 4.16 Vertical and horizontal polarization emissivities at frequency 10.65 GHz; red: actual data; blue: simulated data

The emissivities are discretely distributed due to the coupling between the effects of surface roughness and soil moisture in the study area. Because the surface roughness is less variable than soil moisture at a given place for a period, the emissivities may be described by an approximate linear relationship, as in Eq. (4.8). To further illustrate these phenomena, eight sites with predominantly bare soils are chosen and labelled A through H. The computed emissivities for these points for all clear days in 2004 are shown in Fig. 4.17. There are clear linear relationships between the vertical and horizontal polarization emissivities, which agree well with the analysis above. The regression lines and value of *s/cl* estimated by Eq. (4.9) are also shown in Fig. 4.17.

The estimated values of *s/cl* are largely consistent in between the eight sites. However, the absolute values of the estimated *s/cl* are near the maximum used in the simulated data, which is inconsistent with the fact that the surface should be relatively smooth in the study area. The difference between the simulated and actual data may contribute to the discrepancy between the scale of modelling and that of observation (Wu and Li, 2009).

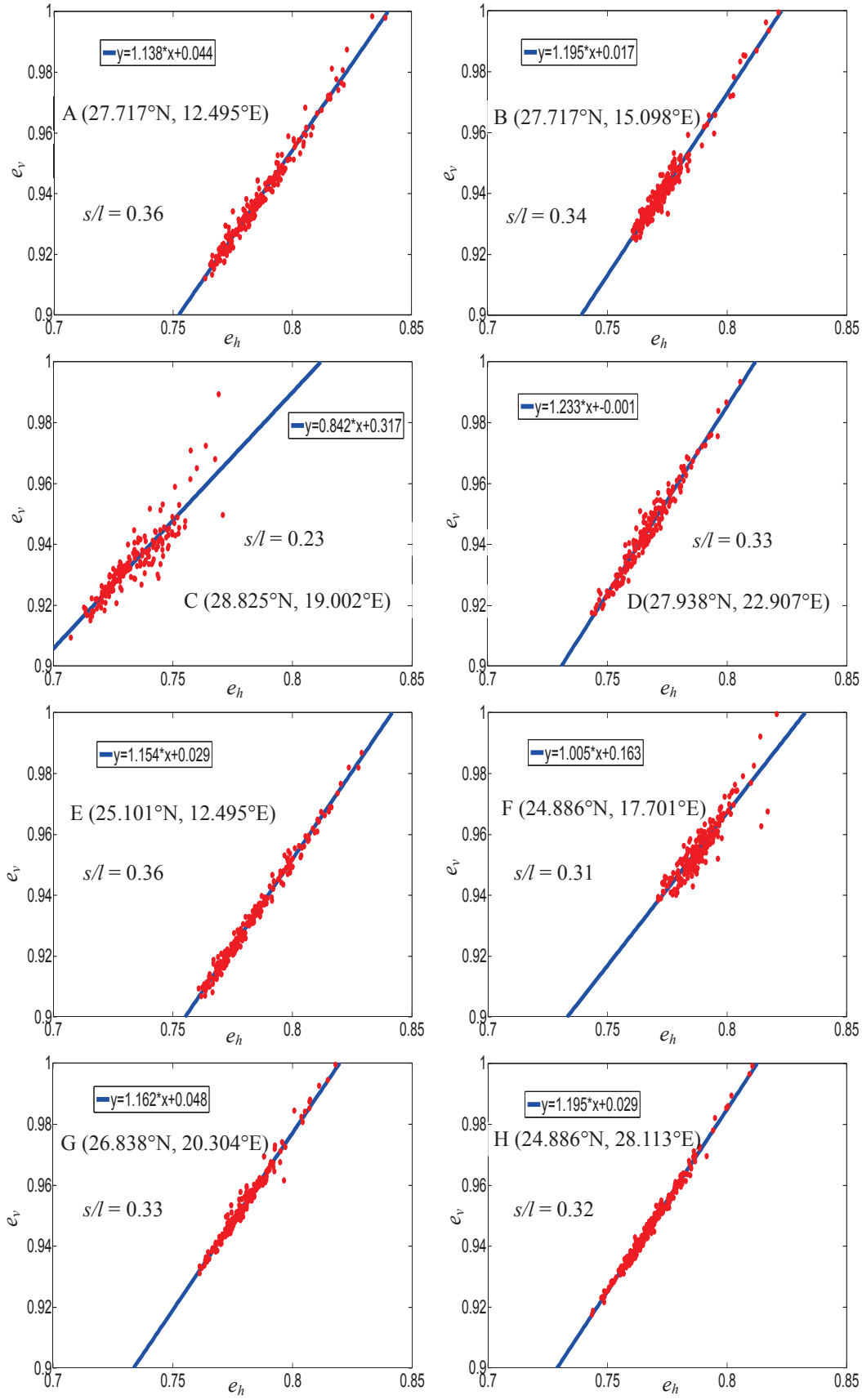

Figure 4.17 Scatter plots of vertical and horizontal polarization emissivities for the eight sites in the Sahara Desert

4.2.2 LSE retrieval from AMSR-E data in combination with MODIS LST

In the AMSR-E microwave frequencies range, for a given path zenith angle, the brightness temperature ($T_{B,f,p}$) observed by the satellite instrument can be expressed by Eq. (2.25). Provided that LST (T_s) is known and the atmospheric quantities (t_f, $T_{au,f}$, $T_{ad,f}$) are estimated using MonoRTM with atmospheric profiles, LSE ($\varepsilon_{f,p}$) can be directly derived from

$$\varepsilon_{f,p} = \frac{T_{B,f,p} - T_{au,f} - T_{ad,f} \times t_f - T_{sp} \times t_f^2}{\left(T_s - T_{ad,f} - T_{sp} \times t_f\right) \times t_f}, \tag{4.11}$$

where subscripts p and f represent polarization (vertical or horizontal) and frequency, respectively. T_{sp} is the equivalent temperature of space, $T_{sp} = 2.7K$.

In this study, to retrieve LSE from $T_{B,f,p}$, LST (T_s) at AMSR-E pixel is calculated from MODIS LST product using Eq. (4.11), and the atmospheric profiles given by ECMWF data are used to estimate the atmospheric quantities (t_f, $T_{au,f}$, $T_{ad,f}$) with MonoRTM.

As an example, maps of the monthly mean LSEs in February 2006 over whole China retrieved using this method at 18.7 GHz and 36.5 GHz for vertical and horizontal polarizations are displayed in Fig. 4.18. Note that, each composite LSE value in this figure is the average value of all LSEs available in one month.

To analyze the variation of LSE with different land surface types, eight sites, which represent sandy desert, rocky desert, forest, wetland, grassland and barren/sparsely vegetated surface according to ESA/ESA Glob cover Project classification, are selected. Table 4.2 lists the monthly mean LSEs of February, June and September at two polarizations and mean difference of LSE at two polarizations for 8 sites (Taklimakan, Junggar, Donggebi, Linzhi, Nameless, Zhalong, Tianshan, Zhongcang). From this table, one can notice that the polarization difference of LSEs is dependent of land surface type. The vegetated land surfaces have small polarization difference of LSEs and the sandy desert has the largest polarization difference of LSEs. The polarization differences of LSEs at 18.7 GHz are commonly larger than those at 36.5 GHz, especially over the rocky desert and grassland.

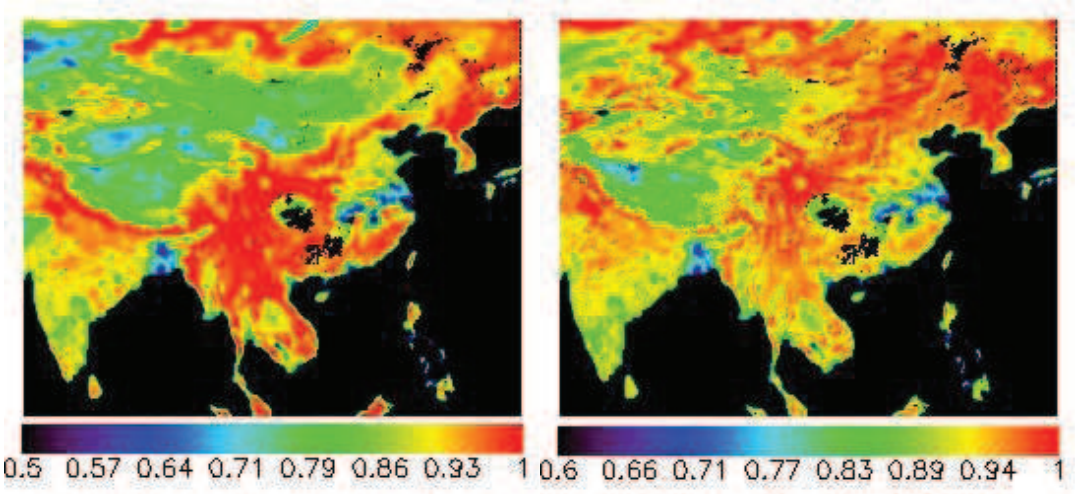

(a) 18 GHz (horizontal) (b) 18 GHz (vertical)

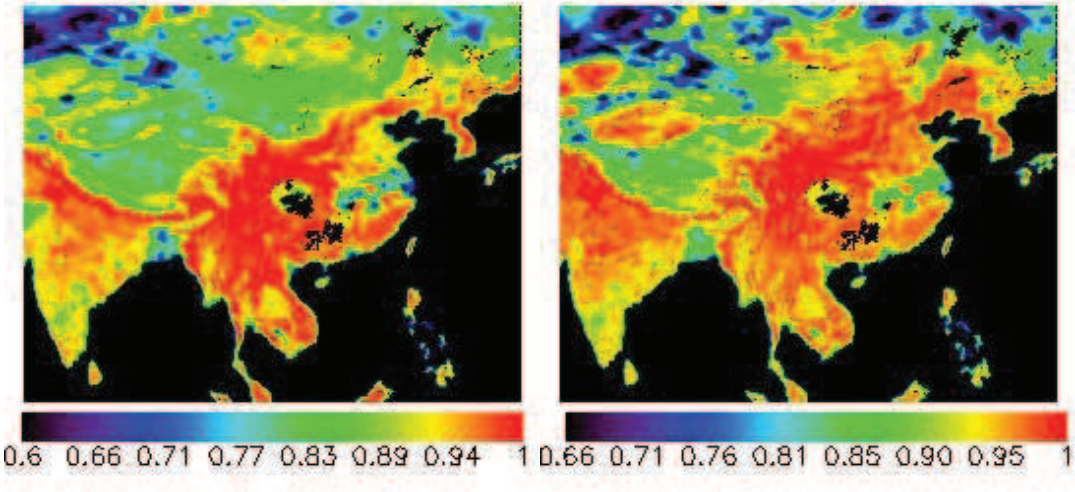

(c) 36 GHz (horizontal) (d) 36 GHz (vertical)

Figure 4.18Composite monthly mean LSE at 18.7 GHz and 36.5 GHz for horizontal and vertical polarizations in February 2006

Table 4.2 Mean emissivity of February, June and September at horizontal (*H*) and vertical (*V*) polarizations and mean difference of LSE at two polarizations ($\Delta\varepsilon = \varepsilon_V - \varepsilon_H$) over 8 sites in 2006

Site name	Location	Land cover type	$\varepsilon_{18.7}$ (Feb.)		$\varepsilon_{36.5}$ (Feb.)		$\varepsilon_{18.7}$ (Jun.)		$\varepsilon_{36.5}$ (Jun.)		$\varepsilon_{18.7}$ (Sept.)		$\varepsilon_{36.5}$ (Sept.)	
			V	H	V	H	V	H	V	H	V	H	V	H
Taklimakan	N38°, E83°	Sandy desert	0.93	0.78	0.93	0.79	0.95	0.79	0.95	0.80	0.93	0.77	0.94	0.78
			$\Delta\varepsilon = 0.15$		$\Delta\varepsilon = 0.14$		$\Delta\varepsilon = 0.16$		$\Delta\varepsilon = 0.15$		$\Delta\varepsilon = 0.16$		$\Delta\varepsilon = 0.16$	
Junggar	N45°, E87.25°	Rocky desert	0.95	0.83	0.80	0.73	0.93	0.84	0.92	0.86	0.93	0.84	0.93	0.85
			$\Delta\varepsilon = 0.12$		$\Delta\varepsilon = 0.07$		$\Delta\varepsilon = 0.09$		$\Delta\varepsilon = 0.06$		$\Delta\varepsilon = 0.09$		$\Delta\varepsilon = 0.08$	
Donggebi	N44°, E110°	Rocky desert	0.96	0.82	0.94	0.82	0.97	0.83	0.95	0.84	0.96	0.83	0.94	0.85
			$\Delta\varepsilon = 0.14$		$\Delta\varepsilon = 0.12$		$\Delta\varepsilon = 0.14$		$\Delta\varepsilon = 0.11$		$\Delta\varepsilon = 0.13$		$\Delta\varepsilon = 0.09$	
Linzhi	N30°, E93°	Forest	0.95	0.94	0.94	0.93	0.95	0.93	0.95	0.94	0.95	0.94	0.95	0.94
			$\Delta\varepsilon = 0.01$		$\Delta\varepsilon = 0.01$		$\Delta\varepsilon = 0.02$		$\Delta\varepsilon = 0.01$		$\Delta\varepsilon = 0.01$		$\Delta\varepsilon = 0.01$	
Nameless	N42°, E85°	Barren/sparsely vegetated	0.93	0.89	0.91	0.87	0.90	0.85	0.89	0.85	0.90	0.86	0.90	0.86
			$\Delta\varepsilon = 0.04$		$\Delta\varepsilon = 0.04$		$\Delta\varepsilon = 0.05$		$\Delta\varepsilon = 0.04$		$\Delta\varepsilon = 0.04$		$\Delta\varepsilon = 0.04$	
Zhalong	N47°, E124°	Wetland	0.97	0.90	0.92	0.85	0.93	0.84	0.92	0.84	0.91	0.83	0.91	0.84
			$\Delta\varepsilon = 0.07$		$\Delta\varepsilon = 0.07$		$\Delta\varepsilon = 0.09$		$\Delta\varepsilon = 0.08$		$\Delta\varepsilon = 0.08$		$\Delta\varepsilon = 0.07$	
Tianshan	N42.25°, E86°	Grassland	0.94	0.88	0.93	0.88	0.91	0.85	0.90	0.85	0.92	0.87	0.92	0.86
			$\Delta\varepsilon = 0.06$		$\Delta\varepsilon = 0.05$		$\Delta\varepsilon = 0.06$		$\Delta\varepsilon = 0.05$		$\Delta\varepsilon = 0.05$		$\Delta\varepsilon = 0.06$	
Zhongcang	N32°, E85.25°	Grassland	0.91	0.81	0.89	0.81	0.90	0.81	0.88	0.81	0.92	0.82	0.90	0.83
			$\Delta\varepsilon = 0.10$		$\Delta\varepsilon = 0.08$		$\Delta\varepsilon = 0.09$		$\Delta\varepsilon = 0.07$		$\Delta\varepsilon = 0.10$		$\Delta\varepsilon = 0.07$	

As an example, Fig. 4.19 displays the daily LSE retrieved from AMSR-E at Taklimakan site for February, June and September of 2006.

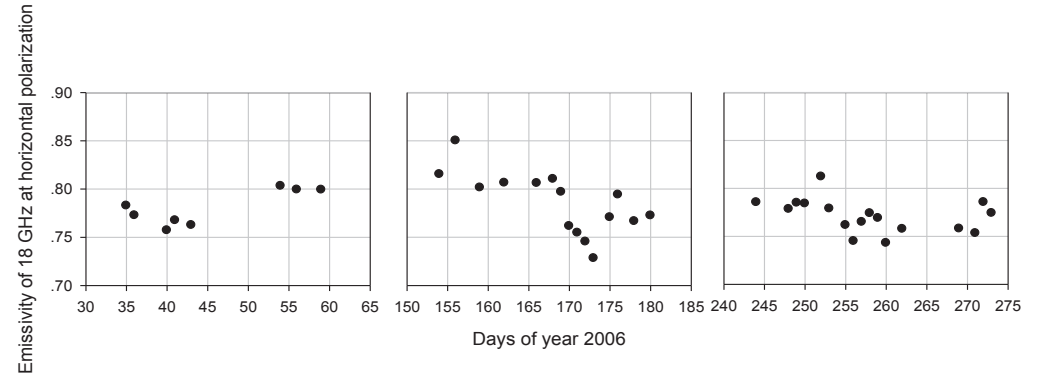

(a)

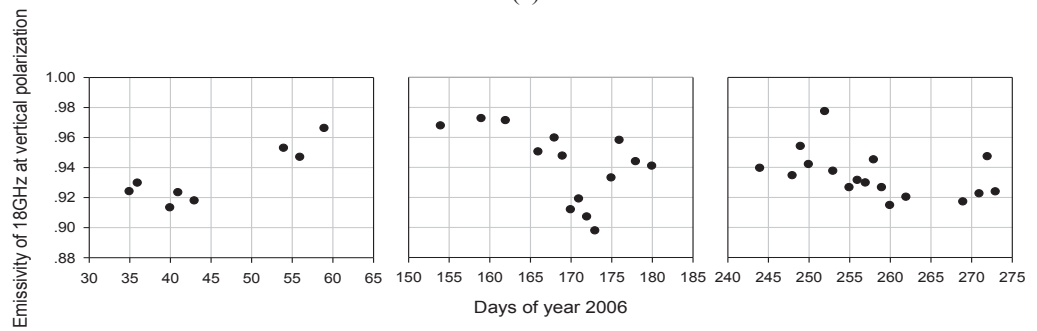

(b)

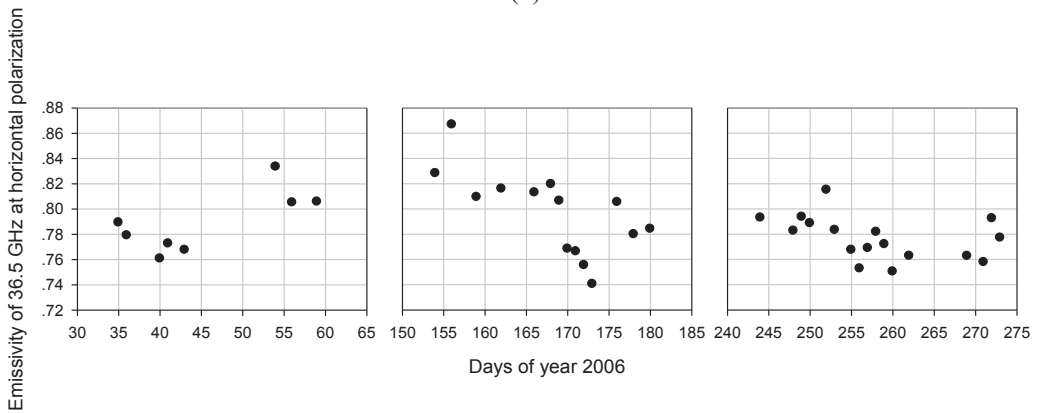

(c)

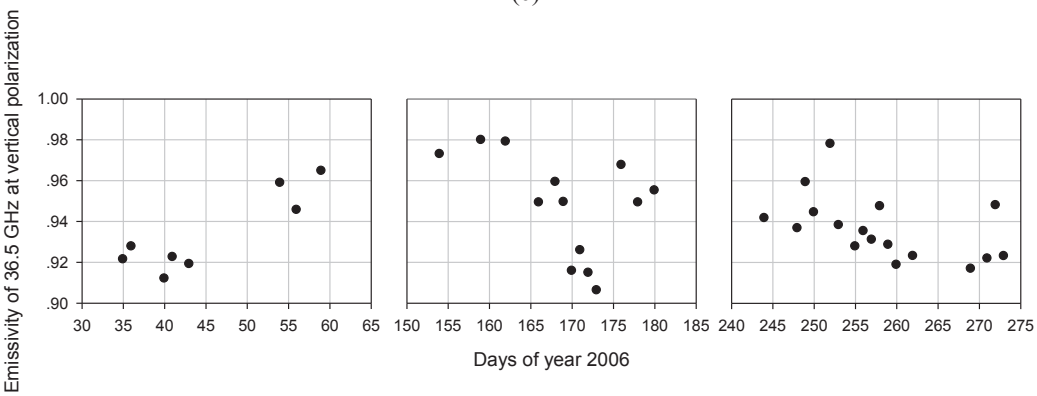

(d)

Figure 4.19 Daily evolution of LSE at Taklimakan site for February, June and September of 2006 at two polarizations

4.3 Atmospheric correction for retrieving LST from AMSR-E data

In this section, a simulated database is first built that covers various atmospheric and land surface conditions and reflects AMSR-E data. Atmospheric effects on AMSR-E observations are then analyzed and an atmospheric correction algorithm at 18.7 GHz vertical polarization is finally proposed.

4.3.1 Database

A simulated database of passive microwave land surface brightness temperatures, configured to represent AMSR-E data, is built using the modified microwave MonoRTM, which is used for analyzing atmospheric effects. To generate simulated database, atmosphere profile data, LSE data and LST data are all required. Descriptions of the data used in this study are partly provided in section 4.2, and partly given below.

LST is necessary input parameter to simulate brightness temperature of land surface. T_o make the value of LST more reasonable, LST was set within a given range based the temperature (T_0) of the bottom layer of atmosphere. Specifically, LST varied from -5 K to 15 K, with an interval of 5 K, for $T_0 \geqslant 280$ K, and from -10 K to 10 K, with an interval of 5 K, for $T_0 < 280$ K.

Using this input data, a simulation database containing 638880 AMSR-E brightness temperature observations and covering a range of atmospheric and land surface conditions were established using the MonoRTM model. All of following analysis work is based on the simulated data.

4.3.2 Analysis of atmospheric effects

To show the effects of atmosphere on AMSE-E observations, the simulated brightness temperature at the top and the bottom of the atmosphere ($T_{Bp\text{-}TOA}$ and $T_{Bp\text{-}BOA}$) has been compared to the land surface emitted brightness temperature ($T_{B,S}$). According to radiative transfer theory, the satellite-observed brightness temperature at polarization mode, p, and a given frequency and incidence angle can be written as:

$$T_{Bp-TOA} = T_{Bp-BOA} \times t + T_{au}, \tag{4.12}$$

where T_{Bp_BOA} is the brightness temperature at polarization, p, (vertical or horizontal) observed at the bottom of atmosphere. It can be expressed as:

$$T_{Bp-BOA} = T_{Bp-land} + \left[T_{ad} + T_{sp} \times t\right] \times (1-\varepsilon_p), \tag{4.13}$$

and $T_{Bp\text{-}land}$ is given by Eq. (2.8).

Fig. 4.20 shows the difference between $T_{Bp\text{-}TOA}$ and $T_{Bp\text{-}BOA}$ at vertical (ΔT_{BV}) and horizontal (ΔT_{BH}) polarization using the simulated data for all of the AMER-E channels. The mean and standard deviation (STD) for the difference between ΔT_{BV} and ΔT_{BH} are given in Table 4.3.

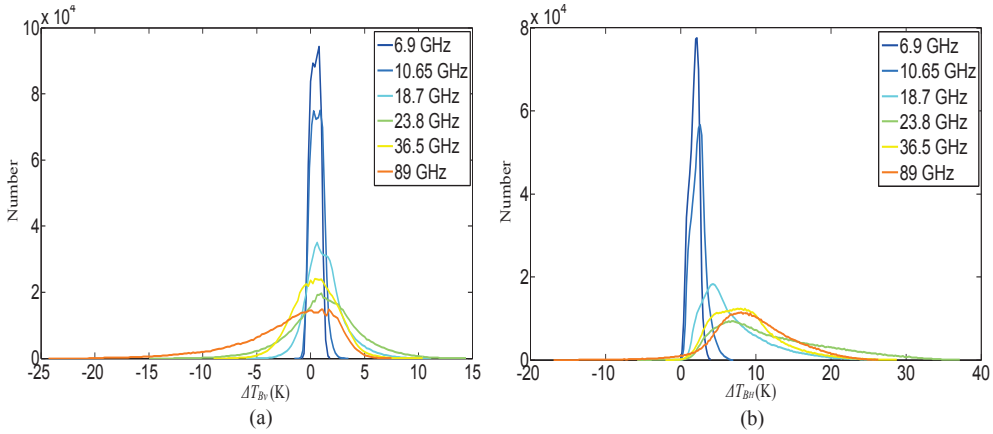

Figure 4.20 Comparison between the $T_{Bp\text{-}TOA}$ and $T_{Bp\text{-}BOA}$ at vertical polarization (a) and horizontal polarization (b)

Table 4.3 Mean and standard deviation (STD) of the T_{BV} and T_{BH} for all channels of AMSR-E

Frequency (GHz)	Vertical Polarization		Horizontal Polarization	
	mean(K)	STD (K)	mean (K)	STD (K)
6.925	0.44	0.44	1.81	0.65
10.65	0.60	0.57	2.40	0.98
18.7	1.33	1.78	6.91	4.22
23.8	1.23	3.27	12.07	7.05
36.5	0.48	2.11	8.71	4.38
89	-1.97	4.28	9.69	4.98

The simulated data set shows that the mean differences are greater than zero, with the exception of ΔT_{B89V}. This means that the atmosphere acts as an emission source rather than an absorption layer in most cases. The STD resulting from a comparison of $T_{Bp\text{-}TOA}$ and $T_{Bp\text{-}BOA}$ is 0.44 K and 0.65 K, respectively, at a frequency of 6.925 GHz for the vertical and horizontal polarizations. This means that the atmospheric effect on observed brightness temperatures at

6.925 GHz can be neglected and the $T_{B6.925p\text{-}TOA}$ can be directly used as $T_{B6.925p\text{-}BOA}$ without introducing significant errors. Furthermore, because the mean value is 0.6 K and the STD is 0.57 K, $T_{B10.65v\text{-}TOA}$ can be used as $T_{B10.65v\text{-}BOA}$ without considering atmospheric effects. For the other channels of AMSR-E, the mean and STD are larger than 1 K, with the exception of the STD at 10.65 GHz with horizontal polarization and the mean at 36.5 GHz with vertical polarization. Atmospheric effects on these channels should be considered.

Fig 4.21 shows the difference between $T_{Bp\text{-}TOA}$ and T_{Bp_land} at vertical ($\Delta T'_{BV}$) and horizontal ($\Delta T'_{BH}$) polarization using simulated data for all of the channels of AMER-E. The mean and STD of the difference between $\Delta T'_{BV}$ and $\Delta T'_{BH}$ are given in Table 4.4.

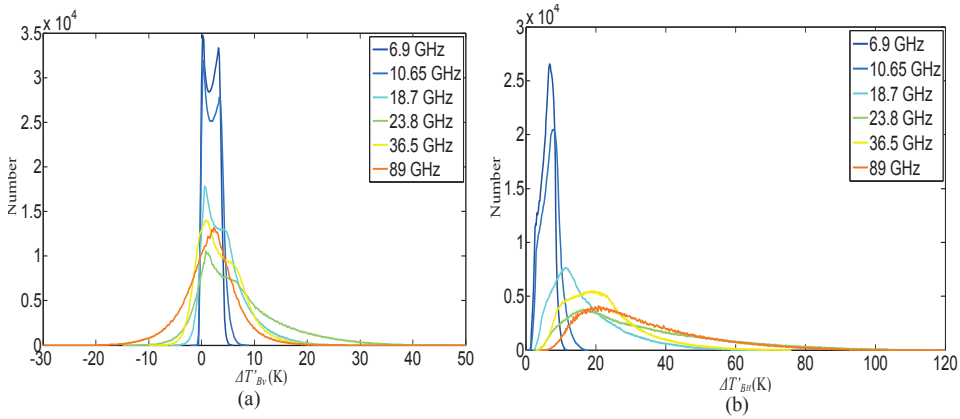

Figure 4.21 Comparison between the T_{Bp_toa} and T_{Bp_land} at vertical polarization (a) and horizontal polarization (b)

Comparing $T_{Bp\text{-}TOA}$ and T_{Bp_land} shows that both the mean and the STD are larger than 1 K in every AMSR-E channel. This means that atmospheric effects should be considered when estimating T_{Bp_land} using AMSR-E data.

Table 4.4 Mean and STD of the T'_{BV} and T'_{BH} for all channels of AMSR-E

Frequency (GHz)	Vertical Polarization		Horizontal Polarization	
	mean (K)	STD(K)	mean (K)	STD (K)
6.925	1.88	1.25	5.99	1.89
10.65	2.16	1.50	7.14	2.52
18.7	4.40	4.13	17.23	9.98
23.8	6.95	7.64	32.62	19.98
36.5	3.70	4.24	22.27	10.74
89	1.71	5.04	32.94	16.71

Further analysis shows that atmospheric effects are less critical to the temperature of the atmosphere than to the atmospheric water content across a range of atmospheric conditions. A comparison of $T_{Bp\text{-}TOA}$ and $T_{Bp\text{-}BOA}$ shows that, when the atmospheric water content is less than 20 kg/m^2, the mean and STD are lower than 1.5 K at 18.7 GHz vertical polarization. At 36.5

GHz vertical polarization, the mean and STD are less than 2 K. At 89 GHz vertical polarization, the mean and STD are lower than 2 K when the atmospheric water content is less than 10 kg/m^2. Due to the low values of land surface emissivity at horizontal polarization, atmospheric effects are more pronounced than at vertical polarization. The results show that atmospheric effects on observed brightness temperatures at horizontal polarization should be considered.

4.3.3. Atmospheric correction algorithm

(1) Algorithm: the results above show that atmospheric correction is necessary for AMSR-E data, with the exception of the 6.925 and 10.65 GHz bands at vertical polarization and 6.925 GHz at horizontal polarization. Using the simulated data, a theoretical description of the required atmospheric correction and a correction algorithm are presented in this section. The approximate equivalency of $\varepsilon_{v18.7}$ and $\varepsilon_{v23.8}$ (Weng and Grody, 1998), as well as the obvious differences between the atmospheric effects at 18.7 and 23.8 GHz vertical polarization, makes it possible to remove the atmospheric effects on observations at 18.7 GHz vertical polarization. Based on the classic split window technique, which is usually used in thermal infrared remote sensing (Becker and Li, 1999), an atmospheric correction method for the 18.7 GHz vertical polarization channel of AMSR-E is established.

First, using the simulated data, the following empirical relationships were established. For observations of AMSR-E under clear sky conditions, T_{au} and T_{ad} are closely related and can be expressed as:

$$T_{ad} = T_{au} + 2.11, \quad R^2 = 0.99. \tag{4.14}$$

Eq. (4.14) demonstrates that it is reasonable to consider Tau and Tad to be approximately equal (Njoku and Li, 1999), especially under relatively moist atmospheric conditions.

Next, some linear relationships between t and w (the atmospheric water content, kg/m2) at 18.7 and 23.8 GHz were also established:

$$t_{18.7} = -0.003 \times w + 0.975, \quad R^2 = 0.99, \tag{4.15}$$

$$t_{23.8} = -0.007 \times w + 0.951, \quad R^2 = 0.99. \tag{4.16}$$

Fig. 4.22 shows a scatter plot of $t_{18.7}$ and $t_{23.8}$ with w.

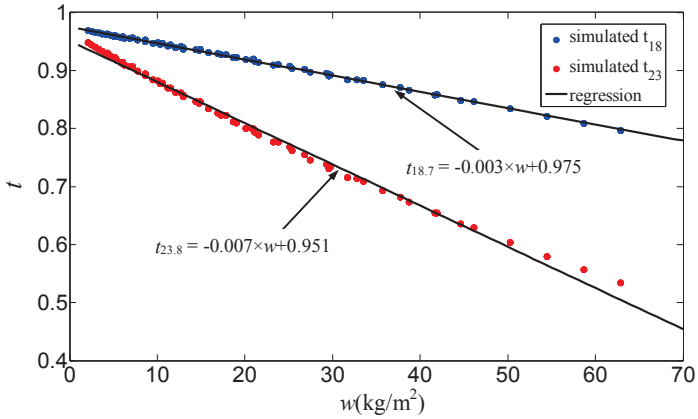

Figure 4.22 Linear relationships between w and t at 18.7 and 23.8 GHz

Using the approximate expression for effective radiating temperature (T_{ae}), T_{au} can be expressed as (Njoku and Li, 1999):

$$T_{au} = T_{ae} \times (1-t) \tag{4.17}$$

Substituting Eqs. (4.14) to (4.17) into Eqs. (4.12) and (4.13) gives:

$$\begin{aligned} T_{B18.7V-TOA} = {} & T_s + (T_{ae} - T_s) \times (1-b_{18.7}) - a_{18.7} \times w \times (T_{ae} - T_s) - 2a_{18.7} \times b_{18.7} \times w \times T_s \\ & + r_{18.7\mathrm{V}} \times a_{18.7} \times w \times (T_{ae} - T_s) \times (1-2b_{18.7}) - a_{18.7}^2 \times w^2 \times r_{18.7\mathrm{V}} \times T_{ae} \\ & + r_{18.7\mathrm{V}} \times b_{18.7} \times (1-b_{18.7}) \times (T_{ae} - T_s)_s - b_{18.7}^2 \times r_{18.7\mathrm{V}} \times T \\ & + 2.11 \times r_{18.7\mathrm{V}} \times (a_{18.7} \times w + b_{18.7}), \end{aligned} \tag{4.18}$$

$$\begin{aligned} T_{B23.8V-TOA} = {} & T_s + (T_{ae} - T_s) \times (1-b_{23.8}) - a_{23.8} \times w \times (T_{ae} - T_s) - 2a_{23.8} \times b_{23.8} \times w \times T_s \\ & + r_{23.8\mathrm{V}} \times a_{23.8} \times w \times (T_{ae} - T_s) \times (1-2b_{23.8}) - a_{23.8}^2 \times w^2 \times r_{23.8\mathrm{V}} \times T_{ae} \\ & + r_{23.8\mathrm{V}} \times b_{23.8} \times (1-b_{23.8}) \times (T_{ae} - T_s) - b_{23.8}^2 \times r_{23.8\mathrm{V}} \times T_s \\ & + 2.11 \times r_{23.8\mathrm{V}} \times (a_{23.8} \times w + b_{23.8}), \end{aligned} \tag{4.19}$$

where r_p is the soil reflectivity (related to the soil emissivity, ε_p, by ε_p =1- r_p).

Assuming that $\varepsilon_{v18.7} \approx \varepsilon_{v23.8}$ and ignoring some small terms in Eqs. (4.18) and (4.19), $T_{B18.7v\_land}$ can be approximately expressed, by combining Eqs. (4.18) and (4.19), as:

$$T_{B18.7\mathrm{v}\_land} = A_1 \times T_{B18.7V\_TOA} + A_2 \times (T_{B18.7\mathrm{v\text{-}TOA}} - T_{B23.8\mathrm{V\text{-}TOA}}), \tag{4.20}$$

where A_1 and A_2 are unknown coefficients.

To improve the accuracy of Eq. (4.20), correction terms were added, and the coefficients were determined from the simulated data.

$$T_{B18.7\mathrm{v}\_land} = T_{B18.7\mathrm{v}\_toa} + 0.506\times(T_{B18.7\mathrm{v}\_toa} - T_{B23.8V-TOA}) - 0.019\times(T_{B18.7V-TOA} - T_{B23.8V-TOA})^2 - 0.085. \quad (4.21)$$

Fig. 4.23 shows the difference between $T_{B18.7V\text{-}TOA}$ and $T_{B18.7v\_land}$ (ΔT_1) and the difference between $T_{B18.7v\_land}$ estimated by Eq. (4.20) and $T_{B18.7v\_land}$ in the simulated database (ΔT_2).

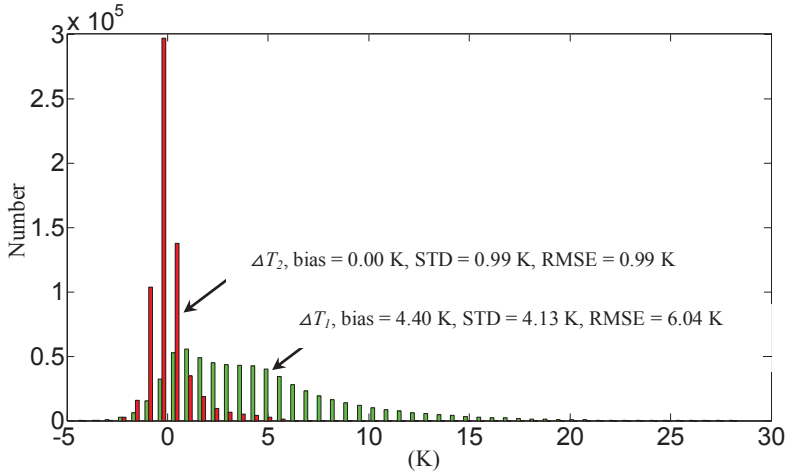

Figure 4.23 Difference between simulated values of $T_{B18.7V\text{-}TOA}$ and $T_{B18.7v\text{-}land}$. T_1 is the difference between the simulated values of $T_{B18.7v\text{-}TOA}$ and $T_{B18.7v\text{-}land}$. T_2 is the difference between the estimated values of $T_{B18.7v\text{-}land}$ using Eq. (4.21) and $T_{B18.7v\text{-}land}$

Fig. 4.23 shows that this algorithm can correct for the atmospheric effects and that RMSE may decrease from 6.04 K to 0.99 K. Using this algorithm, the land surface emission can be estimated without using any other auxiliary data. Moreover, if $\varepsilon_{18.7v}$ is known, LST can be estimated from AMSR-E data using the following equation.

$$T_s = \frac{T_{B18.7V-TOA}}{\varepsilon_{18.7\mathrm{v}}} + \frac{0.506\times(T_{B18.7V-TOA} - T_{B23.8V-TOA})}{\varepsilon_{18.7\mathrm{v}}} - \frac{0.019\times(T_{B18.7V-TOA} - T_{B23.8V-TOA})^2}{\varepsilon_{18.7\mathrm{v}}} - \frac{0.085}{\varepsilon_{18.7\mathrm{v}}}. \quad (4.22)$$

Using Eq. (4.22), the estimated value of LST from the simulated data is shown in Fig. 4.24. The RMSE of the estimated LST is 1.17 K.

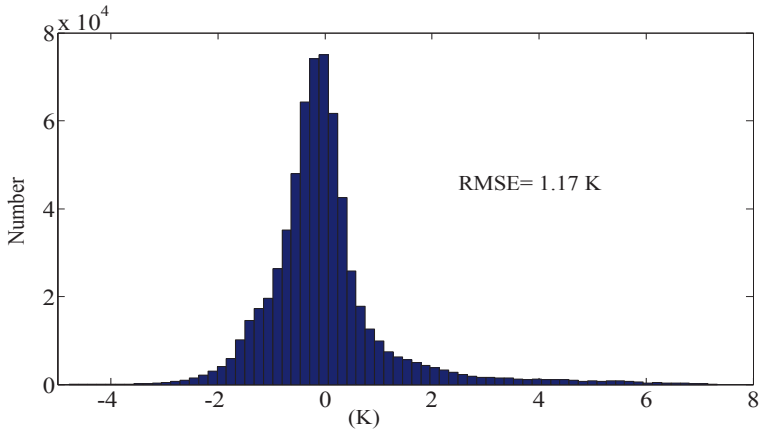

Figure 4.24 Difference between T_s estimated by Eq. (4.22) and actual value of T_s

(2) Sensitivity analysis: partial derivatives, with respect to $T_{B18.7V\text{-}TOA}$, $T_{B23.8V\text{-}TOA}$ and $\varepsilon_{18.7v}$, were computed from Eq. (4.22). Respectively, they are:

$$\frac{\partial T_s}{\partial T_{B18.7V-TOA}} = \frac{1.506 - 0.038 \times (T_{B18.7V-TOA} - T_{B23.8V-TOA})}{\varepsilon_{18.7\mathrm{v}}}, \tag{4.23}$$

$$\frac{\partial T_s}{\partial T_{B23.8\mathrm{V-TOA}}} = \frac{-0.506 + 0.038 \times (T_{B18.7V-TOA} - T_{B23.8\mathrm{V-TOA}})}{\varepsilon_{18.7\mathrm{v}}}, \tag{4.24}$$

$$\frac{\partial T_s}{\partial \varepsilon_{18.7\mathrm{v}}} = -\frac{T_{B18.7V-TOA} + 0.506 \times (T_{B18.7V-TOA} - T_{B23.8V-TOA}) - 0.019 \times (T_{B18.7V-TOA} - T_{B23.8V-TOA})^2}{\varepsilon_{18.7\mathrm{v}}^2}. \tag{4.25}$$

Fig. 4.25 shows the results of Eqs. (4.23) and (4.24), computed using the simulated data. The results show that, if $\Delta T_{B18.7V\text{-}TOA}$ ($\Delta T_{B23.8V\text{-}TOA}$) is 1 K, ΔT_s will be approximately 1.98 K (-0.85 K). Fig. 4.26 shows the data based on the calculation in Eq. (4.25). The bias and STD of Eq. (4.25) are -325.41 K and 32.77 K, respectively. This means that, if $\Delta\varepsilon_{18.7v}$ is 0.01, ΔT_s will be approximately -3.25 K.

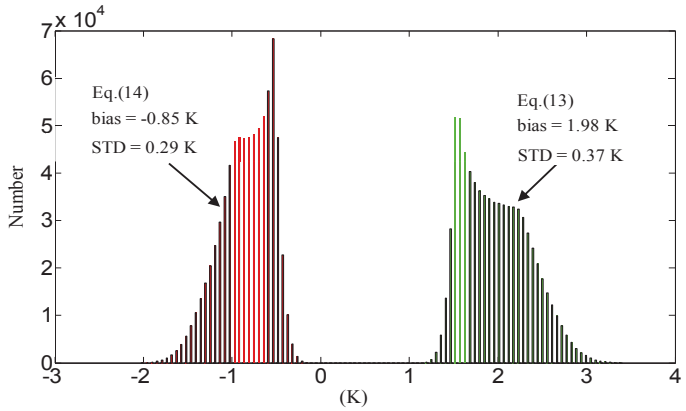

Figure 4.25 Histograms of the results of Eqs. (4.23) and (4.24) using the simulated data

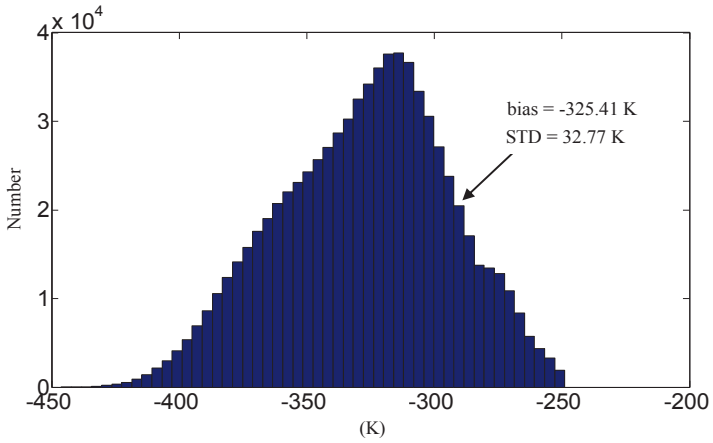

Figure 4.26 Histogram of the results computed by Eq. (4.25), based on the simulated data

Chapter 5

LSE and LST retrieval from MSG-2/SEVIRI data

5.1 Introduction

LST is one of the primary factors that govern energy exchange between the land surface and the atmosphere. This factor is used in global change studies to estimate radiation budgets in heat balance studies and is also a key parameter in climate models (Mallick et al., 2008). Due to the considerable difficulties of acquiring *in situ* LST representations at the satellite pixel scale, the need for satellite-based LST measurements is highlighted, as these measurements are the only way to provide the LST on a regional or global scale. Therefore, various LST retrieval algorithms have been proposed and developed over the past three decades (Li et al., 2013a). These algorithms can be roughly grouped into two categories based on the wavelength used: TIR techniques and MW techniques. However, because of the smaller range in variation of LSE in the TIR domain and the stronger dependence of the radiance on temperature, there are fewer uncertainties involved in TIR-based LST retrieval than in microwave-based LST retrieval (Sun, 2011). Therefore, TIR techniques are widely used to estimate the LST from space.

Currently, three major TIR-based LST retrieval methods have been developed, including the single-channel method, the split-window (SW) method and the multi-angle method, and all of these methods require a priori knowledge of the LSE (Dash et al., 2002; Li et al., 2013a). The single-channel method retrieves the LST from the radiance measured in a single atmospheric window channel and corrects for atmospheric effects using a confident knowledge of accurate atmospheric profiles (Price, 1983). However, these accurate atmospheric profiles are not available with sufficient spatial density or at the same time as the passage of the satellite. The SW method is based on the different atmospheric absorptions in two adjacent channels to correct for atmospheric effects and does not require knowledge of accurate atmospheric profiles. This method was first proposed by McMillin to determine sea surface temperature (McMillin, 1975) and extended to LST retrieval by Price (Price, 1984). Following the application of this method to LST retrieval, a variety of SW algorithms have been developed and modified with some success to retrieve LST from space instruments such as the MODIS and AVHRR (Coll and Caselles, 1997; Li et al., 2013b; Wan and Dozier, 1996;). The multi-angle method is based on a similar principle as that used in the SW method but uses different absorption results from the different atmospheric path-lengths that correspond to different observation angles. However, this method assumes that the surface temperature is angular independent.

The MSG satellite is a new generation of geostationary meteorological satellite (http://www.eumetsat.int). The main payload in this satellite, the SEVIRI, provides data in four visible and near infrared (VNIR) channels and eight infrared channels every 15 minutes, which provides the possibility of obtaining the LST frequently. From these data, a SW method is operationally used to generate an MSG/SEVIRI LST product by the Land Surface Analysis of Satellite Application Facility (LSA SAF) (http://landsaf.meteo.pt/). However, the LSE used in this SW method is estimated using the vegetation cover method, which relies on the land cover obtained from land classification maps and on corresponding laboratory measurements of LSE extracted from spectral libraries (Caselles and Sobrino, 1989; Peres and DaCamara, 2005). Therefore, the accuracy of the retrieved LSE significantly depends on both the accuracy of the land classification and the LSE values assigned to each class (Li et al., 2013b). Jiang et al. (2006) and Jiang (2007) estimated the LST from MSG-1/SEVIRI data using a SW method proposed by Becker and Li (1990) and improved by Wan and Doizer (1996); in this method, the LSE was derived using the day/night temperature-independent spectral indices (TISI)-based method proposed by Becker and Li (1990) and improved by Li and Becker (1993) and Li et al. (2000). This method provides a new approach for retrieving the LSE/LST from SEVIRI data. Nevertheless, there are some deficiencies in the algorithms of these methods, such as the atmospheric correction failures in regions with a late local sunrise time and the sensitivity of the bi-directional reflectivity model to errors in the reflectivities. Therefore, based on the work of Jiang et al. (2006) and Jiang (2007), an improved algorithm for retrieving the LSE and LST from MSG-2/SEVIRI data is developed in this thesis. Three components of this algorithm are improved: the atmospheric corrections, the fitting of the bi-directional reflectivity model and the retrieval of the LSE in channel 10 of the SEVIRI. Furthermore, a preliminary validation of the LST retrieved from SEVIRI data using the improved algorithm is performed with MODIS-derived validated LST data extracted from the V5 MOD11B1 product.

This chapter is organized as follows. Section 5.2 describes all data used in this study. The principles of the LSE and LST retrieval methods and their application to SEVIRI data are detailed in section 5.3. Section 5.4 presents the preliminary results derived from the MSG-2/SEVIRI data and the results of their cross-validation with the MODIS-derived LST product. Section 5.5is devoted to conclusions.

5.2 Descriptions of all datasets used in the Study

The study area B described in section 3.1.2 of chapter 3 is used in this work. The main payload of MSG-2, SEVIRI, provides data in 12 spectral bands every 15 minutes; it is therefore particularly suited to determining LSE on the day/night TISI concept and then deriving the LST using the SW method.

The primary product of the MSG is the MSG Level 1.5 product, which can be read by SEVIRI Pre-processing Toolbox (SPT) software. In this chapter, to illustrate the improvements on LSE and LST retrievals, the MSG datasets on August 22, 2009, March 13, 2009, July 3, 2008 and March 2, 2008 are used. To delineate all possible occurrences of clouds within each pixel, the corresponding MSG cloud masks are used. In addition, the atmospheric effect for each pixel is corrected using the atmospheric radiative transfer code (MODTRAN 4.0) with the aid of the atmospheric profiles provided by ECMWF. The ECMWF reanalysis operational deterministic model data provide 25-level profiles of pressure, temperature, relative humidity, and geo-potential with spatial resolutions of 0.25°/0.25° latitude/longitude at four synoptic UTC times: 00:00; 06:00; 12:00; 18:00.

Ancillary input data related to the LSE retrieval consisted of data on view/sun geometry, digital elevation model (DEM) and geolocation information (latitudes and longitudes) and land/sea water mask for each pixel.

Moreover, to acquire the coefficients from simulated data obtained using the SW method for LST retrieval, 1413 clear-sky atmospheric profiles are extracted from the Thermodynamic Initial Guess Retrieval (TIGR) dataset (http://ara.lmd.polytechnique.fr/htdocs-public/products/TIGR), which represents a worldwide set of atmospheric situations from polar to tropical atmospheres.

Due to the difficulty of obtaining in situ LST measurements at the satellite pixel scale (~km^2), the MODIS-derived LST over the entire study area, which is extracted from the V5 MOD11B1 product (denoted as MODIS LST), is used to validate the SEVIRI-derived LST in this study. In this chapter, the validation is performed with the data on July 3, 2008 and August 22, 2009 to ensure that the validation results are representative, as more valid SEVIRI-derived LST data at different atmospheric and land cover conditions on the two days are available. The MODIS LST product with a spatial resolution of 5.6 km was constructed using the results produced by the day/night LST algorithm and has been validated to have an

accuracy greater than 1 K in most cases through field campaigns in 47 clear-sky cases (Wan, 2008; Wan and Li, 2008). LSEs from the V5 MOD11B1 product, on the other hand, have not been validated. Therefore, the cross-calibration in this study is carried out in terms of LST. In addition to day and night LSTs for each pixel, information on LSE, VZA, viewing time, and quality control (QC), which are the key input parameters for the cross-calibration, is also stored.

Because the LST significantly varies in space and time, this cross-validation of SEVIRI-derived LST with MODIS LST under clear skies (QC=0) must be conducted on the same site and within as short a time period as possible. Considering the facts that the SEVIRI provides LSTs every 15 minutes and the SEVIRI measurements closest in view time to the MODIS are eligible to be used in this study, only the pixels with a view time difference of less than 7.5 minutes are considered for this cross-validation. In addition, to solve the issue of inconsistency in spatial resolution, a radiance-based pixel aggregation method is employed to match coordinates between the two LST products (Jiang, 2007). Furthermore, because Meteosat is a geostationary meteorological satellite, its sun-satellite viewing geometry results in the observation of sunlit scenes; MODIS, on the other hand, obtains the LSTs over the entire study area from a wide range of viewing perspectives, and its sun-satellite viewing geometry leads to the detection of a portion of shadow surfaces. To reduce the difference in LST caused by the shadow surfaces, only pixels with MODIS VZAs less than 30° are considered in this study.

All of the datasets used in this study are recapitulated in Table 5.1.

Table 5.1 Datasets used in this study

	Dataset
LSE retrieval	MSG Level 1.5 product MSG cloud mask ECMWF atmospheric profiles View/Sum geometry data DEM data Geolocation information Land/sea water mask
LST retrieval	TIGR atmospheric profiles
Cross-validation	MODIS LST extracted from V5 MOD11B1 product

5.3 LSE and LST Retrieval from MSG-2/SEVIRI Data

5.3.1 Radiative Transfer Model

Based on the radiative transfer theory introduced in chapter 2, for a clear-sky atmosphere in local thermodynamic equilibrium, the radiance, $R_i(\theta_v,T_i)$ measured in channel i at the VZA, θ_v, is given by Eqs. (2.22) and (2.23).

5.3.2 LSE Retrieval

(1)Principle of day/night TISI-based method: This method uses the property that, in the MIR channel (approximately at 3.7 μm), the radiance emitted by the land surface itself and the reflected radiance due to solar irradiation during the day are on the same order of magnitude if the surface reflectance in this channel is approximately 0.1. Li and Becker (1993) and Li et al. (2000) proposed and improved method to retrieve the LSE using the sun as an active source by defining the two channel $TISI_{ij}$ without the contribution of solar illumination between channels i and j as Eq. (5.1) through the power-law approximation of Planck's function (Jiang et al., 2006; Li et al., 2013b; Nerry et al., 1998; Tang et al., 2009).

$$TISI_{ij} = \left[\frac{R_i(\theta_v, T_{g,i})}{m_i C_i}\right]^{1/n_i} \left[\frac{R_j(\theta_v, T_{g,j})}{m_j C_j}\right]^{-1/n_j} \tag{5.1}$$

$$\text{with } C_i = \left(1 - \frac{R_{atm\downarrow,i}}{B_i(T_s)}\right) \Big/ \left(1 - \frac{R_{atm\downarrow,i}}{R_i}\right)$$

where n_i and m_i are the exponents of the power law approximation of channel radiance: $B_i(T) = m_i T^{n_i}$. The surface temperature T_s involved in the calculation of C_i is taken as the maximum surface temperature calculated with LSE=0.98 in channels 7, 9 and 10.

Assuming that the $TISI_{ij}$ (i= 4, j = 9 or 10) in the daytime without the contribution of solar illumination is the same as the $TISI_{ij}$ in the night-time, the bi-directional reflectivity ($\rho_i(\theta_v, \theta_s, \varphi)$) in the MIR channel ($i$=4 for SEVIRI channel 4) can then be extracted through a comparison of the day and night $TISI_{ij}$ (see Eq. (5.2)):

$$\rho_i(\theta_v,\theta_s,\varphi)=\frac{R_i^{day}(\theta_v,T_{g,i})}{E_{sun,i}}-\frac{\frac{C^{day}}{C^{night}}[\frac{R_j^{day}(\theta_v,T_{g,i})}{R_j^{night}(\theta_v,T_{g,i})}]^{n_i/n_j}R_i^{night}(\theta_v,T_{g,i})}{E_{sun,i}} \quad (5.2)$$

with $C=C_iC_j^{-n_i/n_j}$.

Because the MSG-2/SEVIRI provides data every 15 minutes with a fixed VZA for a given pixel, various values of $\rho_i(\theta_v, \theta_s, \varphi)$with different solar illuminated directions during the daytime can be extracted for the same pixel; the LSE in the MIR channel ($\varepsilon_i(\theta)$, see Eq. (5.4)) is then estimated to be a complement to the hemispheric-directional reflectivity, which is the integration of the angular variation of the bi-directional reflectivities described by the RossThick-LiSparse-R model (Roujean et al., 1992; Lucht and Roujean, 2000).

$$\varepsilon_i(\theta_v)=1-\int_0^{2\pi}\int_0^{\pi/2}\rho_i(\theta_v,\theta_s,\varphi)\sin(\theta_s)\cos(\theta_s)d\theta_s d\varphi \quad (5.3)$$

$$\rho_i(\theta_v,\theta_s,\varphi)=K_{iso,i}+K_{vol,i}\times f_{vol,i}(\theta_v,\theta_s,\varphi)+K_{geo,i}\times f_{geo,i}(\theta_v,\theta_s,\varphi) \quad (5.4)$$

where $K_{iso,i}$ is the isotropic scattering term in channel i, $K_{vol,i}$ and $K_{geo,i}$ are the coefficients of the volumetric kernel $f_{vol,i}$ and the geometric kernel $f_{geo,i}$ in channel i, respectively.

Assuming that the ratio of the vertical radius to the horizontal width of the spheroid crown is equal to unity and that the distance to the centre of the crown above the ground is equal to the vertical radius, for a given view zenith ranging from 0° to 80°, Jiang (2007) calculated the integration of $f_{vol,I}$ and $f_{geo,I}$ ($If_{vol,i}$ and $If_{geo,i}$) with a step of 0.05° for both the solar zenith angle and the solar azimuth and observed that the Exponential Growth function (Eq. (5.5)) and the Gauss function (Eq. (5.6)) provided very good fits to $If_{vol,i}$ and $If_{geo,i}$, respectively. The fitting parameters of Eqs. (5.5) and (5.6) are shown in Table 5.2.

$$If_{vol,i}(\theta_v)=\int_0^{2\pi}\int_0^{\pi/2}f_{i,vol}(\theta_v,\theta_s,\varphi)\sin(\theta_s)\cos(\theta_s)d\theta_s d\varphi=A_0+A_1\exp(\theta_v/t_1) \quad (5.5)$$

$$If_{geo,i}(\theta_v)=\int_0^{2\pi}\int_0^{\pi/2}f_{i,geo}(\theta_v,\theta_s,\varphi)\sin(\theta_s)\cos(\theta_s)d\theta_s d\varphi=B_0+\frac{B_1}{\omega\sqrt{\pi/2}}\exp[-2(\frac{\theta_v-\theta_c}{\omega})^2] \quad (5.6)$$

Table 5.2 Fitting parameters of the integration of volumetric kernel (If_{vol}) and geometric kernel (If_{geo})

Function	$A_0(B_0)$	$A_1(B_1)$	$t_1(\omega)$ (degree)	θ_c (degree)
$If_{vol,i}(\theta_v)$	-0.02990	0.01278	21.43823	
$If_{geo,i}(\theta_v)$	-2.01124	-29.40855	68.81710	90.95449

Finally, the LSE in the TIR channel (j=9 and 10 for SEVIRI channels 9 and 10), $\varepsilon_j(\theta_v)$, can be derived from Eq. (5.7):

$$\varepsilon_j(\theta_v) = \frac{\varepsilon_i(\theta_v)^{n_i/n_j}}{TISI_{i,j}^{night}} \tag{5.7}$$

(2) Atmospheric corrections: It is worth noting that the TISI-based method requires the quantity $R_i(\theta_v, T_{g,i})$ (i= 4, 9, 10) to construct the TISI and that atmospheric corrections must be performed for the SEVIRI MIR and TIR channels. In this study, after data checking, cloud screening and land/sea water masking procedures, the atmospheric correction is performed using MODTRAN 4.0 with ECMWF atmospheric profile data, as the TISI-based method is not sensitive to the error of atmospheric correction. However, because ECMWF atmospheric profiles have lower temporal and spatial resolutions than the SEVIRI data, modified schemes are used to approach this problem. At each synoptic time, the spatial bilinear interpolation method is used to interpolate the atmospheric quantities estimated with the ECMWF atmospheric profile data using MODTRAN 4.0, and these interpolated atmospheric quantities are then used to correct for the atmospheric effects for SEVIRI pixels. For the data measured at times other than the synoptic time, different schemes are employed to correct for the atmospheric effects in the MIR and TIR channels.

For the MIR channel (SEVIRI channel 4), time-nearest atmospheric quantities are used to correct for atmospheric effects because the measurements in this channel are less sensitive to changes in the atmospheric WVC. However, because SEVIRI channel 4 cannot be regarded as a channel with a narrow spectral range, the use of Eqs. (2.22) and (2.23) will introduce large errors in the radiance at ground level in this channel. Jiang et al. (2006) and Jiang (2007) introduced a temperature-dependent channel-averaged transmittance of SEVIRI channel 4 ($\tau_4(\theta_v, T_{g,4})$) defined by Eq. (5.8):

$$\tau_4(\theta_v, T_{g,4}) = \frac{\int_0^\infty f_4(\lambda) R(\theta_v, T_{g,4}, \lambda) \tau(\theta_v, \lambda) d\lambda}{\int_0^\infty f_4(\lambda) R(\theta_v, T_{g,4}, \lambda) d\lambda} \tag{5.8}$$

Consequently, the channel-averaged radiance in channel 4 ($L_4(\theta_v, T_4)$) can be rewritten as:

$$R_4(\theta_v, T_4) = \tau_4(\theta_v, T_{g,4}) R_4(\theta_v, T_{g,4}) + R_{atm\uparrow,4}(\theta_v) + R_{s\uparrow,4}(\theta_v) \tag{5.9}$$

As shown in Eq. (5.9), to obtain $R_4(\theta_v, T_{g,4})$, the quantity $\tau_4(\theta_v, T_{g,4})$ is a key parameter that depends on the estimation of $T_{g,4}$. The change in $\tau_4(\theta_v, T_{g,4})$ was observed to be less than 0.6% when $T_{g,4}$ varies by 10 K (Jiang et al., 2006; Jiang, 2007), which indicates that the quantity $\tau_4(\theta_v, T_{g,4})$ can be obtained with sufficient accuracy using an approximate temperature. Therefore, the quantity $R_4(\theta_v, T_{g,4})$ can be obtained as follows:

1) Computation of the approximate brightness temperature ($T_{g,4a}$) in channel 4 at ground level using Eq. (2.22);

2) Estimation of the average transmittance in SEVIRI channel 4 ($\tau_4(\theta_v, T_{g,4a})$) using Eq. (5.8) with $T_{g,4a}$;

3) Inversion of Eq. (5.9) to obtain $R_4(\theta_v, T_{g,4})$ with the estimated $\tau_4(\theta_v, T_{g,4a})$ in the second step.

Because the TIR channels (SEVIRI channels 9 and 10) are very sensitive to changes in the atmospheric water vapor content (WVC), a large error would be produced when using the time-nearest atmospheric data to obtain $R_j(\theta_v, T_{g,j})$ (j = 9 and 10) for the images acquired at times other than the synoptic times (UTC: 05:57, 11:57, 17:57 and 23:57). Therefore, to address this limitation, a two-part semi-empirical diurnal temperature cycle (DTC) model with six unknown parameters (Göttsche and Olesen, 2001) is used for the temporal interpolation to obtain $T_{g,j}$ (j= 9 and 10) at any times from those used at synoptic times. The DTC model is described by the following equations:

$$T_{g,j}^{day}(t) = a_j + b_j \cos(\beta_j (t - t_{d,j})) \qquad t \le t_s \text{ for day-time} \tag{5.10}$$

$$T_{g,j}^{night}(t) = b_{1,j} + b_{2,j} \exp(\alpha_j (t - t_{s,j})) \qquad t > t_s \qquad \text{for night-time} \tag{5.11}$$

with $$b_{2,j} = -\frac{b_j \beta_j \sin(\beta_j (t_{s,j} - t_{d,j}))}{\alpha_j}$$

$$b_{1,j} = a_j + b_j \cos(\beta_j (t_{s,j} - t_{d,j})) - b_{2,j}$$

where β_j is the angular frequency in channel j (j=9 and 10), $t_{d,j}$ is the time where the $T_{g,j}$ reaches its maximum in channel j, $t_{s,j}$ is the starting time of attenuation in channel j, and α_j is the decay coefficient at night-time in channel j.

Because atmospheric quantities are only available at four synoptic times in one day for each location, the DTC model is underdetermined with four measurements. To reduce the number of unknowns in the model and to make the model deterministic, $t_{d,j}$ (j = 9 and 10) and $t_{s,j}$ in the model are taken as known parameters and are pre-determined from the quantity T_j by assuming that the atmosphere between the ground and the satellite does not change $t_{d,j}$ and $t_{s,j}$. The DTC model described by Eqs. (5.10) and (5.11) with pre-determined $t_{d,j}$ and $t_{s,j}$ values is then fitted with a Levenberg-Marquardt least squares algorithm. However, at some locations, because of the constraint in the model related to sunrise time or cloud contaminations, only three $T_{g,j}$ values are available for fitting the DTC model, or only one $T_{g,j}$ valueis eligible before $t_{s,j}$ even if four $T_{g,j}$ values are available. In this case, the parameter α_j in the DTC model is also assumed to be the same at the satellite and ground levels. Furthermore, due to the large fluctuation in temperature and the inaccuracy of the DTC model around sunrise, data from two hours before sunrise to two hours after sunrise are excluded to construct a more accurate TISI (and therefore to retrieve more accurate LSEs).

The procedures for performing atmospheric corrections of the TIR images are shown in Fig. 5.1. These procedures are primarily divided into three steps: 1) with the aid of MODTRAN 4.0, the atmospheric quantities at a spatial resolution of 0.25°/0.25° latitude/longitude at the synoptic times are estimated with the ECMWF profiles and other ancillary data required in MODTRAN; the atmospheric effects for the SEVIRI images at each synoptic time are then corrected with spatial interpolated atmospheric quantities corresponding to SEVIRI pixels estimated with a bilinear interpolation method; 2) the parameters in the DTC model are derived from T_j (j = 9 and 10); 3) the $T_{g,j}$ (j=9 and 10) at times other than the synoptic times are estimated from those at the synoptic times using the DTC model with pre-determined $t_{d,j}$, $t_{s,j}$ or α_j.

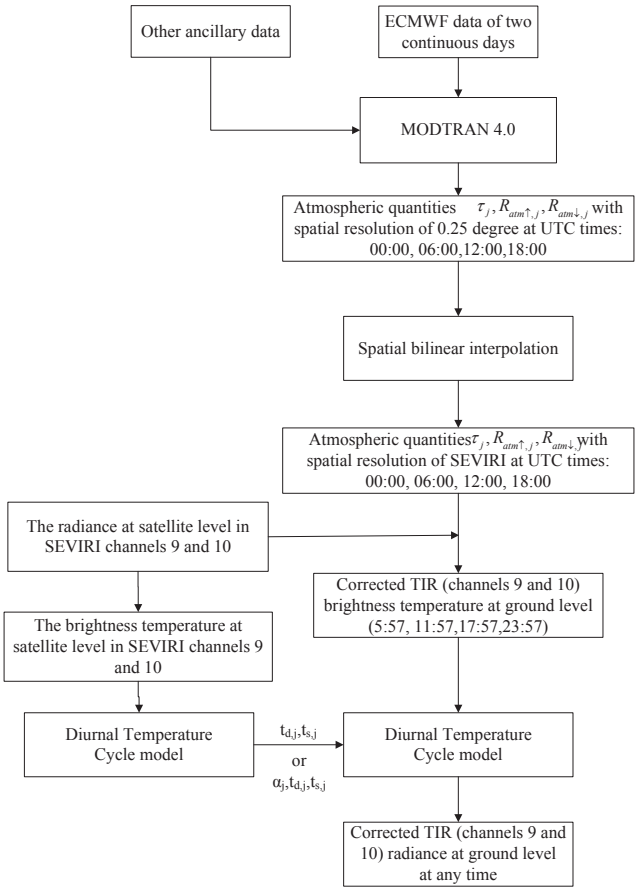

Figure 5.1 Procedures for performing atmospheric corrections for the images of the TIR channels

Jiang et al. (2006) and Jiang (2007) assumed that the values of β_j and $t_{s,j}$ (j = 9 and 10) in the DTC model derived from T_j were the same as those derived from $T_{g,j}$. To illustrate the improvement proposed in this study, two typical sites located at (33.225° N, 6.378° E) and (38.024° N, -3.834° E) are selected from the SEVIRI data from March 2, 2008 and March 13, 2009, respectively, and these data are atmospherically corrected using the DTC model with the different known parameters. Fig. 5.2 shows the modelled T_9, $T_{g,9}$ at four synoptic times, the DTC simulated temperatures at ground level with known $t_{s,9}$, $t_{d,9}$ and α_9 (because only one $T_{g,9}$ at this site is eligible before $t_{s,9}$, the DTC at ground level is fitted with known values of $t_{s,9}$, $t_{d,9}$ and α_9) and that simulated with pre-determined values of β_9 and $t_{s,9}$. It is noteworthy that in Fig. 5.2, an unreasonable $t_{d,9}$ value (9.85 on March 2, 2008, 9.73 on March 13, 2009) is derived when the DTC model at ground level is fitted with known β_9 and $t_{s,9}$ values, and the DTC fitted with the pre-determined β_9 and $t_{s,9}$ values is obviously abnormal; the DTC fitted with known $t_{s,9}$, $t_{d,9}$ and α_9 values, on the other hand, is consistent with the actual situation. This result demonstrates that the assumption proposed in this study is more reasonable.

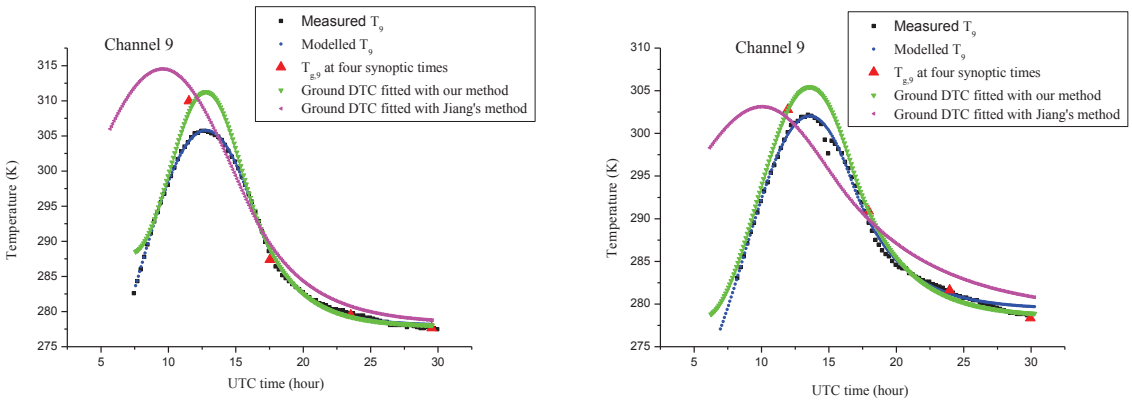

(a) (b)

Figure 5.2 Measured/Modelled brightness temperatures at the satellite and ground levels in channel 9 with different known parameters (a) for the site located at 33.225° N, 6.378° E on March 2, 2008 and (b) for the site located at 38.024° N, -3.834° E on March 13, 2009

(3) LSE retrieval: To construct the TISI, the radiance $R_i(\theta_v, T_{g,i})$ (i=4, 9 and 10) is calculated using the spatially interpolated atmospheric quantities estimated from the ECMWF data and then combined with the DTC model aforementioned. Using these $R_i(\theta_v, T_{g,i})$ values, the LSE can be retrieved with the following procedures:

1) The $E_{sun,4}$ value at any local time is predicted by assuming that $E_{sun,4}$ simply varies as a cosine function (see Eq. (5.12)).

$$E_{sun,4}(t) = A_s + B_s \cos \beta_s (t - 12) \tag{5.12}$$

where t is the local solar time and A_s, B_s and β_s are unknown coefficients that can be pre-determined using various $E_{sun,4}$ values. To accelerate the processing of ECMWF data, the $E_{sun,4}$ quantity is calculated every two hours rather than every 15 minutes (the temporal resolution of the SEVIRI).

2) The values of $\rho_i(\theta_v, \theta_s, \varphi)$ in channel 4 with different solar illumination directions are calculated assuming $C^{day}/C^{night} = 1.0$ in Eq. 5.2, which is a rather good approximation of the $\rho_4(\theta_v, \theta_s, \varphi)$ estimation (Li et al., 2006; Li, 2007). In this procedure, all of the daytime data are used, and data at 23:57 UTC are selected because (a) the TISI at night is stable (constant value during the night-time); (b) ECMWF profile data are only available at 00:00, 06:00, 12:00, 18:00 UTC every day; therefore, the SEVIRI data acquired at 23:57 UTC can be atmospherically corrected using ECMWF atmospheric profiles; and (c) for the studied region, all of the pixels observed at 23:57 UTC are measured during the night when no direct or diffuse solar radiation is

present.

3) Based on the RossThick-LiSparse-R model and Kichhoff's law, $\varepsilon_4(\theta_v)$ is derived using Eqs. (5.3) and (5.4). A Levenberg-Marquardt minimisation scheme is utilised to determine the parameters $K_{iso,4}$, $K_{vol,4}$ and $K_{geo,4}$ in Eq. (5.4) for each pixel using various values of $\rho_4(\theta_v, \theta_s, \varphi)$ with different solar illumination directions. In the fitting procedure, if the absolute difference between the measured and modelled bi-directional reflectivity is two times greater than the root mean square error (RMSE), this measurement is eliminated in the next fitting procedure until the number of measurements is reduced by 30%; in this manner, the bi-directional reflectivity model is not sensitive to the errors in the reflectivities and the parameters $K_{iso,4}$, $K_{vol,4}$ and $K_{geo,4}$ can be correctly inverted. However, in Jiang's work (Jiang, 2007), the minimum number of measurements was set to 7, which may result in local optimal solutions rather than global optimal solutions.

4) Due to the stability of the TISI at night and the availability of ECMWF data, the night-time $TISI_{4,9}$ and $TISI_{4,10}$ at 23:57 UTC are calculated and used to estimate $\varepsilon_9(\theta_v)$ and $\varepsilon_{10}(\theta_v)$ according to Eq. (5.7). However, Jiang *et al*. (2006) and Jiang (2007) derived $\varepsilon_{10}(\theta_v)$ from $\varepsilon_9(\theta_v)$ using $TISI_{9,10}$. This derivation resulted in the propagation of error in $\varepsilon_9(\theta_v)$ to $\varepsilon_{10}(\theta_v)$.

5.3.3 LST retrieval method

It is worth noting that the estimated errors in LSE in SEVIRI channels 9 and 10 with the TISI method are not independent; in particular, the error in the emissivity difference between the two adjacent channels, $\Delta\varepsilon$, is very small. Because the LST retrieval using the single-channel method is sensitive to the error of atmospheric corrections but not the LSE retrieval using the TISI method, and given that the error in $\Delta\varepsilon$ is small, the SW method can be used to derive the LST with an acceptable accuracy (Li and Becker, 1993). In this study, a generalized SW method (GSW) proposed by Becker and Li (1990) and developed by Wan and Dozier (1996) is used, in which the LST is retrieved from the MSG-2/SEVIRI data in the form of Eq. (5.13).

$$T_s = A_0 + (A_1 + A_2 \times \frac{1-\varepsilon}{\varepsilon} + A_3 \times \frac{\Delta\varepsilon}{\varepsilon^2}) \times \frac{T_9 + T_{10}}{2} + (B_1 + B_2 \times \frac{1-\varepsilon}{\varepsilon} + B_3 \times \frac{\Delta\varepsilon}{\varepsilon^2}) \times \frac{T_9 - T_{10}}{2} \qquad (5.13)$$

where ε is the averaged emissivity [$\varepsilon_{=}(\varepsilon_{9+}\varepsilon_{10})/2$];$\Delta\varepsilon = (\varepsilon_{9-}\varepsilon_{10})$; A_0, A_1, A_2, A_3, B_1, B_2 and B_3 are unknown coefficients for a given VZA and a given sub-range of ε, LST and WVC which must be pre-determined.

The coefficients A_i, B_i, and A_0 (i= 1, 3) in Eq. (5.13) can be pre-determined either from the ground LST measured synchronously with satellite brightness temperatures (T_j, j = 9, 10) or from simulated data under various atmospheric and surface conditions by statistical regression. To render the algorithm operational, the determinations of the GSW coefficients A_i, B_i (i= 1, 3) and A_0areperformed using numerical simulations, as insufficient high quality simultaneous *in situ* measurements of the LST for a wide range of surface types and atmospheric conditions are available to permit a good determination of the coefficients.

In the simulations using MOTRAN 4.0 (Berk et al., 1998) to acquire the values of coefficients A_i, B_i (i=1, 2, 3) and A_0 in Eq. (5.13), 1413 clear-sky atmosphere profiles are used in combination with various land surface conditions (LSE and LST), VZA and spectral response functions of SEVIRI channels 9 and 10 to drive MODTRAN to simulate T_j(j = 9 and 10)(Gao et al., 2013; Tang et al., 2008). For each VZA (eleven VZAs at the surface (0º, 10.16º, 20.33º, 30.52º, 35.63º, 40.76º, 45.91º, 51.08º, 56.31º, 61.6º, 67º) are considered in this work), various values of T_j (j =9 or 10) with different atmospheric profiles and surface conditions are simulated according to Eqs.(2.22) and (2.23). Furthermore, to improve the accuracy of LST retrieval for each VZA, the WVC, LSE and LST are divided into several tractable sub-ranges, i.e., WVC: 0−1.5, 1.0−2.5, 2.0−3.5, 3.0−4.5, 4.0−5.5 and 5.0−6.5 g/cm^2; ε: 0.90−0.96 and 0.94−1.0; LST: $\leqslant$ 280.0 K, 275−295 K, 290−310 K, 305−325 K, and$\geqslant$ 320 K. The coefficients A_0, A_1, A_2, A_3, B_1, B_2 and B_3 in Eq. (5.13) for each sub-range of ε, LST and WVC can be determined using the minimisation procedure with the simulated data. The results indicate that the RMSE of the retrieved LST varies with the VZA and the atmospheric WVC and that the RMSEs are within 1.0 K for all sub-ranges where the VZA<30° and WVC<4.25 g/cm^2.

Furthermore, because the atmospheric WVC is used to select the optimal coefficients A_i, B_i (i = 1, 2, 3) and A_0in the GSW method, an accurate WVC is not required provided that the estimated WVC is within the same range as the actual WVC. The method proposed by Li et al. (2003) is used to estimate the WVC at the spatial resolution of several pixels from the SEVIRI measurements of channels 9 and 10. If this method fails (if the square of the correlation coefficient is less than 0.95), the WVCs provided by the ECMWF data are used to

obtain the WVC corresponding to the relevant pixel with a temporal and spatial linear interpolation.

In practice, the LST is estimated in two steps. First, the approximate LST is estimated with the coefficients for the entire LST; then, a more accurate LST is determined using the coefficients for the LST sub-range containing the approximate LST (Jiang and Li, 2008).

Fig. 5.3 shows the key procedures for retrieving the LSE and LST from SEVIRI data. These procedures are composed of four parts. (1) Data preparation: the MSG-2/SEVIRI radiances, corresponding cloud masks, land/water masks, ECMWF profiles and other ancillary datasets, such as view geometry data and geolocation information (latitudes and longitudes) are extracted or pre-processed using SPT software and self-developed C++ programs. (2) Atmospheric correction: with the aid of MODTRAN 4.0, the atmospheric effects for the SEVIRI channels 4, 9 and 10 are corrected. For channels 9 and 10, the DTC at ground level has the same parameters ($t_{d,j}$ and $t_{s,j}$, or α_j,$t_{d,j}$ and $t_{s,j}$(j=9 and 10))as the DTC at the satellite level rather than β_j and $t_{s,j}$;. (3) LSE retrieval: LSEs in channels 4, 9 and 10 are derived based on the TISI concept and the bi-directional reflectivity model (RossThick-LiSpare-R model). In the LSE retrieval, the schemes used to fit the bi-directional reflectivity model and retrieve the LSE in the SEVIRI channel 10 are improved; (4) LST retrieval: the LST is estimated using the GSW (Eq.(5.13)) with the knowledge of T_j (j=9 and 10), the pre-determined coefficients [A_i, B_i (i = 1, 3) and A_0] in Eq.(5.13), $\varepsilon_j(\theta_v)$ (j=9 and 10), and the WVC either estimated with the method proposed by Li *et al*. (2003) or provided by the ECMWF data.

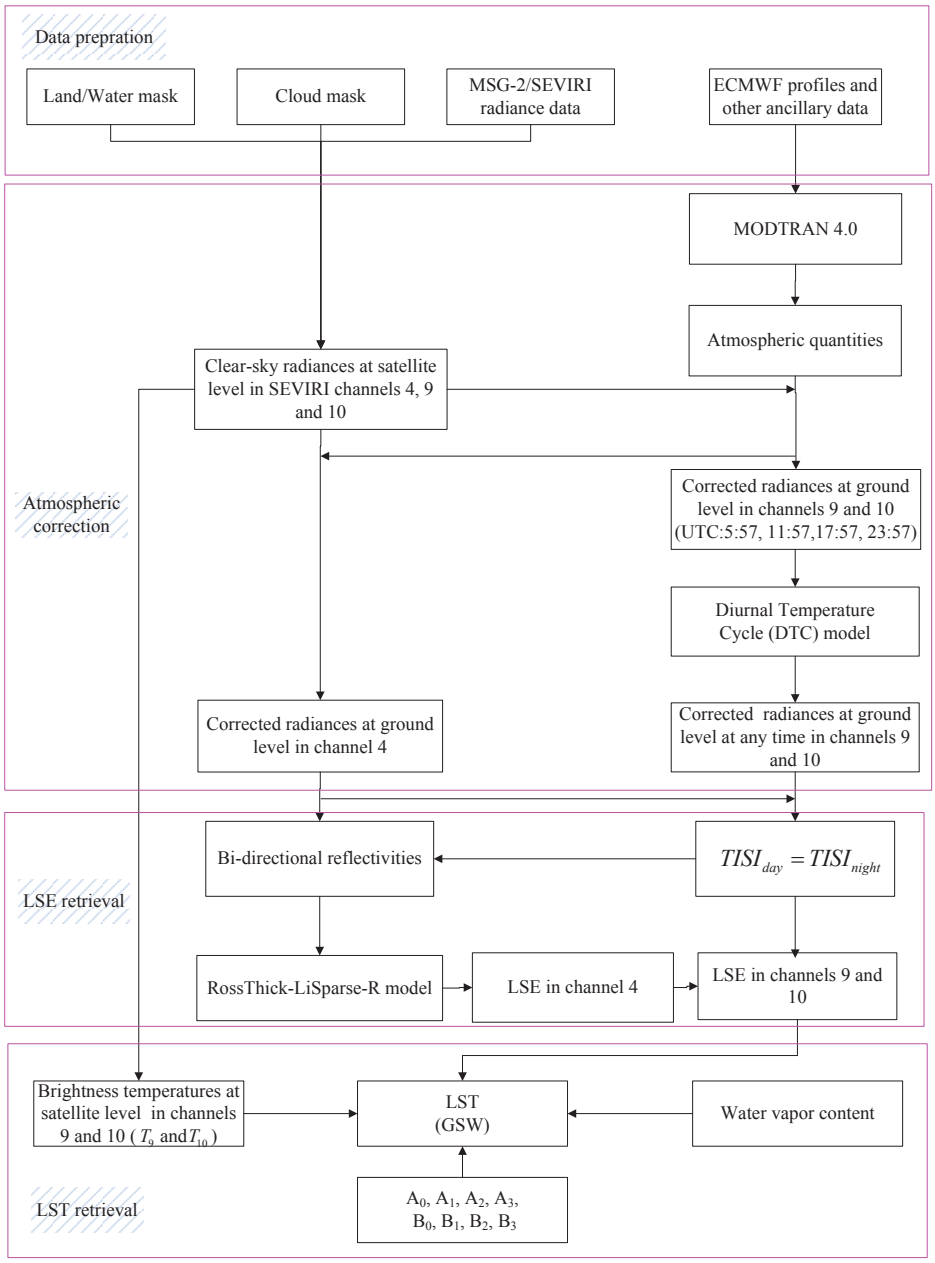

Figure 5.3 Procedures for retrieving the LSE/LST from the MSG-2/SEVIRI data

5.4 Results and cross-validation

5.4.1 Results

To analyze the performance of the algorithm described in section 5.3 under different climatic and atmospheric conditions, the algorithm is applied to these datasets on four clear-sky days (August 22, 2009; March 13, 2009; July 3, 2008 and March 2, 2008) after data processing of the MSG Level 1.5 product, the cloud filtering steps and atmospheric correction with ECMWF data and other ancillary datasets (DEM data, geolocation data (longitude and

latitude), and SEVIRI view geometry data *etc*.). As example, Fig. 5.4 shows the spatial variation of the derived LSE in channels 4, 9 and 10 (see Fig. 5.4 (a), (b) and (c), respectively) and the LST at 11:12 (see Fig. 5.4 (d)) derived from SEVIRI data over the entire study area on August 22, 2009. As shown in this figure, the entire image is spatially heterogeneous and the LSEs over the vegetated surfaces are usually higher than those over bare surfaces. The southern region of the Maghreb, which is dominated by bare soils, presents considerably higher LSTs than the other regions. However, because of the cloud contamination and limitations of the algorithm (such as the requirements for a minimum number of observations in the DTC model and the bi-directional reflectivity model), a number of LSEs/LSTs are not successfully derived. This phenomenon also occurs on the other days.

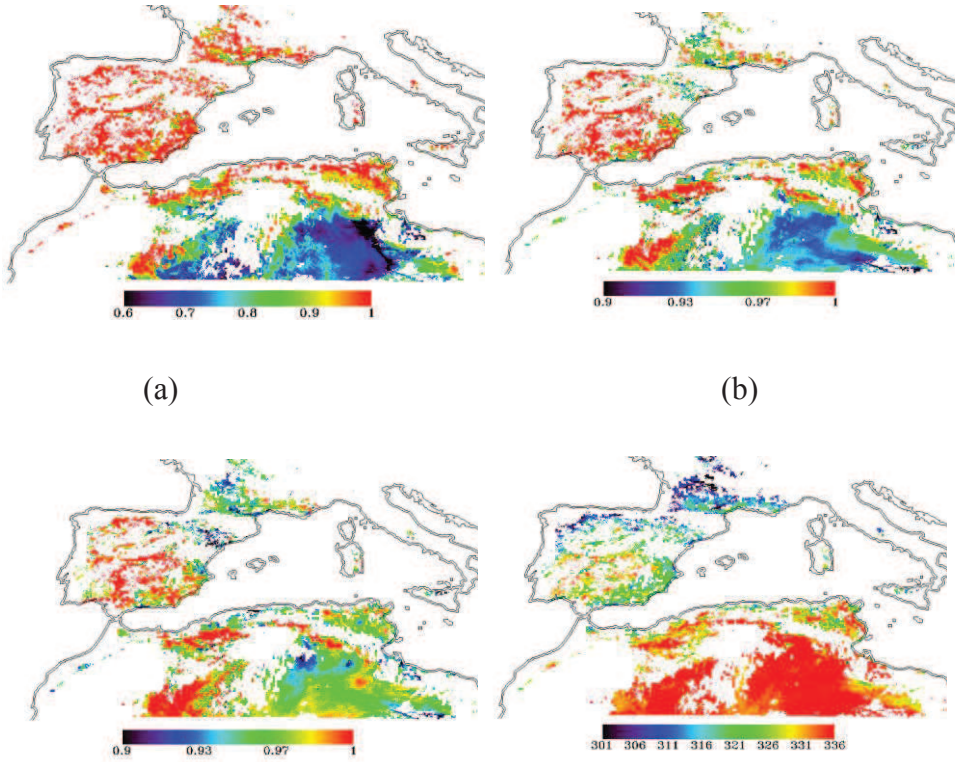

(a) (b)

(c) (d)

Figure 5.4 Maps of the LSEs in SEVIRI channels 4, 9 and 10 and the LSTs at 11:12 (UTC time) retrieved from the SEVIRI data on August 22, 2009. (a) LSE in channel 4; (b) LSE in channel 9; (c) LSE in channel 10; (d) map of the retrieved LSTs at 11:12

As mentioned in section 5.3, some improvements are adopted for the retrievals of the LSE/LST from the MSG-2/SEVIRI data. The effects of these improvements on results are analyzed with the datasets on the aforementioned four clear-sky days in terms of the following three aspects:

(1) The DTC at ground level has the same parameters ($t_{d,j}$ and $t_{s,j}$, or α_j,$t_{d,j}$ and $t_{s,j}$(j=9 and 10)) as the DTC at the satellite level rather than β_j and $t_{s,j}$. As illustrated in Fig. 5.2, unreasonable DTC coefficients are usually derived with pre-determined β_j and $t_{s,j}$ values when only one $T_{g,j}$ value is eligible before $t_{s,j}$, even if four $T_{g,j}$ values are available, which results in the failure of the atmospheric correction with the DTC model for the TIR data. This improvement can be typically illustrated by the $T_{g,9}$ obtained on March 2, 2008 and March 13, 2009, as the number of valid $T_{g,9}$ values significantly increases (see Figs. 5.5 and 5.6) from 28945 to 58956 on March 2, 2008 and from 32512 to 37642 on March 13, 2009 after improvements on the algorithm are made. For the data in channel 9 on August 22, 2009 and July 3, 2008, the differences between the value $T_{g,9}$ at 11:12 (UTC time) based on the schemes proposed in this study (denoted as LSBT1) and the value $T_{g,9}$ at 11:12 derived using the original schemes presented by Jiang et al. (2006) and Jiang (2007) (denoted as LSBT2) and the corresponding histogram of these differences are shown in Fig. 5.7. It is worth nothing that the value of LBST1 is lower than the value of LBST2 in most cases, and the differences between LBST1 and LBST2 are within 1 K. Similar results are obtained for March 13, 2009 and March 2, 2008.

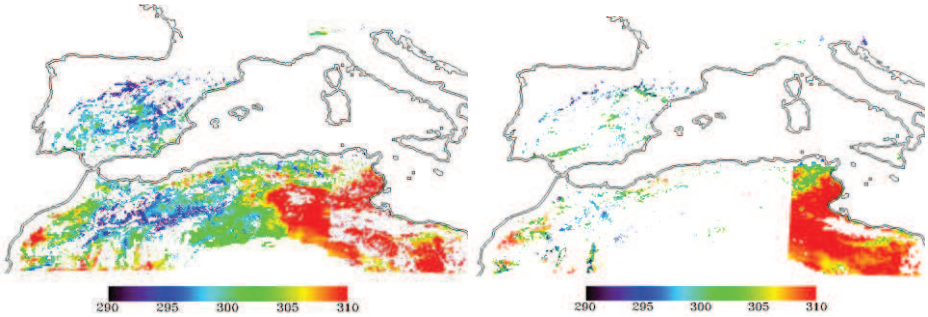

(a) (b)

Figure 5.5 Maps of the brightness temperature for surface-leaving radiances at 11:12, March 2, 2008. (a) Based on the schemes proposed in this paper and (b) based on the schemes proposed by Jiang *et al*. (2006 and 2007)

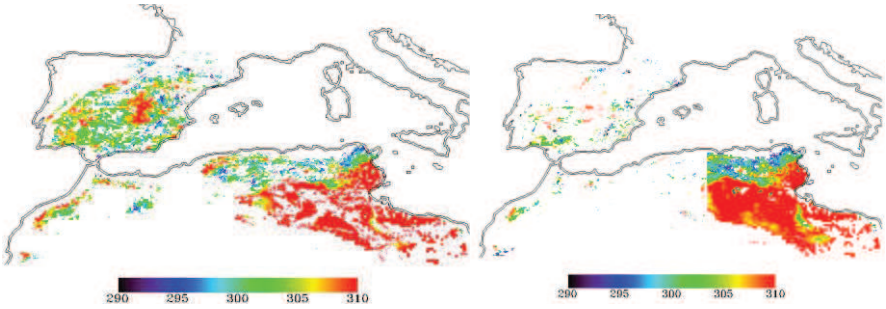

(a) (b)

Figure 5.6 Maps of the brightness temperature for surface-leaving radiances at 11:12, March 13, 2009. (a) Based on the schemes proposed in this paper and (b) based on the schemes proposed by Jiang *et al*. (2006 and 2007)

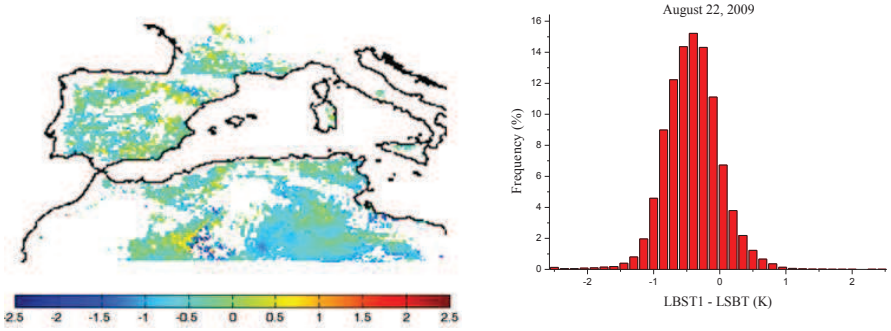

(a)

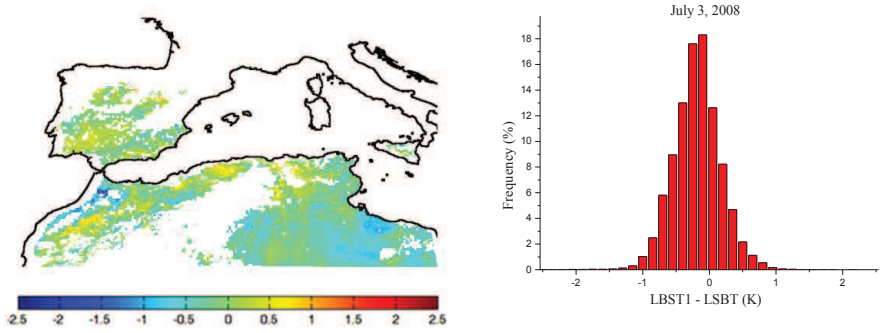

(b)

Figure 5.7 Maps of the differences between the LSBT1 and LSBT2 at 11:12 (a) on August, 22, 2009 and (b) on July 3, 2008 (UTC time) and the corresponding histogram of these differences. LSBT1 and LSBT2 are the brightness temperature for surface-leaving radiances based on the schemes proposed in this study and those derived using the original schemes proposed by Jiang *et al*. (2006 and 2007), respectively

(2) In step 3 of retrieving the LSE, if the absolute difference between the measured and the modelled bi-directional reflectivity is two times greater than the RMSE, the measurement is discarded until the number of measurements (minimum number) is reduced by 30%

(denoted as Scheme 1) rather than setting the minimum number of measurements to 7 (denoted as Scheme 2), which ensures that the bi-directional reflectivity model is not sensitive to the errors in the reflectivities and more reasonable values of $\varepsilon_4(\theta_v)$ are obtained. To illustrate this improvement, we retrieve the $\varepsilon_4(\theta_v)$ using the same values of $\rho_4(\theta_v, \theta_s, \varphi)$ on August 22 and March 13, 2009 using Schemes 1 and 2, respectively; the results of this analysis are shown in Figs. 5.8 and 5.9, respectively. It is obvious that there are less abnormal LSEs (black pixels) (see Fig. 5.8 (a) and Fig. 5.9 (a)) over the two small areas (red boxes) after improvement.

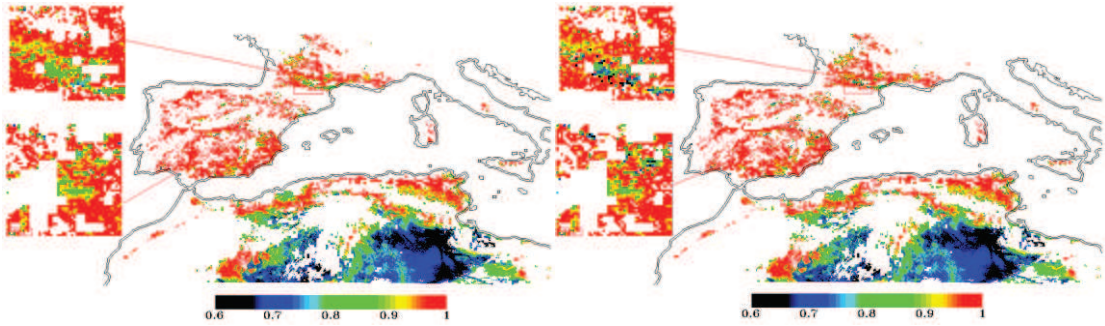

(a) (b)

Figure 5.8 Maps of the LSEs in channel 4 retrieved with the reflectivities on August 22, 2009 using different schemes. (a) Using the schemes proposed in this study; (b) using the schemes proposed by Jiang *et al*. (2006 and 2007)

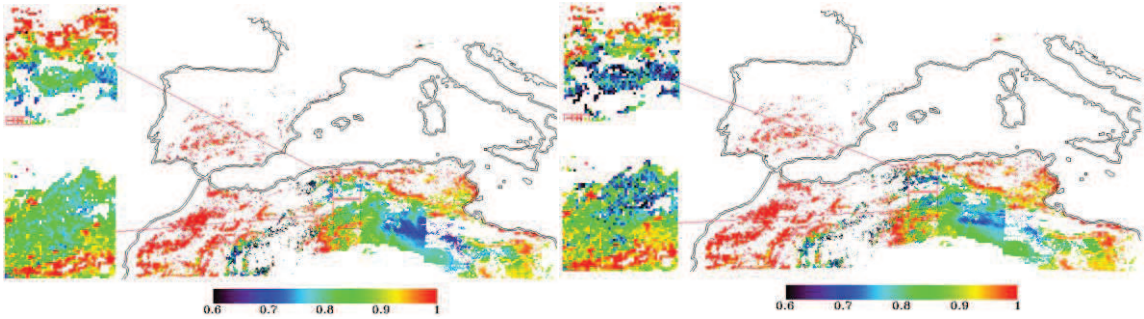

(a) (b)

Figure 5.9 Maps of the LSEs in channel 4 retrieved with the reflectivities March 13, 2009 using different schemes. (a) Using the schemes proposed in this study; (b) using the schemes proposed by Jiang *et al*. (2006 and 2007)

(3) The $\varepsilon_{10}(\theta_v)$ value is derived from $\varepsilon_4(\theta_v)$ rather than from $\varepsilon_9(\theta_v)$. The differences between the $\varepsilon_{10}(\theta_v)$ value retrieved from $\varepsilon_4(\theta_v)$(denoted as $LSE1_{10}$) and the $\varepsilon_{10}(\theta_v)$ value derived from $\varepsilon_9(\theta_v)$ ($LSE2_{10}$) are calculated; most of the differences between $LSE1_{10}$ and $LSE2_{10}$ on the four days are within 0.005. As an example, the corresponding histogram of these differences on August 22, 2009 and July 3, 2008 is shown in Fig. 5.10.

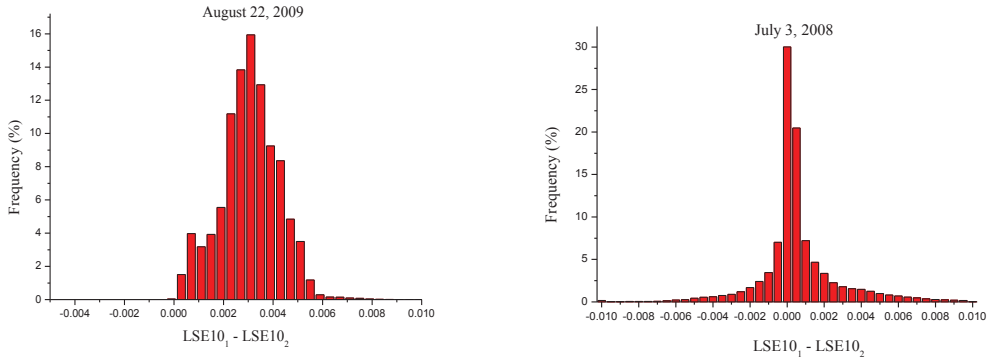

(a) (b)

Figure 5.10 Histogram of the differences between the $LSE1_{10}$ and $LSE2_{10}$ on August 22, 2009 (a) and July 3, 2008 (b). $LSE1_{10}$ and $LSE2_{10}$ are the LSEs in channel 10 derived from the LSEs in channels 4 and 9, respectively

As presented above, the improved algorithm is more effective and reasonable. To quantify the differences between the SEVIRI-derived LSE/LST (denoted as SEVIRI LSE1/LST1) retrieved with the improved algorithms and the SEVIRI-derived LSE/LST (denoted as SEVIRI LSE2/LST2) retrieved based on the original schemes proposed by Jiang et al. (2006) and Jiang (2007), the differences between the SEVIRI LSE1 and the SEVIRI LSE2 in channels 4, 9, 10 and the differences between the SEVIRI LST1 and SEVIRI LST2 at 11:12 are calculated. On the previously mentioned four days (August 22, 2009; March 13, 2009; July 3, 2008 and March 2, 2008), the LSE differences are within 0.1 for the most cases in channel 4 and within 0.05 in channels 9 and 10; the LST differences are within 2 K in most cases. As an example, the LSE/LST differences on August 22, 2009 (UTC time) and the corresponding histograms of these differences are displayed in Fig. 5.11. It is worth nothing that the LSE differences in channel 4 are considerably higher than those in channels 9 and 10; more than 85% of the LSE differences are within 0.05 for channel 4 and 0.02 for channels 9 and 10; more than 85% of the LST differences are within 1.0 K, though, in some instances, differences greater than 2.0 K are also observed. Moreover, the diurnal cycles of SEVIRI LST1/LST2 on August 22, 2009 and their differences in two homogeneous areas (geographic coordinates: 35.176°N, 5.001°W; 34.493°N, 2.527°W) covered by trees and shrubs, respectively, are displayed in Fig. 5.12. It is worth noting that the differences between SEVIRI LST1 and SEVIRI LST2 over the tree-covered area are within 0.65 K, while the differences over the shrub-covered area range from -1.0 K~-1.5 K.

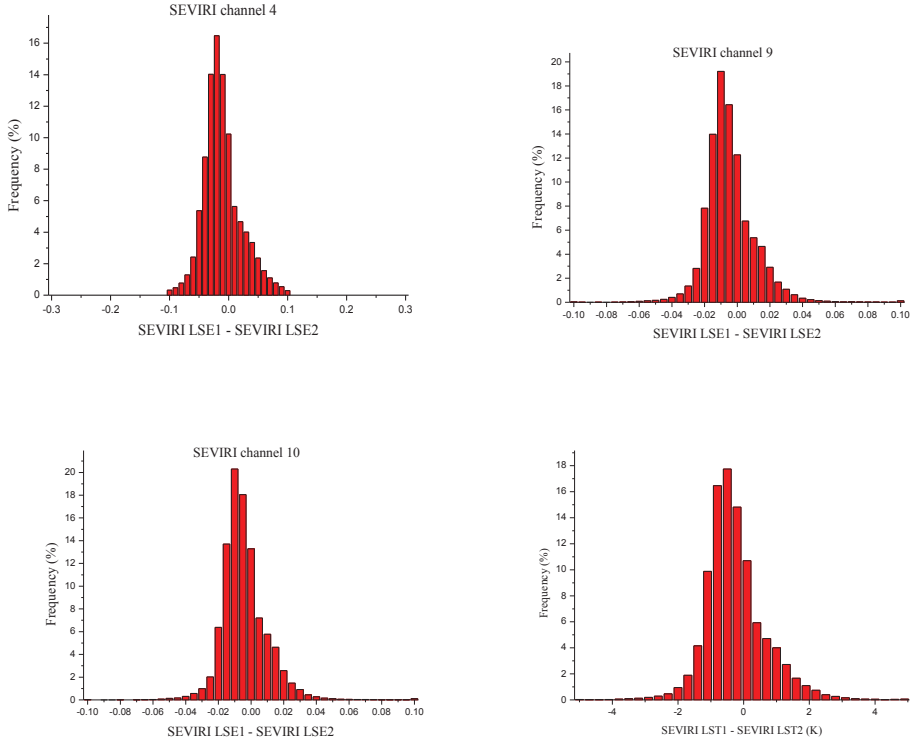

Figure 5.11 The histograms of the differences between the SEVIRI LSE1 and the SEVIRI LSE2 on August 22, 2009 and the corresponding differences between the SEVIRI LST1 and the SEVIRI LST2 at 11:12 (UTC time). SEVIRI LSE1/LST1 is the LSE/LST retrieved using the algorithms proposed in this study, and SEVIRI LSE2/LST2 is the LSE/LST retrieved based on the original schemes proposed by Jiang *et al.*(2006 and 2007)

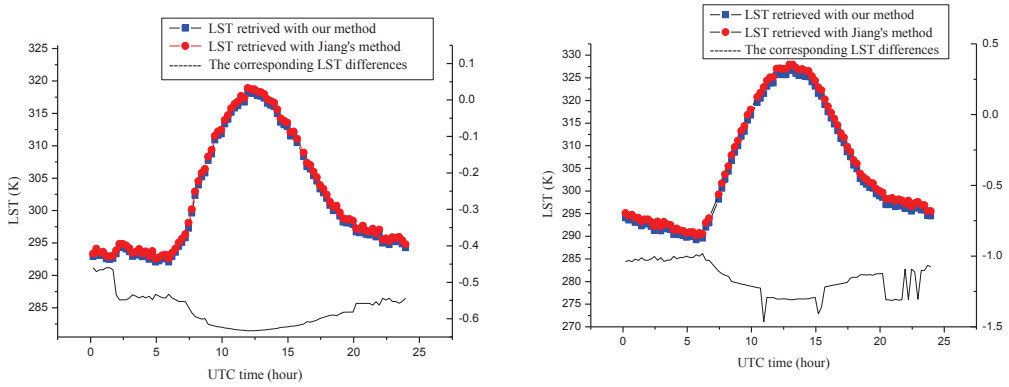

(a) (b)

Figure 5.12 The diurnal cycles of LST on August, 22, 2009 retrieved with our method and Jiang's method, at two respective sites (a) 35.176°N, 5.001°W, covered by trees; (b) 34.493° N, 2.527°W, covered by shrubs

5.4.2 Preliminary cross-validation

After data pre-processing, the qualified SEVIRI LST1 is cross-validated with the MODIS

LST over the entire study area on the two clear-sky days (August 22, 2009 and July 3, 2008). The LST differences between the SEVIRI LST1 and the MODIS LST as a function of the MODIS LST and the histograms of the LST differences are shown in Fig. 5.13. It is noteworthy that the differences between the SEVIRI LST1 and the MODIS LST have no obvious relationship with the MODIS LST; approximately more than 70% of the LST differences are within 2.5 K on both August 22, 2009 and July 3, 2008, and the differences in LST tend to be lower at night than during the day, which may be explained by the relatively homogeneous thermal conditions of the Earth's surface at night. However, in several instances, differences between the SEVIRI LST1 and the MODIS LST on August 22, 2009 reach approximately 10 K, which may have been caused by the misdetection of clouds.

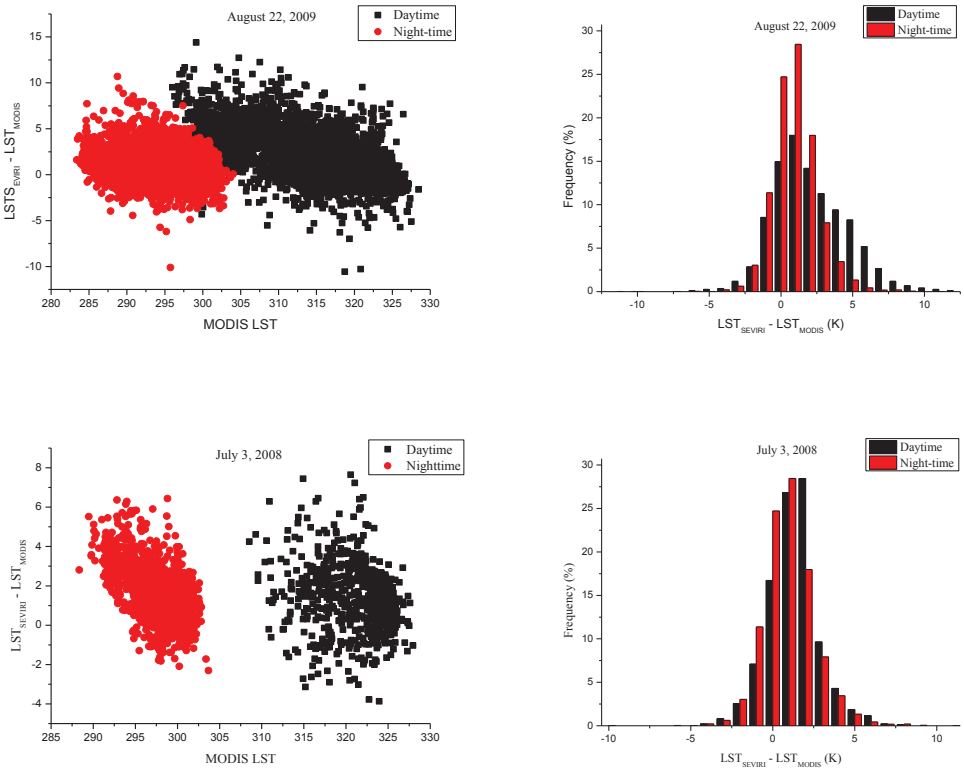

Figure 5.13 The differences between the SEVIRI LST1 and the MODIS LST as a function of the MODIS LST and the corresponding histograms of their LST differences on August 22, 2009 and July 3, 2008. The SEVIRI LST1 is the LST retrieved in this study, and the MODIS LST is the LST extracted from the V5 MOD11B1 product

Chapter 6

Conclusions

Conclusions

The objectives of this thesis were twofold: (1) improve the current method for retrieving land surface emissivity and temperature from SEVIRI data; (2) investigate the potential of passive microwave data (AMSR-E data) for retrieval of land surface emissivity and temperature in all-weather conditions. The primary work includes the development of a comprehensive soil-atmosphere radiative transfer model in passive microwave region, the methodological development for retrieving land surface emissivity and temperature from AMSR-E data, the improvement of algorithm for land surface emissivity and temperature retrievals from SEVIRI data.

The major findings and implications of this thesis are summarized below:

(1) A comprehensive soil-atmosphere radiative transfer model in MW was developed to simulate the brightness temperatures at the top of the atmosphere for microwave frequencies, based on the AIEM and MonoRTM models.Using this model, a microwave emission database was simulated for bare surfaces with a wide range of surface roughness and dielectric properties under the configuration of the AMSR-E, which is used subsequently to propose LST and LSE retrieval methods.

(2) Several empirical parameterized relationships between vertical and horizontal polarization emissivities were developed. With the proposed relationships, the differing effects of soil moisture and surface roughness on the microwave emission of bare surfaces can be separated efficiently. Simulated results using the proposed relationships are compared with those of AIEM model. These results show that the proposed relationships are accurate, with absolute root-mean-square errors (RMSEs) of 0.0025, and they can be used as a reliable boundary condition to retrieve other surface geophysical parameters.

(3) Quantitative analysis of the atmospheric effects on AMSR-E data was performed. The differences between observed brightness temperatures at the top of the atmosphere and at the bottom of the atmosphere were analysed using a database of simulated observations, which were configured to replicate AMSR-E data. The differences between observed brightness temperatures at the top of the atmosphere and land surface-emitted brightness temperatures were also computed. Quantitative results show that the atmosphere has different effects on brightness temperatures in different AMSR-E channels. Atmospheric effects can be neglected at 6.925 and 10.65 GHz, when the standard deviation is less than

1 K. However, at other frequencies and polarizations, atmospheric effects on observations should not be neglected.

(4) An atmospheric correction algorithm was proposed at 18.7 GHz vertical polarization, based on the classic split-window algorithm used in thermal remote sensing. With this correction algorithm, atmospheric effects on observations at 18.7 GHz vertical polarization can be removed effectively and the emission of land surfaces, at 18.7 GHz vertical polarization, can be estimated with RMSE=0.99 K using the measurements of two AMSR-E channels (18.7 and 23.8 GHz vertical polarization). Provided that the land surface emissivity is known, land surface temperature (LST) can be retrieved with an RMSE of 1.17 K using the simulated data.

(5) An improved algorithm was developed for simultaneously retrieving both the LSE and the LST from SEVIRI data. Three components of the day/night TISI-based algorithm for retrieving the LSE from SEVIRI data are improved: the atmospheric correction, the fitting of the bi-directional reflectivity model and the retrieval of the LSE in SEVIRI channel 10. The GSW method proposed by Becker and Li (1990) and improved by Wan and Dozier (1996) was adapted to retrieve the LST from SEVIRI dada with the knowledge of the retrieved LSE and the coefficients in equation (5.13) [A_i, B_i (i= 1, 3) and A_0] that were pre-determined during a numerical simulation under various atmospheric and surface conditions.

(6) Applying our improved algorithm to the SEVIRI data under different climatic and atmospheric conditions revealed that the improved atmospheric correction algorithm resolves the problem that prevented the original algorithm proposed by Jiang *et al*. (2006) and Jiang (2007) from being applied to specific issues successfully, especially for the atmospheric correction in regions with a late local sunrise time. Less abnormal LSEs were obtained with the improved algorithm, illustrating that the improved algorithm is more reasonable and efficient.

(7) To preliminarily validate the LST data (SEVIRI LST1) derived from the SEVIRI measurements obtained using the improved algorithm, cross-validations were conducted on two clear-sky days (August 22, 2009 and July 3, 2008) over the entire study area with the MODIS-derived validated LST (MODIS LST). It is noteworthy that more than 70% of the differences between the SEVIRI LST1 and MODIS LST are within 2.5 K and that the

LST differences tend to be lower at night than in the day, which may result from the homogeneous thermal conditions at night.

Perspectives

The results of this study open interesting perspectives. In the LSE retrieval from SEVIRI data, the accuracy of the estimated LSEs is mainly dependent on the accuracy of atmospheric corrections and the performance of the BRDF model. Therefore, the atmospheric correction scheme and the BRDF model still need to be improved. In the LSE retrieval from AMSR-E data, efforts should be made on the simultaneous retrieval of LSE and LST.

References:

Abrams, M. (2000). ASTER: data products for the high spatial resolution imager on NASA's EOS-AM1 platform. *International Journal of Remote Sensing*, vol. 21, pp. 847-861.

Aires, F., Armante, R., Chédin, A., and Scott, N. A. (1998). Surface and atmospheric temperature retrieval with the high resolution interferometer IASI. *Proceedings of the American Mathematical Society*, vol. 98, pp. 181-186.

Aires, F., Prigent, C., Rossow, W. B., and Rothstein, M. (2001). A new neural network approach including first-guess for retrieval of atmospheric water vapor, cloud liquid water path, surface temperature and emissivities over land from satellite microwave observations. *Journal of Geophysical Research*, vol. 106, pp. 14887-14907.

Baldridge, A. M., Hook, S. J., Grove, C. I., and Rivera, G. (2009).The ASTER Spectral Library version 2.0. *Remote Sensing of Environment*, vol. 4, pp. 711-715.

Barducci, A., and Pippi, I. (1996). Temperature and emissivity retrieval from remotely sensed images using the "grey body emissivity" method. *IEEE Transactions on Geoscience and Remote Sensing*, vol. 34, pp. 681-695.

Basist, A., Grody, N. C., Peterson, T. C., and Williams, C. N. (1998). Using the Special Sensor Microwave/Imager to monitor land surface temperature, wetness, and snow cover. *Journal of Climate and Applied Meteorology*, vol. 37, pp. 888-911.

Becker, F., and Li, Z.-L.(1990a). Temperature independent spectral indices in thermal infrared bands. *Remote Sensing of Environment*, vol. 32, pp. 17-33.

Becker, F., and Li, Z.-L. (1990b). Towards a local split window methods over land surface. *International Journal of Remote Sensing*, vol. 11, pp. 369-393.

Becker, F., and Li, Z.-L. (1995). Surface temperature and emissivity at various scales: Definition, measurement and related problems. *Remote Sensing Reviews*, vol. 12, pp. 225-253.

Berk, A., Bernstein, L.S., Anderson, G.P., Acharya, P.K., Robertson, D.C.,Chetwynd, J.H., and Adler-Golden, S.M., (1998). MODTRAN cloud and multiple scattering upgrades with application to AVIRIS. *Remote Sensing of Environment*, vol. 65, pp. 367-375.

Berk, A., Anderson, G. P., Acharya, P. K., Chetwynd, J. H., Bernstein, L. S., Shettle, E. P., Mattew, M. W., and Adler-Golden, S. M. (1999). Modtran 4.0 user's manual. *Air force research laboratory space vehicles directorate, air force materiel command hanscom AFB*, MA 01731-3010.

Berk, A., Bernstein, L. S., Anderson, G. P., Acharya, P. K., Robertson, D. C., Chetwynd, J. H., and Adler-Golden, S. M. (1998). MODTRAN cloud and multiple scattering upgrades with application to AVIRIS. *Remote Sensing of Environment*, vol. 65, pp. 367-75.

Borel, C. C. (1997). Iterative retrieval of surface emissivity and temperature for a hyperspectral sensor. *First JPL Workshop on Remote Sensing of Land Surface Emissivity*.

Borel, C. C. (1998). Surface emissivity and temperature retrieval for a hyperspectral sensor. *IEEE International Geoscience Remote Sensing Symposium Proceedings*, vol. 1, pp. 546-549.

Cadeddu, M. P., Liljegren, J. C., and Pazmany, A. L. (2007). Measurements and retrievals from a new 183-GHz water vapor radiometer in the Arctic. *IEEE Transactions on Geoscience and Remote Sensing*, vol. 45, pp. 2207-2215.

Carlson, T. N., and Ripley, D. A. (1997). On the relation between NDVI, fractional vegetation cover, and leaf area index. *Remote Sensing of Environment*, vol. 62, pp. 241-252.

Caselles, V., and Sobrino, J. A. (1989). Determination of frosts in orange groves from NOAA-9 AVHRR data. *Remote Sensing of Environment*, vol. 29, pp. 135-146.

Chen, J., Chen, W., Liu, J., Cihlar, J., and Gray, S. (2000). Annual carbon balance of Canada's forest during 1895-1996. *Global Biogeochemical Cycles*, vol. 14, pp. 839-850.

Chen, K., Wu, T.-D., Tsang, L., Li, Q., Shi, J., and Fung, A. K. (2003). The emission of rough surfaces calculated by the integral equation method with a comparison to a three-dimensional moment method simulations. *IEEE Transactions on Geoscience and Remote Sensing*, vol. 41, pp. 90-101.

Chevallier, F., Morcrette, J.-J., Chéruy, F., and Scott, N. A. (2000). Use of a neural network-based longwaveradiative transfer scheme in the ECMWF atmospheric model. *Quarterly Journal of the Royal Meteorological Society*, vol. 126, pp. 761-776.

Choudhury, B. J., Schmugge, T. J., Chang, A., and Newton, R. W. (1979). Effect of surface-roughness on the microwave emission from soils. *Journal of Geophysical Research*, vol. 84, pp. 5699-5706.

Coll, C. and Caselles,V. (1997). A split-window algorithm for land surface temperature from advanced very high resolution radiometer data: Validation and algorithm comparison. *J. Geophys. Res.*, vol. 102, pp.16697-16713.

Dash, P., Göttsche, F.-M., Olesen, F.-S., and Fischer, H. (2002). Land surface temperature and emissivity estimation from passive microwave data. *International Journal of Remote Sensing*, vol. 23, pp. 2563-2594.

Dash, P., Göttsche, F.-M., and Olesen, F.-S.(2003). Emissivity and temperature estimation from MSG SEVIRI data; method validation with simulated and NOAA-14 AVHRR data. *Advance in Space Research*, vol. 32, pp. 2241-2246.

Dash, P., Göttsche, F.-M., Olesen, F.-S., and Fischer, H. (2005). Separating surface emissivity and temperature using two-channel spectral indices emissivity composites comparison with a vegetation method. *Remote Sensing of Environment*, vol. 96, pp. 1-17.

Entekhabi, D., Asrar, G. R., Betts, A. K., Beven, K. J., Bras, R. L., Duffy, C. J., Dunne, T., Koster, R. D., Lettenmaier, D. P., Mclaughlin, D. B., Shuttleworth, W. J., van Genuchten, M. T., Wei, M.-Y., and Wood, E. F. (1999). An agenda for land surface hydrology research and a call for the second international hydrological decade. *Bulletin of the American Meteorological Society*, vol. 80, pp. 2043-2058.

Entekhabi, D., and Brubaker, K. L. (1995). An analytic approach to modelling land-atmospheric interaction: 2. Stochastic extension. *Water ResourcesResearch*, vol. 31, pp. 635-643.

Escobar, J., Che´din, A., Che´ruy, F., and Scott, N. A. (1993). Re´seaux de neurones multicouches pour la restitution de variables thermodynamiques atmosphe´riques a` l'aide de sondeurs verticaux satellitaires. *C. R. Acad. Sci. Paris*, vol. 317(2), pp. 911 – 918.

Felde, G. W. and Pickle J. D. (1995). Retrieval of 91 and 150 GHz. earth surface emissivities. *Journal of Geophysical Research*, vol. 100, pp. 20855-20866.

Fily, M., Royer, A., Goïta, K., and Prigent, C. (2003). A simple retrieval method for land surface temperature and fraction of water surface determination from satellite microwave brightness temperatures in sub-arctic areas. *Remote Sensing of Environment*, vol. 85, pp. 328-338.

França, G. B. and Cracknell, A. P. (1994). Retrieval of land and sea surface temperature using NOAA-11 AVHRR data in northeastern Brazil. *International Journal of Remote Sensing*, vol. 15, pp. 1695-1712.

Fung, A. K. (1994). Microwave scattering and emission models and their applications. *Norwood: Artech House.*

Gao, H., Fu, R., Dickinson, R. E., and Juarez, R. I. N. (2008). A practical method for retrieving land surface temperature from AMSR-E over the Amazon forest. *IEEE Transactions on Geoscience and Remote Sensing*, vol. 46, pp. 193-199.

Gillespie, A., Matsunaga, T., Rokugawa, S., and Hook, S. (1998). A temperature and emissivity separation algorithm for ASTER images. *IEEE Transactions on Geoscience and Remote Sensing*, vol. 36, pp. 1113-1126.

Gillespie, A. R. (1985). Lithologic mapping of silicate rocks using TIMS. *The TIMS data users' workshop, JPL Publication*, vol. 86-38, pp. 29-44.

Gillespie, C. S., Ford, K. L., Gillespie, R. D., and Leavell, A. G. (1996). Portfolio Assessment: Some questions, some answers, some recommendations. *Journal of Adolescent & Adult Literacy*, vol. 39, pp. 480-91.

Goïta, K., and Royer, A. (1997). Surface temperature and emissivity separability over land surface from combined TIR and SWIR AVHRR data. *IEEE Transactions on Geoscience and Remote Sensing*, vol. 35, pp. 718-733.

Gordy, W., and Cook, R. (1970). Microwave Molecular Spectra, p. 94, *Wiley-Interscience*, New York.

Gordy, W., and Cook, R. L. (1984). Microwave Molecular Spectra. *New York: Wiley*.

Göttsche, F.-M, and Olesen, F.-S. (2001). Modeling of diurnal cycle of brightness temperature extracted from METEOSAT data. *Remote Sensing of Environment*, vol. 76, pp. 337-348.

Gross, E. P. (1955). Shape of collision-broadened spectral lines. *Physical Review*, vol. 97, pp. 395-403.

Holmes, T. R. H. (2008). The radiative temperature of the earth at microwave frequencies (Ph. D. thesis).VrijiUniversiteit Amsterdam, Netherlands.

Holmes, T. R. H., De Jeu, R. A. M., Owe, M., and Dolman, A. J. (2009). Land surface temperature from Ka band (37GHz) passive microwave observations. *Journal of Geophysical Research*, vol. 114, D04113, doi:10.1029/2008JD010257.

Hook, S. J., Gabell, A. R., Green, A. A., and Kealy, P. S. (1992). A comparison of techniques for extracting emissivity information from thermal infrared data for geologic studies. *Remote Sensing of Environment*, vol. 42, pp. 123-135.

Jaggi, S. (1992). An investigative study of multispectral lossy data compression using vector quantization. *Proceedings of SPIE*, vol. 1702, pp. 238-249.

Jiang, G.M., Li, Z.L. and Nerry, F., (2006). Land surface emissivity retrieval from combined mid-infrared and thermal infrared data of MSG-SEVIRI. *Remote Sensing of Environment*, vol. 105, pp. 326 – 340.

Jiang G.-M. (2007). Retrievals of land surface emissivity and land surface temperature from MSG1-SEVIRI data. *Dissertation, University of Strasbourg*.

Jiang, G.-M., and Li, Z.-L.(2008a). Split-window algorithm for land surface temperature estimation from MSG1-SEVIRI data. *International Journal of Remote Sensing*, vol. 29, pp. 6067-6074.

Jiang, G.-M., and Li, Z.-L.(2008b). Intercomparison of two BRDF models in the estimation of the directional emissivity in MIR channel from MSG1-SEVIRI data. *Optics Express*, vol. 16, pp. 19310-19321.

Jiang, G.-M., Li, Z.-L., and Nerry, F. (2006). Land surface emissivity retrieval from combined mid-infrared and thermal infrared data of MSG-SEVIRI. *Remote Sensing of Environment*, vol. 105, pp. 326-340.

Jiang, L., Tjuatja, S., Shi, J., Zhang, L., and Zhao, K. (2012). Evaluation of emission from snow-covered ground for passive microwave remote sensing. *International Journal of Remote Sensing*, vol. 33, pp. 872-886.

Jones, A. S., and von der Haar, T. H. (1990). Passive microwave remote sensing of cloud liquid water over land regions. *Journal of Geophysical Research*, vol. 95, pp. 16673-16683.

Jones, M. O., Jones, L. A., Kimball, J. S., and McDonald K. C. (2011). Satellite passive microwave remote sensing for monitoring global land surface phenology. *Remote Sensing of Environment*, vol. 115, pp. 1102-1114.

Kahle, A. B., Madura, D. P., and Soha, J. M. (1980). Middle infrared multispectral aircraft scanner data analysis for geological applications. *Applied Optics*, vol. 19, pp. 2279-2290.

Karbou, F., Prigent, C., Eymard, L., and Pardo, J. R. (2005). Microwave land emissivity calculations using AMSU measurements. *IEEE Transactions on Geoscience and Remote Sensing*, vol. 43, pp. 948-959.

Kaufman, Y. J., Tanré, D., Gordon, H. R., Nakajima, T., Lenoble, J., Frouin, R., Grassl, H., Herman, B. M., King, M. D., and Teillet, P. M. (1997). Passive remote sensing of tropospheric aerosol and

atmospheric correction for the aerosol effect. *Journal of Geophysical Research*, vol. 102, pp. 16815-16830.

Kerr, Y. H., Waldteufel, P, Wigneron, J.-P., Martinuzzi, J.-M., Font, J., and Berger, M. (2001). Soil moisture retrieval from space: the Soil Moisture and Ocean Salinity (SMOS) Mission. *IEEE Transactions on Geoscience and Remote Sensing*, vol. 39, pp. 1729–1735.

Li, J., Li, J., Weisz, E., and Zhou, D. K. (2007). Physical retrieval of surface emissivity spectrum from hyperspectral infrared radiances. *Geophysical Research Letters*, vol. 34, pp. L16812, doi:10.1029/2007GL030543.

Li, X., Strahler, A. H., and Friedl, M. A. (1999). A conceptual model for effective directional emissivity from nonisothermal surfaces. *IEEE Transactions on Geoscience and Remote Sensing*, vol. 37, pp. 2508-2517.

Li, Z.-L. and Becker, F. (1993). Feasibility of land surface temperature and emissivity determination from AVHRR data. *Remote Sensing of Environment*, vol. 43, pp. 67-85.

Li, Z.-L., Becker, F., Stoll, M. P., and Wan, Z. (1999a). Evaluation of six methods for extracting relative emissivity spectra from thermal infrared images. *Remote Sensing of Environment*, vol. 69, pp. 197-214.

Li, Z.-L., Becker, F., Stoll, M. P., Wan, Z., and Zhang, Y. (1999b). Channel selection for soil spectrum reconstruction in 8-13 um region. *Journal of Geophysical Research*, vol. 104, pp. 22271-22285.

Li, Z.-L., Petitocolin, F., and Zhang, R. (2000).A physically based algorithm for land surface emissivity retrieval from combined mid-infrared and thermal infrared data. *Science in China (Series E)*, vol. 43, pp. 22-33.

Li, Z.-L., Jia, L., Su, Z., Wan, Z., and Zhang, R. (2003). A new approach for retrieving precipitable water from ATSR2 split-window channel data over land area. *International Journal of Remote Sensing*, vol. 24, pp. 5059-5117.

Li, Z.-L., Tang, B.-H., Wu, H., Ren, H., Yan, G.J., Wan, Z., Triggo, I.F. and Sobrino, J.A. (2013a). Satellite-derived land surface temperature: Current status and perspectives. *Remote Sens. Environ.*, vol. 131, pp.14-37.

Li, Z.-L., Wu, H., Wang, N., Qiu, S., Sobrino, J.A., Wan, Z., Tang, B.-H. and Yan, G.J. (2013). Land surface emissivity retrieval from satellite data. *Int. J. Remote Sens.*, vol. 34, pp. 3084-3127.

Liu, Z.-L., Wu, H., Qiu, S., Jia, Y.-Y., and Li, Z.-L. (2010). Determination of land surface temperature from AMSR-E data for bare surface. *IEEE International Geoscience Remote Sensing Symposium Proceedings*, pp. 3011-3014.

Lucht, W. (1998). Expected retrieval accuracies of bidirectional reflectance and albedo from EOS-MODIS and MISR angular sampling. *Journal of Geophysical Research*, vol. 103, pp. 8763-8778.

Lucht, W., and Roujean, J. (2000). Considerations in the parametric modeling of BRDF and albedo from multiangular satellite sensor observations. *Remote Sensing Reviews*, vol. 18, pp. 343-379.

Ma, X., Wan, Z., Moeller, C. C., Menzel, W. P., and Gumley, L. E. (2002). Simultaneous retrieval of atmospheric profiles, land-surface temperature, and surface emissivity from Moderate-Resolution Imaging Spectroradiometer thermal infrared data: extension of a two-step physical algorithm. *Applied Optics*, vol. 41, pp. 909-924.

Ma, Y., Tsukamoto, O., Wu, X., Tamagawa, I., Wang, J., Ishikawa, H., Hu, Z., and Gao, H. (2000). Characteristics of energy transfer and micrometeorology in the surface layer of the atmosphere above marshland of the Tibetan Plateau area. *Chinese Journal of Atmospheric Sciences*, vol. 24, pp. 715-722 (in Chinese with English abstract).

Mallick, J., Kant, Y., and Bharath, B. D. (2008). Estimation of land surface temperature over Delhi using Landsat-7 ETM+. *Journal of Indian Geophysic Union*, vol. 12, pp. 131-140.

Matzler, C. (1994). Passive microwave signatures of landscapes in winter. *Meteorology and Atmospheric Physicis*,vol. 54, pp. 241-260.

McFarland, M. J., Miller, R. N., and Neale, C. M. U. (1990). Land surface temperature derived from the SSM/I passive microwave brightness temperatures. *IEEE Transactions on Geoscience and Remote Sensing*, vol. 28, pp. 839-845.

McMillin, L. M. (1975). Estimation of sea surface temperature from two infrared window measurements with different absorptions. *Journal of Geophysical Research*, vol. 20, pp. 5113-5117.

Menzel, W. P., Seemann, S. W., Li, J., and Gumley, L. E. (2006). MODIS atmospheric profile retrieval algorithm theoretical basis document, Version 6.*NASA/GSFC*, pp. 1-40.

Minnaert, M. (1941).The reciprocity principle in lunar photometry. *Astrophysical Journal*, vol. 93, pp. 403-410.

Mo, T., and Schmugge, T. J. (1987). A parameterization of the effect of surface-roughness on microwave emission. *IEEE Transactions on Geoscience and Remote Sensing*, vol. 25, pp. 481-486.

Moncet, J.-L., Liang, P., Galantowicz, J. F., Lipton, A. E., Uymin, G., Prigent, C., and Grassotti, C. (2011). Land surface microwave emissivities derived from AMSR-E and MODIS measurements with advanced quality control. *Journal of Geophysical Research*, vol. 116, D16104, doi: 10.1029/2010JD015429.

Nerry, F., Labed, J., and Stoll, M. P. (1998a). Emissivity signatures in the thermal IR band for Remote Sensing: calibration procedure and method of measurement. *Applied Optics*, vol. 27, pp. 758-764.

Nerry, F., Petitcolin, F., and Stoll, M. P. (1998b). Bidirectional reflectivity in AVHRR channel 3: application to a region in North Africa. *Remote Sensing of Environment*, vol. 66, pp. 298-316.

Nerry, F., Stoll, M. P., and Malaplate, A. (2004). Multi temporal regression method for mid infrared [3-5 µm] emissivity outdoor measurements. *Optics Express*, vol. 12, pp. 6574-6588.

Njoku, E. G., and Li, L. (1999).Retrieval of land surface parameters using passive microwave measurements at 6 to 18 GHz. *IEEE Transactions on Geoscience and Remote Sensing*, vol. 37, pp. 79-93.

Njoku, E. G., Ashcroft, G. P., Chan, T. K., and Li, L. (2005).Global survey and statistics of radio-frequency interference in AMSR-E land observations. *IEEE Transactions on Geoscience and Remote Sensing*, vol. 43, pp. 938-947.

Njoku, E. G., Jackson, T. J., Lakshmi, V., Chan, T. K., and Nghiem, S. V. (2003). Soil moisture retrieval from AMSR-E. *IEEE Transactions on Geoscience and Remote Sensing*, vol. 41, pp. 215-229.

Ouyang, X., Wang, N., Wu, H., and Li, Z.-L.(2010). Errors analysis on temperature and emissivity determination from hyperspectral thermal infrared data. *Optics Express*, vol. 18, pp. 544-550.

Owe, M., De Jeu, R. A. M., and Walker, J. (2001). A methodology for surface soil moisture and vegetation optical depth retrieval using the microwave polarization difference index. *IEEE Transactions on Geoscience and Remote Sensing*, vol. 39, pp. 1643-1654.

Payne, V. H., Delamere, J. S., Cady-Pereira, K. E., Gamache, R., Moncet, J.-L., Mlawer, E. J., and Clough, S. A. (2008). Air-broadened half-widths of the 22- and 183-GHz water-vapor lines. *IEEE Transactions on Geoscience and Remote Sensing*, vol. 46, pp. 3601–3617.

Peres, L. F., and DaCamara, C. C. (2005). Emissivity maps to retrieve land surface temperature from MSG/SEVIRI. *IEEE Transactions on Geoscience and Remote Sensing*, vol. 45, pp. 1834-1844.

Petitcolin, F., Nerry, F., and Stoll, M. P. (2002). Mapping temperature independent spectral indice of emissivity and directional emissivity in AVHRR channels 4 and 5. *International Journal of Remote Sensing*, vol. 23, pp. 3473-3491.

Petitcolin, F., and Vermote, E. (2002). Land surface reflectance, emissivity and temperature from MODIS middle and thermal infrared data. *Remote Sensing of Environment*, vol. 83, pp. 112-134.

Prata, A. J. (1993). Land surface temperature derived from the Advanced Very High Resolution Radiometer and the Along-Track Scanning Radiometer 1. *Journal of Geophysical Research*, vol. 98, pp. 16689-16702.

Price, J. C. (1983). Estimating surface temperatures from satellite thermal infrared data-A simple formulation for the atmospheric effect. *Remote Sens. Environ*., vol. 13, pp. 353-361.

Price, J. C. (1984). Land surface temperature measurements from the split window channels of the NOAA 7 AVHRR. *Journal of Geophysical Research*, vol. 89, pp. 7231-7237.

Prigent, C., Rossow, W. B., and Matthews, E. (1997). Microwave land surface emissivities estimated from SSM/I observations. *Journal of Geophysical Research*, vol. 102, pp. 21867-21890.

Prigent, C., Rossow, W. B., and Mattews, E. (1998). Global maps of microwave land surface emissivities: Potential for land surface characterization. *Radio Science*,vol. 33, pp. 745-751.

Pulliainen, J. T., Hallikainen, M. T., and Grandell, J. (1999). Hut snow emission model and its applicability to snow water equivalent retrieval. *IEEE Transactions on Geoscience and Remote Sensing*, vol. 37, pp. 1378-1390.

Realmuto, V. J. (1990). Separating the effects of temperature and emissivity: emissivity spectrum normalization. In: Abbott, E.A. (Ed.), Proceedings of the 2nd TIMS workshop. *JPL Publication*, vol. 55-90, pp. 31-35.

Rice, S. O. (1951). Reflection of electromagnetic waves from slightly rough surfaces. *Communications on Pure and Applied Mathematics*, vol. 4, pp. 361-378.

Rosenkranz, P. W. (1975). Shape of the 5 mm oxygen band in the atmosphere. *IEEE Transactions on Antennas and Propagation*, vol. 23, pp. 498-506.

Roujean, J. L., Leroy, M., and Deschamps, P. Y. (1992). A bidirectional reflectance model of the Earth's surface for the correction of remote sensing data. *Journal of Geophysical Research*, vol. 97, pp. 455-468.

Rubio, E., Caselles, V., and Badenas, C. (1997). Emissivity measurements of several soils and vegetation types in the 8-14 um waveband: analysis of two field methods. *Remote Sensing of Environment*, vol. 59, pp. 490-521.

Rubio, E., Caselles, V., Coll, C., Valor, E., and Sospedra, F. (2003). Thermal infrared emissivities of natural surfaces: Improvements on the experimental set-up and new measurements. *International Journal of Remote Sensing*, vol. 24, pp. 5379-5390.

Russell, S. M., Keegan, A. D., Harada, N., Nakamura, Y., Noguchi, M., Leland, P., Friedmann, M. C., Miyajima, A., Puri, R. K., Paul, W. E., and Leonard, W. J. (1993). Interleukin-2 receptor gamma chain: a functional component of the interleukin-4 receptor. *Science*, vol. 262, pp. 1880–1883.

Shi, J., Jiang, L., Zhang, L., Chen, K., Wigneron, J. P., and Chanzy, A. (2005). A parameterized multi-frequency-polarization surface emission model. *IEEE Transactions on Geoscience and Remote Sensing*, vol. 43, pp. 2831-2841.

Snider, J. B., Westwater, E. R., andFedor, L. S. (1994). Radiometric correction for atmospheric effects in surface sensing from aircraft and satellites. *Passive Microwave Remote Sensing of Land-Atmosphere Interactions*, E.D. B.J. Choudhury, Y. H. Kerr, and P. Pampaloni, ed. (VSP, Zeist, Netherlands).

Snyder, W. C., and Wan, Z. (1998a). BRDF models to predict spectral reflectance and emissivity in the thermal infrared. *IEEE Transactions on Geoscience and Remote Sensing*, vol. 36, pp. 214-225.

Snyder, W. C., Wan, Z., Zhang, Y., and Feng, Y.-Z.(1998b). Classification-based emissivity for land surface temperature measurement from space. *International Journal of Remote Sensing*, vol. 19, pp. 2753-2754.

Sobrino, J. A., Gomez, M., Jimenez-Munoz, J. C., Olioso, A., and Chehbouni, G. (2005). A simple algorithm to estimate evapotranspiration from DAIS data: Application to the DAISEX Campaigns. *Journal of Hydrology*, vol. 315, pp. 117-125.

Sobrino, J. A., Julien, Y., Atitar, M., and Nerry, F. (2008). NOAA-AVHRR orbital drift correction from solar zenithal angle data. *IEEE Transactions on Geoscience and Remote Sensing*, vol. 46, pp. 4014-4019.

Sobrino, J. A., and Raissouni, N. (2000). Toward remote sensing methods for land cover dynamic monitoring. Application to Morocco. *International Journal of Remote Sensing*, vol. 21, pp. 353-366.

Sobrino, J. A., Raissouni, N., and Li, Z.-L.(2001). A comparative study of land surface emissivity retrieval from NOAA data. *Remote Sensing of Environment*, vol. 75, pp. 256-266.

Sun, D., and Pinker, R. T. (2003). Estimation of land surface temperature from Geostationary Operational Environmental Satellite (GOES-8). *Journal of Geophysical Research*, vol. 108, pp. 4326, doi: 10.1029/2002JD002422.

Sun, Y. (2011). Retrieval and application of land surface temperature. http://www.geo.utexas.edu/courses/387h/PAPER, Accessed 10, July, 2011.

Tang, B., Bi. Y., Li, Z.-L., and Xia, J. (2008). Generalized split-window algorithm for estimate of land surface temperature from Chinese geostationary FengYun Meteorological Satellite (FY-2C) data. *Sensors*, vol. 8, pp. 933-951.

Tang, B. H., Li, Z.-L., and Bi, Y. (2009). Estimation of land surface directional emissivity in mid-infrared channel around 4.0 μm from MODIS data. *Optics Express*, vol. 17, pp. 3173-3182.

Tang,B.H, Bi,Y.Y, Li, Z.-L. and Xia, J., (2008). Generalized split-window algorithm for estimate of land surface temperature from Chinese geostationary FengYun Meteorological Satellite (FY-2C) data. *Sensors*, vol. 8, vol. 933 – 951.

Tang, B.H., Li, Z.-L., Bi, Y.Y., (2009). Estimation of land surface directional emissivity in mid-infrared channel around 4.0 μm from MODIS data. *Optics Express*, vol. 17, pp. 3173−3182.

Thorsos, E. I. (1988). The validity of the Kirchhoff approximation for rough surface scattering using a Gaussian roughness spectrum. *Journal of the Acoustical Society of America*, vol. 83, pp. 78-82.

Thorsos, E. I. (1990). Acoustic scattering from a 'Pierson-Moskowitz' sea surface. *Journal of the Acoustical Society of America*, vol. 88, pp. 335-349.

Thorsos, E. I., and Jackson, D. R. (1989). The validity of the perturbation approximation for rough surface scattering using a Gaussian roughness spectrum. *Journal of the Acoustical Society of America*, vol. 86, pp. 261–277.

Townes, C. H., and Schawlow, A. L. (1955). Microwave Spectroscopy, *McGraw Hill, New York (1955), reprinted by Dover (1975)*.

Tretyakov, M. Y., Koshelev, M. A., Dorovskikh, V. V., Makarov, D. S., and Rosenkranz, P. W. (2005). 60-GHz oxygen band: precise broadening and central frequencies of fine-structure lines, absolute absorption profile at atmospheric pressure, and revision of mixing coefficients. *Journal of Molecular Spectroscopy*, vol. 231, pp. 1-14.

Ulaby, F. T., Moore, R. K., and Fung, A. K. (1981). Microwave remote sensing: active and passive, Vol. I: microwave remote sensing fundamentals and radiometry. *New York: Addison-Wesley, Reading, MA*.

Ulaby, F. T., Moore, R. K., and Fung, A. K. (1982). Microwave remote sensing: active and passive, Vol. II: radar remote sensing and surface scattering and emission theory. *New York: Addison-Wesley, Reading, MA*.

Ulaby, F. T., Moore, R. K., and Fung, A. K. (1986). Microwave remote sensing: active and passive, Vol. III: volume scattering and emission theory. *New York: Addison-Wesley, Reading, MA*.

Valor, E., and Caselles, V. (1996). Mapping land surface emissivity from NDVI: application to European, African and South American areas. *Remote Sensing of Environment*, vol. 57, pp. 167-184.

Van de Griend, A. A., and Owe, M. (1993). On the relationship between thermal emissivity and the normalized difference vegetation index for natural surfaces. *International Journal of Remote Sensing*, vol. 14, pp. 1119-1131.

Van Vleck, J. H., and Weisskopf, V. F. (1945). On the shape of collision-broadened lines. *Reviews of Modern Physics*, vol. 17, pp. 227-236.

Verstraeten, W. W., Veroustraete, F., van der Sande, C. J., Grootaers, I., and Feyen, J. (2006). Soil moisture retrieval using thermal inertia, determined with visible and thermal spaceborne data, validated for European forests. *Remote Sensing of Environment*, vol. 101, pp. 299-314.

Wan, Z. and Dozier, J., (1996). A generalized split-window method for retrieving land-surface temperature from space. *IEEE Transcations on Geosciences and Remote sensing*, vol. 34, pp. 892-905.

Wan, Z., and Li, Z.-L., (1997). A physics-based algorithm for retrieving land-surface emissivity and temperature from EOS/MODIS data. *IEEE Transactions Geoscience and Remote Sensing*, vol. 35, pp. 980- 996.

Wan, Z. (1999). MODIS land surface temperature algorithm theoretical basis document, Version 3.3. *NASA/GSFC*, pp. 1-77.

Wan, Z. (2006). MODIS land surface temperature products user's guide. *Institute for Computational Earth System Science, University of California, Santa Barbara*, CA. http://www.icess.ucsb.edu/modis/LstUsrGuide/usrguide.html.

Wan, Z. (2008). New refinements and validation of the MODIS land-surface temperature/emissivity products. *Remote Sensing of Environment*, vol. 112, pp. 59-74.

Wan, Z., and Dozier, J. (1996). A generalized split-window method for retrieving land-surface temperature from space. *IEEE Transcations on Geosciences and Remote sensing*, vol. 34, pp. 892-905.

Wan, Z., and Li, Z.-L. (1997). A physics-based algorithm for retrieving land-surface emissivity and temperature from EOS/MODIS data. *IEEE Transactions Geoscience and Remote Sensing*, vol. 35, pp. 980-996.

Wan, Z., and Li, Z.-L. (2008). Radiance-based validation of the V5 MODIS land-surface temperature product. *International Journal of Remote Sensing*, vol. 29, pp. 5373-5395.

Wan, Z., and Li, Z.-L. (2010). MODIS land surface temperature and emissivity products. In *Land Remote Sensing and Global Environmental Changes*, B. Ramachandran, C. O. Justice and M. J. Abrams, pp.563-577 (London: Springer).

Wan, Z., Zhang, Y., and Li, Z.-L.(2004). Quality assessment and validation of the MODIS global land surface temperature. *International Journal of Remote Sensing*, vol. 25, pp. 261-274.

Wan, Z., Zhang, Y., Zhang, Q., and Li, Z.-L. (2002). Validation of the land surface temperature products retrieved from Terra Moderate Resolution Imaging Spectroradiometer data. *Remote Sensing of Environment*, vol. 83, pp. 163-180.

Wang, J., and Schmugge, T. J. (1980). An empirical model for the complex dielectric permittivity of soils as a function of water content. *IEEE Transactions on Geoscience and Remote Sensing*, vol. GE-18, pp. 288-295.

Wang, J., and Choudhury, B. J. (1981). Remote sensing of soil moisture content over bare fields at 1.4 GHz frequency. *Journal of Geophysical Research*, vol. 86, pp. 5277-5282.

Wanner, W., Li, X., and Strahler, A. (1995). On the derivation of kernels for kernel-driven models of bidirectional reflectance. *Journal of Geophysical Research*, vol. 100, pp. 21077-21089.

Watson, K. (1992). Two-temperature method for measuring emissivity. *Remote Sensing of Environment*, vol. 42, pp. 117-121.

Wegmuller, U., and Matzler, C. (1999). Rough bare soil reflectivity model. *IEEE Transactions on Geoscience and Remote Sensing*, vol. 37, pp. 1391-1395.

Weng, F. Z., and Grody, N. C. (1998). Physical retrieval of land surface temperature using the special sensor microwave imager. *Journal of Geophysical Research*, vol. 103, pp. 8839-8848.

Wu, T., Chen, K., Shi, J., and Fung, A. K. (2001). A transition model for the reflection coefficient in surface scattering. *IEEE Transactions on Geoscience and Remote Sensing*, vol. 39, pp. 2040-2050.

Xiang, X., and Smith, E. A. (1997). Feasibility of simultaneous surface temperature-emissivity from retrieval using SSM/I measurements from HAPEX-Sahel. *Journal of Hydrology*, vol. 188-189, pp. 330-360.

Yang, H., and Weng, F. (2011). Error sources in remote sensing of microwave land surface emissivity. *IEEE Transactions on Geoscience and Remote Sensing*, vol. 49, pp. 3437-3442.

Zhevakin, S. A., and Naumov, A. P. (1963).Absorption coefficient of water vapour for electromagnetic waves in the wavelength range 10 μm to 2 cm. *Izvestiya Vysshikh Uchebnykh Zavedeni\u\i*, vol. 6, pp. 674-694.